

Numerical modelling of flow boiling inside microchannels: A critical review of methods and applications

Darshan M.B.^a, M. Magnini^{b,*}, O.K. Matar^a

^a Department of Chemical Engineering, Imperial College London, London SW7 2BX, United Kingdom

^b Department of Mechanical, Materials and Manufacturing Engineering, University of Nottingham, Nottingham NG7 2RD, United Kingdom

ARTICLE INFO

Keywords:

Computational methods
Microchannels
Two-phase flow
Boiling
Heat transfer

ABSTRACT

Boiling heat transfer in microchannels has been a very hot topic in heat transfer research over the past two decades, fuelled by the dramatic need for high heat flux cooling of miniaturised electronics and a number of high energy density applications. Two-phase numerical simulations have emerged as a very powerful tool to investigate fundamental fluid mechanics structures and heat transfer mechanisms, and thus complement experimental observations. Boiling flows in microchannels possess distinctive fluid dynamics features such as clear separation of liquid and gas phases, dominance of surface tension forces, very thin liquid films, that require tailored numerical models to achieve high-fidelity results. Hence, there has been growing interest towards computational developments and numerical studies, which has resulted in an extensive publication output. This article presents a comprehensive review of the vast literature of scientific papers dedicated to numerical simulations of boiling in microchannels. First, the most recent advances in traditional and emerging computational techniques for interface-resolved simulations of microchannel flows are reviewed, covering from macroscale models based on the solution of the continuum Navier–Stokes equations, to mesoscale and molecular dynamics models. The review then focuses on numerical studies that investigated the prevailing fluid dynamics features in microchannel flow boiling, such as the confined bubble dynamics, flow pattern development, conjugate heat transfer and flow instabilities deriving from multi-channel configurations. Last, the results of computational studies dedicated to practical applications in heat transfer enhancement through engineered surfaces and novel geometrical arrangements are illustrated. The review is then completed by providing recommendations for future two-phase computational research and by proposing a wishlist for experimental analyses. The main challenges for numerical simulations of flow boiling in microchannels remain the accurate estimation of surface tension forces which is paramount due to the dominance of capillarity, the availability of sub-grid thin film models applicable to flow boiling conditions made necessary by the disparity of scales between sub-micron thin films and channel sizes, and the physics-based modelling of nucleation which is currently missing in all continuum-scale models. A closer integration of simulation and experimental activities is recommended to design fundamental microchannel flow boiling experiments, where the initial and boundary conditions of the flow can be represented faithfully by simulations for validation of the numerical methods.

Contents

1.	Introduction	2
1.1.	State of the art of microchannel flow boiling research	2
1.2.	Scope of this review	4
2.	Computational methods for two-phase flows in microchannels	4
2.1.	Macroscale methods	5
2.1.1.	Advection of the marker function	5
2.1.2.	Numerical approximation of the Dirac delta	6
2.1.3.	Calculation of surface tension force	7
2.1.4.	Phase change models	7

* Corresponding author.

E-mail address: mirco.magnini@nottingham.ac.uk (M. Magnini).

2.1.5.	Sub-grid thin-film models.....	8
2.2.	Phase field method.....	10
2.3.	Lattice-Boltzmann method.....	10
2.4.	Molecular dynamics simulations.....	12
2.5.	Nucleation models.....	12
2.6.	Validation of computational methods for boiling in microchannels.....	13
2.6.1.	Analytical solutions for validation.....	13
2.6.2.	Experimental data for validation.....	13
2.7.	Boiling simulation software and computational cost.....	16
2.8.	Summary and challenges.....	18
3.	Fundamental analyses of microchannel flow boiling.....	19
3.1.	Flow patterns during flow boiling inside microchannels.....	19
3.1.1.	Confined bubble and elongated bubble flow.....	19
3.1.2.	Interaction between bubbles and bubble coalescence.....	21
3.1.3.	Flow pattern transitions and annular flow.....	25
3.2.	Conjugate heat transfer.....	27
3.3.	Multi-channel configurations.....	28
3.4.	Summary and challenges.....	29
4.	Applications: Heat transfer enhancement.....	30
4.1.	Micro-structured surfaces.....	31
4.2.	Enhanced wettability of boiling surfaces.....	32
4.3.	Enhanced geometry.....	33
4.4.	Summary and challenges.....	36
5.	Current status, challenges and future direction.....	36
6.	Conclusions.....	37
	Declaration of competing interest.....	37
	Data availability.....	37
	Acknowledgements.....	37
	References.....	37

1. Introduction

Flow boiling in microchannels has rapidly emerged in recent years as one of the most efficient cooling solutions for high-power-density applications, where heat fluxes well beyond 1 MW/m^2 must be dissipated through exchange areas of the order of 1 cm^2 , while maintaining uniform surface temperatures below technology-specific threshold values [1]. High-performance computers, power electronics, lasers, avionics, electric vehicles, batteries, photovoltaics, miniature fuel cells, energy conversion and storage systems, are some of the technologies where two-phase cooling is playing a crucial role to ensure efficient thermal management [2,3]. With the rapid increase of computational power witnessed in the past decades, numerical simulations of flow boiling in microchannels have been used to complement experimental research. This article presents a review of the methods, achievements and remaining challenges for numerical simulations of flow boiling in microchannels.

1.1. State of the art of microchannel flow boiling research

One of the major concerns related to the advancements in the miniaturisation of electronic systems, such as micro-electronic chips, and micro-electro-mechanical systems (MEMS), is the high heat generated due to ultra-dense circuitry in a single chip and multiple such devices placed in close proximity. The heat flux generated in such miniature systems can range from $50\text{--}100 \text{ W/cm}^2$ in the case of 3-D integrated chips [4] or highly-concentrated solar photovoltaics [5] to about $10^3\text{--}10^4 \text{ W/cm}^2$ with respect to electronics in defence radars or microwave weapons [6]. Such high heat fluxes result in a rapid increase in the surface temperature of the electronic components, which, in turn, can reduce their lifetime and performance. As shown in Fig. 1, among the different causes for the failure of electronics, high surface temperatures are recognised to be the most prominent one [7,8]. Hence, there is a need to have a thermal management system which can effectively dissipate such high heat generated while maintaining the optimum temperatures for efficient working of micro-electronic devices.

Cooling methods such as jet impingement [9], spray cooling [10], and microjet [11] have been tested by researchers to provide good thermal performance while removing heat generated in micro-electronic systems. These methods, however, are found to suffer from problems related to either high fluid pressure drops across the nozzles, or complex header connections. Hence, these cooling methods might not be suitable for applications within confined spaces. On the other-hand, there has been a growing interest in cooling using microchannel heat sinks since they are compact in size, provide higher heat transfer surface to volume ratios, and are observed to provide uniform wall temperature distributions at comparatively lower coolant flow rates as compared to the other cooling methods [12]. Further, much higher heat transfer coefficients have been obtained by employing two-phase cooling in a microchannel [6]. Hence, numerous experiments have been conducted by researchers to understand the heat transfer characteristics in two-phase flow boiling, comprehensive reviews of which can be found in the literature [13–16]. Considerable focus has also been given to enhance the heat transfer capabilities of the microchannel heat exchangers. A review of the effect of surface roughness and fluid additives has been carried out by Sidik et al. [17]. Xie et al. [18] have compiled a comprehensive review of methods to improve the critical heat flux of microchannels using nanoparticles and via nanoscale structuring of the microchannel surface. Liang and Mudawar [19] have summarised different passive techniques for heat transfer enhancement covering surface modifications from the nano- to the macroscales.

The design of efficient heat transfer elements for two-phase cooling requires reliable boiling heat transfer prediction methods. Since within microchannels the flow patterns have very distinctive features, phenomenological models based on a physics-based description of the interface topology pertinent to each flow pattern and of the underlying heat transfer mechanisms have proven more accurate than empirical correlations [20,21]. However, phenomenological prediction methods require precise descriptions of the prevailing flow features such as the thickness and distribution of thin liquid films in slug and annular flows within microchannels. Despite the recent advances in experimental methods for the diagnostics of two-phase flows in microchannels, the small spatial and temporal scales associated with these flows are

Nomenclature

a, b	Model constants	Ja	Jakob number, $\left(\frac{(T_\infty - T_{sat}) \rho_l c_{p,l}}{\rho_v h_{lv}}\right)$
A	Hamaker's constant	k	Thermal conductivity
Bd	Bond Number, $\left(\frac{g \Delta \rho D^2}{\sigma}\right)$	K	Thermal diffusivity, $(k/\rho c_p)$
Bo	Boiling Number, $(\dot{q}/G h_{lv})$	l_c	Interface thickness
c_s	Lattice speed sound	L_{heated}	Heated length of the channel
c_p	Specific heat at constant pressure	\dot{m}_Γ	Rate of interfacial mass transfer ($\text{kg}/\text{m}^2\text{s}$)
c_v	Specific heat at constant volume	M	Molecular weight of the fluid
C	Phase field parameter	Ma	Maranzana number, $\left(\frac{k_s e_w}{G c_{p,f} e_f L_{heated}}\right)$
Ca	Capillary number, $(\mu \mathbf{u}/\sigma)$	\mathbf{n}_Γ	Interface unit normal vector
Co	Confinement number, $\left(\sqrt{\frac{\sigma}{g \Delta \rho D^2}}\right)$	N_{Co}	Convection number, $\left(\frac{1-x_e}{x_e}\right)^{0.8} \left(\frac{\rho_v}{\rho_l}\right)^{0.5}$
D	Diameter	Nu	Nusselt number, $(h_{tp} D/k)$
D_h	Hydraulic diameter	p	Pressure
D_p	Diameter of pillar	P_{EOS}	Pressure equation of state
\mathbf{e}_i	Discrete velocity set	P_{HT}	Heated perimeter of the channel
e_w, e_f	Wall and channel thickness	P_{FT}	Wetted perimeter of channel
E	Rate of evaporation at the interface	P_r	Reduced pressure
E_m	Mixing energy of the system	Pr	Prandtl number, $(\mu c_p/k)$
f	Generic body force	\dot{q}	Heat flux
f_f	Friction factor	Q	Flux rate
f_σ	Surface tension force	r_c	Cutoff radius
F	Net force	r_i	Relaxation factor (s^{-1})
F_f	Fluid – fluid interaction force	r_{ij}	Distance between molecules
F_s	Fluid – solid interaction force	R_B	Radius of bubble
F_g	Gravitational force	R_Γ	Heat resistance at the interface
g	Gravitational acceleration	R_{gas}	Universal gas constant ($\text{J}/\text{mol K}$)
G	Mass flux ($\text{kg}/\text{m}^2\text{s}$)	Re	Reynold number, (GD/μ)
G_f	Fluid – fluid interaction strength	S_p	Pillar geometric factor
G_s	Fluid – solid interaction strength	T	Temperature
h	Film thickness	T_{sat}	Saturated temperature
h_e	Evaporative heat transfer coefficient	\mathbf{u}	Velocity
h_{cb}	Convective boiling heat transfer coefficient	U	Potential energy function
h_{lv}	Latent heat	V_{cell}	Computational cell volume
h_{nb}	Nucleate boiling heat transfer coefficient	W_p	Width of pillar
h_{sp}	Single phase heat transfer coefficient	We	Weber number, $(G^2 D/\rho \sigma)$
h_{tp}	Two phase heat transfer coefficient	x	x-coordinate
H	Heaviside step function	x_e	Thermodynamic equilibrium quality
H_p	Height of pillar	X_{tt}	Martinelli parameter, $\left(\frac{f_{f,l}}{f_{f,v}}\right)^{0.5} \left(\frac{1-x_e}{x_e}\right)^{0.8} \left(\frac{\rho_v}{\rho_l}\right)^{0.5}$
I	Marker function		
Greek symbols			
α	Volume fraction	ν	Kinematic viscosity
δ_Γ	Dirac delta function	ϕ	Level set function
ϵ	Potential well depth	Φ	Chemical potential
ϵ_{th}	Mean field thickness	ψ	Double well potential
ξ	Transformed spatial coordinate	Ψ	Pseudo-potential
γ	Evaporation coefficient	ρ	Density
κ	Mobility parameter	σ	Surface tension
κ_Γ	Liquid vapour interface curvature	σ_p	Molecular diameter
λ	Mixing energy density	τ	Relaxation time
μ	Dynamic viscosity	ω_i	Weight coefficient
Subscripts			
Γ	Interface	sat	Saturated
l	Liquid	v	Vapour
f	Fluid	w	Wall
s	Solid		
Abbreviations			
CSF	Continuum Surface Force	LS	Level Set
FT	Front Tracking	MD	Molecular Dynamics
GFM	Ghost Fluid Method	PF	Phase Field
LBM	Lattice Boltzmann Method	VOF	Volume of Fluid

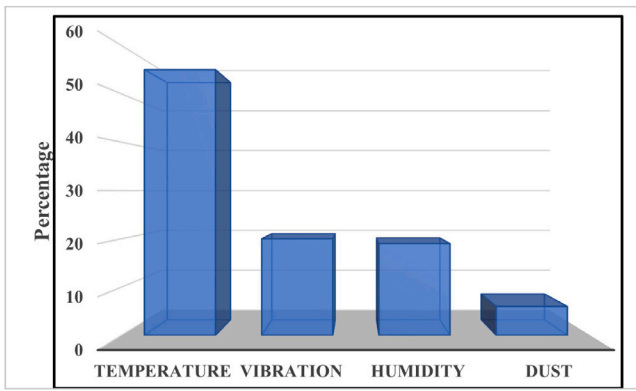


Fig. 1. Major causes for failure in electronics.

still not accessible to experiments. This has led to an increased use of numerical simulation software to elucidate fundamental aspects of multiphase fluid dynamics and heat transfer in miniature channels. The literature of numerical studies of boiling flows in small channels is vast and diversified, with focus ranging from algorithm development [22], to flow pattern based heat and mass transport [23–25], and enhanced heat transfer [26]. Review articles about computational studies of boiling and condensation do exist [27–29], however, there is a lack of up-to-date comprehensive reviews specifically dedicated to the numerical simulation of boiling in microchannels, covering both algorithmic development and applications. The objective of the present article is therefore to bridge this gap.

1.2. Scope of this review

Numerical simulation of boiling is not a new research area and the earliest studies addressing this topic can be dated back to the work of Lee and Nydahl [30] and Welch and Wilson [31]. However, boiling flows in microchannels possess distinctive fluid dynamics features that require ad hoc algorithmic developments compared to conventional channels or unconfined boiling flows (e.g. pool boiling). The precise definition of “microchannel” remains a topic of debate. Two main groups of definitions exist. The first group is based on the absolute size of the channel and considers microchannels as channels where two-phase flow mechanisms and thermal-hydraulic parameters, e.g. flow patterns, pressure drop, heat transfer coefficients, deviate significantly from larger scales or conventional size channels. Popular criteria in this group are those of Mehendale et al. [32], for which microchannels have hydraulic diameters below 0.1 mm based on considerations upon the surface-to-volume ratio of the channels, and that of Kandlikar and Grande [33] who considered microchannels as channels having diameter below 0.2 mm, according to manufacturing considerations. The second group attempts to introduce some physical reasoning into this criterion and considers microchannels as channels where surface tension effects dominate over buoyancy [34], as quantified by the confinement number:

$$Co = \sqrt{\frac{\sigma}{g\Delta\rho D^2}}, \quad (1)$$

where σ is the surface tension coefficient, g is the gravitational acceleration, $\Delta\rho$ is the liquid-to-gas density difference, and D is the channel diameter. An established criterion is to consider that for $Co > 0.5$ the channel corresponds to a microchannel [34].

From a computational modelling perspective, both definitions introduce specific challenges compared to boiling in conventional channels or pool boiling. When the confinement number is large, surface tension forces become dominant such that liquid and gas phases are well separated. Therefore, methods that resolve the two-phase interface

dynamics [35] become necessary as opposed to averaged Eulerian–Eulerian methods [36] typically adopted to model boiling in conventional channels, introducing the challenge of tracking and updating the interface position and topology. Within microchannels, heat transfer is governed by the thickness and evolution of thin liquid films that surround the long vapour bubbles in slug flow, or the high-speed vapour core in annular flow. The thickness of this liquid film determines the boiling heat transfer coefficient, which is usually calculated as inversely proportional to the film thickness [20]. Modelling thin liquid films requires algorithms that can deal with computational grids that are stretched in the direction of the flow to prevent excessive computational overhead [37]. Even so, these liquid films may reach thicknesses that are orders of magnitude smaller than the channel size before rupturing, as such mesh refinement is not always sufficient to adequately capture their evolution, thus requiring subgrid film modelling [38].

Furthermore, the high interface curvatures achieved in microchannel flows together with the interfacial resistance to heat transfer in very thin films may lead to temperature jumps at the interface that must be accounted for in phase change models [39,40]. Numerical methods for two-phase flows with surface tension suffer from spurious currents, which are unphysical flows appearing near interfaces due to errors in curvature calculations [41]. The magnitude of spurious currents scales with the inverse of the capillary number, and thus their impact is exacerbated in microchannel flows requiring specific mitigation strategies to yield reliable simulations [22]; these currents are usually negligible when simulating two-phase flows in conventional channels.

The main objective of this review is, therefore, to describe the specific algorithmic developments for flow boiling in microchannels that have been dedicated to addressing the challenges outlined above, following which we will review the achievements of the studies focused on essential two-phase flow aspects and heat transfer enhancement. The breadth of this review covers fundamentals to applications and it aims to constitute a valuable reference for researchers entering the field of numerical simulation of boiling flows in microchannels.

This review has been divided into three sections, as illustrated in Fig. 2. Section 2 concentrates on bringing together different numerical methods which have been employed by researchers to study flow boiling in microchannels, ranging from the molecular to the macroscale. Section 3 focuses on understanding flow boiling phenomena inside single and multiple microchannels. A review of different methods employed to achieve enhancement in heat transfer and reduce flow instability is presented in Section 4. Finally, the main outstanding challenges and future directions for computational research into microchannel flow boiling are summarised in Section 5.

2. Computational methods for two-phase flows in microchannels

Many different approaches to simulate the flow of two immiscible phases separated by an interface exist. In this review, these approaches are grouped according to the spatial scales they apply to. We refer to “macroscale methods” as those approaches that treat the fluid as a continuum and the interface separating immiscible fluids as a transition region of vanishing thickness for the fluid properties. These methods are suitable as long as the mesh size is sufficiently larger than the mean free path of the fluid molecules. Macroscale methods are based on the solution of the continuum Navier–Stokes equations and implement interfacial effects (e.g. surface tension, phase change) via closure models. Volume Of Fluid (VOF), Level Set (LS), Front Tracking (FT), are the most popular macroscale methods to simulate two-phase flows and are reviewed in Section 2.1. We refer to “microscale methods” as those approaches based on molecular dynamics (MD), where the kinetics of interacting molecules is resolved and thus any interfacial effect arises naturally from the intermolecular potential set; a brief review of these methods is provided in Section 2.4. In between, “mesoscale methods”

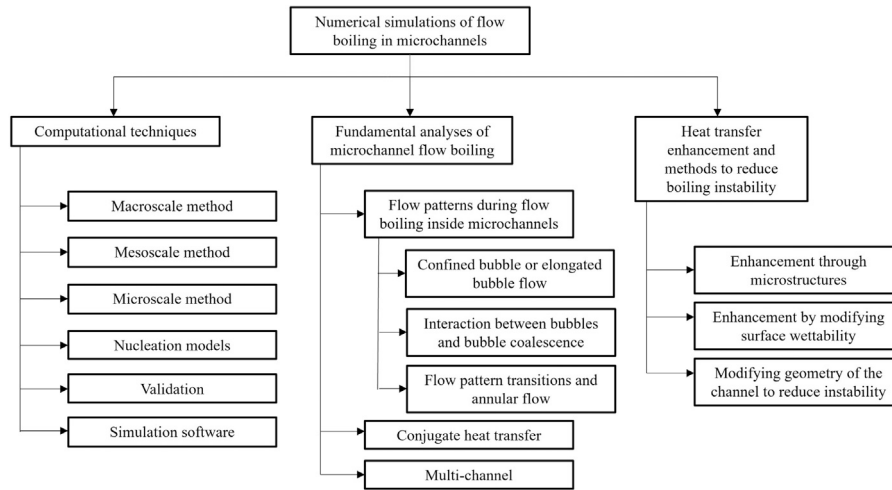


Fig. 2. Topics considered in the present review.

such as Phase Field (PF) and Lattice Boltzmann (LBM) methods capture the interface dynamics down to nanometres by modelling microscopic molecular interactions using thermodynamic (PF) or interparticle potentials (LBM), such that all interfacial effects arise naturally as part of the calculation without the need for closure models; these are reviewed in Sections 2.2 and 2.3. Section 2 is then completed by a discussion about the verification and validation of numerical models (Section 2.6), nucleation methods (Section 2.5), and available frameworks for boiling simulations (Section 2.7).

2.1. Macroscale methods

The most popular techniques for interface-resolved simulations of boiling two-phase flows are the Volume Of Fluid (VOF) [42], Level Set (LS) [43], and Front Tracking (FT) [44] methods. These methods solve the flow equations on a fixed grid, and model the two immiscible phases as a single fluid that occupies the whole domain with physical properties that change rapidly across the liquid-vapour interface. A marker function is then used to identify the different phases, the definition of which is specific to each method. Accordingly, a set of mass, momentum, and energy equations within the single-fluid formulation are written, and the effects of inter-phase mass transfer, latent heat, and surface tension are incorporated as source terms that act only at the interface. For the incompressible flow of a Newtonian fluid in boiling/condensation conditions, the flow equations are formulated as follows [35,39]:

$$\nabla \cdot \mathbf{u} = \left(\frac{1}{\rho_v} - \frac{1}{\rho_l} \right) \dot{m}_\Gamma \delta_\Gamma, \quad (2)$$

$$\frac{\partial(\rho \mathbf{u})}{\partial t} + \nabla \cdot (\rho \mathbf{u} \mathbf{u}) = -\nabla p + \nabla \cdot (\mu [\nabla \mathbf{u} + (\nabla \mathbf{u})^T]) + \rho \mathbf{g} + \sigma \kappa_\Gamma \mathbf{n}_\Gamma \delta_\Gamma, \quad (3)$$

$$\frac{\partial(\rho c_p T)}{\partial t} + \nabla \cdot (\rho c_p \mathbf{u} T) = \nabla \cdot (k \nabla T) - \dot{m}_\Gamma [h_{lv} + (c_{p,l} - c_{p,v})] \delta_\Gamma, \quad (4)$$

where \mathbf{u} denotes the fluid velocity, ρ the density, \dot{m}_Γ the rate at which liquid is converted into vapour, t the time, p the pressure, \mathbf{g} the gravitational acceleration, μ the dynamic viscosity; furthermore, T denotes the temperature, c_p the constant-pressure specific heat, k the thermal conductivity, and h_{lv} the latent heat. The last term on the right-hand side of Eq. (3) introduces the surface tension force according to the Continuum Surface Force (CSF) method [45], with σ being the surface tension coefficient, considered constant here though it could depend on T , and κ_Γ is the liquid-vapour interface curvature; \mathbf{n}_Γ denotes the interface unit normal vector. The Dirac delta function, δ_Γ , is nonzero only at the interface $\Gamma(t)$ and guarantees that the inter-phase source terms are active solely in that region; furthermore, δ_Γ can

be interpreted as an interface area density per unit volume, with units of 1/m. Further details about the formulation of δ_Γ are provided in Section 2.1.2.

The fluid properties appearing in the flow equations are calculated at every location based on the local value of the chosen marker function $I(\mathbf{x}, t)$, e.g. the density:

$$\rho(\mathbf{x}, t) = \rho_l I(\mathbf{x}, t) + \rho_v [1 - I(\mathbf{x}, t)], \quad (5)$$

where the subscripts l and v indicate, respectively, liquid and vapour specific properties, and we consider that $I(\mathbf{x}, t) = 1$ in the liquid phase and 0 in the vapour. To prevent numerical instability arising from large density and viscosity ratios, $I(\mathbf{x}, t)$ is usually smoothed over a few cells across the interface.

To preserve the velocity, pressure, and temperature discontinuities at the interface, the derivatives of \mathbf{u} , p , and T near the interface should be discretised either by one-sided differences or by employing the Ghost Fluid Method (GFM) [46,47]. With the GFM, the values of one field (e.g. \mathbf{u} , p , or T) on one side of the interface are extrapolated to the other side of the interface, thus creating ghost liquid cells in the vapour region and vice versa. The ghost cells values are obtained by directly imposing jump conditions across the interface, and the gradients on either side of the interface can be calculated by considering liquid-only or vapour-only cells [48].

2.1.1. Advection of the marker function

The definition of the marker function $I(\mathbf{x}, t)$, and thus its advection across the fixed grid is specific for each method. The VOF method uses the volume fraction α , which is defined as the fraction of the computational cell volume occupied by the primary phase, and thus it takes values between 0 to 1, and is $0 < \alpha < 1$ in cells containing both phases; an example is provided in Fig. 3(a). The volume fraction is transported as a passive scalar by the flow field. For flow with phase change, the transport equation can be formulated as follows [49,50]:

$$\frac{\partial \alpha}{\partial t} + \nabla \cdot (\mathbf{u} \alpha) = -\frac{1}{\rho_l} \dot{m}_\Gamma \delta_\Gamma, \quad (6)$$

here we consider $\alpha = 1$ in the liquid, and thus a positive mass transfer rate \dot{m}_Γ yields a negative source of volume fraction. The discretisation of the advection term of Eq. (6) is crucial to preserve the sharpness and boundedness (between 0 and 1) of α across the interface. There exist two categories of methods purposely devised for this task, namely geometric and algebraic methods. In geometric methods, the interface is clearly defined in cells where $0 < \alpha < 1$, using piecewise lines (in 2-D) or surfaces (3-D) [41,51]; the advection term $\nabla \cdot (\mathbf{u} \alpha)$ is then calculated geometrically, by reconstructing the volume fluxes across

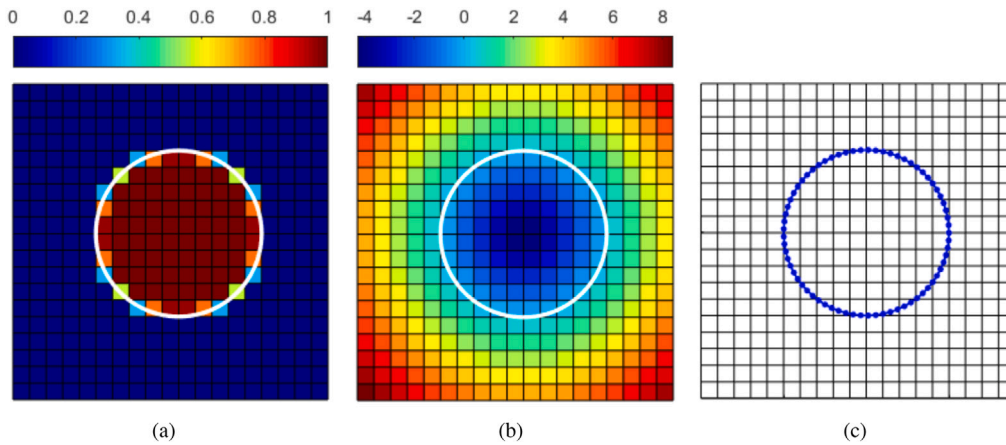


Fig. 3. Examples of (a) VOF volume fraction α field, (b) LS ϕ field and (c) FT marker points identifying a circular interface on a discretised domain. In (b), the level set function is normalised by the mesh size.

each boundary of the computational cell. In algebraic methods, the advection term is discretised by employing cell face-centred values of $(\mathbf{u}\alpha)$, regardless of the actual interface topology, which is unknown; flux-aware interpolation schemes [52–54] or sharpening techniques [55] are then used to maintain sharp gradients of α during the time-marching procedure.

Provided that the advection scheme is carefully implemented, the VOF method preserves mass to machine accuracy. Geometrical schemes ensure a sharp interface representation, with only one mixture cell ($0 < \alpha < 1$) between full-liquid and full-vapour cells, whereas with algebraic methods the interface appears smeared out over a few computational cells. On the other hand, algebraic methods are less computationally expensive and easier to implement for non-orthogonal and unstructured meshes. Geometric advection techniques for both momentum and energy fluxes in Eqs. (3) and (4) have been recently proposed by Fuster et al. [56] and Malan et al. [50], with the latter including also a novel two-step procedure to solve Eq. (6) by advecting the interface with a divergence-free extension of the liquid velocity field.

In the LS method, a level set function ϕ is defined as a signed distance function from the interface, so that $\phi = 0$ at the interface, $\phi > 0$ in one fluid and $\phi < 0$ in the other, as shown in Fig. 3(b). In the presence of phase change, the zero-level set curve is advanced by the interface velocity by solving the following equation [48,57–59]:

$$\frac{\partial \phi}{\partial t} + \mathbf{u}_{\Gamma} \cdot \nabla \phi = 0, \quad (7)$$

where \mathbf{u}_{Γ} is the interface velocity:

$$\mathbf{u}_{\Gamma} = \mathbf{u}_{\Gamma,v} - \frac{\dot{m}_{\Gamma}}{\rho_v} \mathbf{n}_{\Gamma} = \mathbf{u}_{\Gamma,l} - \frac{\dot{m}_{\Gamma}}{\rho_l} \mathbf{n}_{\Gamma}, \quad (8)$$

and $\mathbf{u}_{\Gamma,l}$ and $\mathbf{u}_{\Gamma,v}$ are, respectively, the liquid and vapour velocities at the interface. To avoid numerical instabilities, higher-order non-oscillatory schemes [60] are necessary to discretise the advection term in Eq. (7). Based on the field of ϕ , a Heaviside step function is reconstructed and used as the marker function for Eq. (5). At each time step, the level set function must be re-initialised to a distance function from the interface by solving an extra re-initialisation equation [43]. This procedure may yield artificial displacements of the $\phi = 0$ curve, and does not guarantee exact mass conservation. The LS method is often used in combination with the GFM to enforce the interface discontinuities arising in flows with phase change [48,58,59,61] because the exact knowledge of the interface location available (in terms of the locus of points corresponding to the $\phi = 0$ curve) facilitates the identification of the ghost fluid at each grid point.

In the FT method, the interface is represented as a set of connected marker points (the front) that are moved by the fluid in a Lagrangian fashion, as shown in Fig. 3(c). Eqs. (2)–(4) are solved on the fixed mesh

and the resulting velocity field is interpolated onto the front grid points to update their position by integrating [39,62]:

$$\frac{d\mathbf{x}_{\Gamma}}{dt} = (\mathbf{u}_{\Gamma} \cdot \mathbf{n}_{\Gamma}) \mathbf{n}_{\Gamma}, \quad (9)$$

where $\mathbf{u}_{\Gamma} \cdot \mathbf{n}_{\Gamma}$ is the normal velocity of the interface:

$$\mathbf{u}_{\Gamma} \cdot \mathbf{n}_{\Gamma} = \frac{1}{2} (\mathbf{u}_{\Gamma,l} + \mathbf{u}_{\Gamma,v}) \cdot \mathbf{n}_{\Gamma} - \frac{\dot{m}_{\Gamma}}{2} \left(\frac{1}{\rho_l} + \frac{1}{\rho_v} \right), \quad (10)$$

where $\mathbf{u}_{\Gamma,l}$ and $\mathbf{u}_{\Gamma,v}$ are the liquid and vapour velocities at the interface, obtained via interpolations from the fixed grid to the moving front. Interfacial effects such as interphase mass and heat transfer and surface tension are calculated on the moving front and then transferred to the fixed grid so they can be included in Eqs. (2)–(4). The fixed-to-front grid and front-to-fixed grid communications are done using Peskin distribution functions [63]. Based on the location of the marker points, at each time step, a Heaviside step function is reconstructed [39] and used as the marker function for Eq. (5). The FT has the great advantage that the interfacial effects can be calculated very accurately on the front grid; on the other hand, the interface advection does not guarantee mass conservation and non-trivial front re-meshing methods must be implemented to handle large interface deformations.

2.1.2. Numerical approximation of the Dirac delta

The use of delta functions enables the implementation of interphase mass transfer, latent heat and surface tension into the single-fluid flow equations, Eqs. (2)–(4), as volumetric source terms. The approximation of δ_{Γ} on the computational mesh is specific for each interface advection method. In VOF, $\delta_{\Gamma} = |\nabla \alpha|$ [45]; in LS, $\delta_{\Gamma} = dH/d\phi$ with H being a mollified Heaviside function [64]; in FT, δ_{Γ} can be reconstructed using distribution functions [39]. These methods naturally smooth the delta function over 2–3 mesh cells across the interface, thus benefitting numerical stability, but compromising the sharp nature of the interfacial exchange. An alternative formulation proposed by Sato and Niceno [65] is to interpret δ_{Γ} as an interface area density and thus calculate it only in cells cut by the interface as $\delta_{\Gamma} = A_{int}/V_{cell}$, where A_{int} is the geometrically-calculated area of the liquid-vapour interface and V_{cell} is the computational cell volume, thus ensuring a sharp representation of the source terms. A sharp alternative to the use of delta functions is the Ghost Fluid Method [46], where the mass, momentum and energy jump conditions at the interface are directly included in the discretisation of the gradients of pressure, velocity and temperature at the interface [48,58,59,61,66,67], thus enforcing phase change mass transfer and surface tension as boundary conditions at the interface without any smoothing.

2.1.3. Calculation of surface tension force

The surface tension force formulated via the CSF method of Brackbill et al. [45], see Eq. (3), involves the calculation of the local interface curvature κ_Γ and unit normal \mathbf{n}_Γ . These parameters can be calculated accurately with the LS method, because ϕ is a smooth function across the interface (Fig. 3(b)) and can be differentiated to evaluate both the interface normal as $\mathbf{n}_\Gamma = \nabla\phi/|\nabla\phi|$ and $\kappa_\Gamma = \nabla \cdot \mathbf{n}_\Gamma$ [43]. Surface tension is estimated very accurately also in the FT method, as the interface topology can be reconstructed via differential geometry of the discrete surface constituted by the front points [35]. In the context of the VOF method, the interface topology can in principle be reconstructed using volume fractions, $\mathbf{n}_\Gamma = \nabla\alpha/|\nabla\alpha|$ and $\kappa_\Gamma = \nabla \cdot \mathbf{n}_\Gamma$ [45]. However, the volume fraction is a discontinuous function at the interface, see Fig. 3(a), which makes finite-difference approximations of $\nabla\alpha$ very inaccurate. This leads to poor estimations of the interface normal vector, and errors in the curvature that tend to increase with spatial resolution [22]. Different smoothing techniques for α have been initially proposed to improve the calculations [45,68], but with limited efficacy. More recent methods performing a local geometrical reconstruction of the interface have proven much more powerful, for example employing reconstructed distance functions [68], parabolic reconstructions [69], or the Height Function method [22,70].

The drawback of these more accurate methods is that their use is often limited to orthogonal meshes. Sussman and Puckett [71] devised a coupled LS and VOF algorithm, which combines the mass conservation of geometric VOF and the accurate curvature calculation of LS. This has been recently extended to arbitrary meshes by employing an algebraic VOF advection by Dianat et al. [72] and Ferrari et al. [37]; the latter also proposed a consistent calculation of the LS Heaviside function for high aspect ratio mesh cells, such as those utilised for microchannel film flows. Algorithms exploiting machine learning to estimate curvatures from volume fractions for uniform meshes have also been proposed [73,74].

The implementation of the surface tension force is prone to the generation of spurious currents, artificial flows appearing near the interface despite the absence of any external forcing [41]. In flows with phase change, these may provide an artificial convective contribution to heat transfer and enhance the interfacial mass transfer rate [40]. It has been observed that the magnitude of the spurious velocity scales with the inverse of the capillary number of the flow [41,75], and therefore their impact is particularly detrimental in simulations of microchannel flows. For example, Fig. 4 shows the streamlines and vorticity field near the interface appearing in a numerical simulation of an elongated bubble flowing in a microchannel [75]. When the interface curvature is calculated using the level set function, Fig. 4(b), one single recirculation vortex is established in the liquid slug between two consecutive bubbles, in agreement with experimental data [76]. However, when the VOF method is used and κ_Γ is computed based on derivatives of α , Fig. 4(a), larger vorticity values are observed and one additional recirculation loop appears at the bubble nose, which is a result of numerical errors.

Spurious currents originate from the numerical imbalance of the surface tension force and the associated pressure gradient in Eq. (3), which is caused by: (i) poor estimations of the interface curvature, (ii) different discretisation schemes applied to ∇p and $\sigma\kappa_\Gamma\mathbf{n}_\Gamma\delta_\Gamma$ [66,70], and (iii) curvature estimations depending on the mesh-interface relative orientation [77]. Strategies to mitigate the magnitude of spurious currents include more accurate curvature calculation algorithms, such as those described above for the VOF method, well-balanced numerical schemes capable of recovering the exact numerical equilibrium between pressure gradient and surface tension force [66,70,75], and the use of rotating stencils to reconstruct the interface topology independently of its orientation [78,79]. The review by Popinet [67] summarises the recent developments on numerical models for surface tension-driven interfacial flows.

2.1.4. Phase change models

The phase change model has the task of computing the rate of interfacial mass transfer \dot{m}_Γ , based on the local temperature and pressure fields. The most popular method in interface-resolved simulations evaluates \dot{m}_Γ based on the energy jump condition at the interface [80]:

$$\dot{m}_\Gamma = \frac{\dot{\mathbf{q}}_\Gamma \cdot \mathbf{n}_\Gamma}{h_{lv}} = \frac{[k_v(\nabla T)_{\Gamma,v} - k_l(\nabla T)_{\Gamma,l}] \cdot \mathbf{n}_\Gamma}{h_{lv}}, \quad (11)$$

where $\dot{\mathbf{q}}_\Gamma$ is the heat flux at the interface and $(\nabla T)_{\Gamma,v}$, $(\nabla T)_{\Gamma,l}$ indicate the gradients on either side of the interface. The correct evaluation of one-sided temperature gradients in Eq. (11) is paramount, because the heat flux is discontinuous at the interface and any smoothing of this vector will distort the mass transfer rate [31,48]. The mass flux \dot{m}_Γ is defined only in cells cut by the interface, and the temperature gradients normal to the interface are typically calculated using the normal probe technique introduced by Udaykumar et al. [81]:

$$(\nabla T)_{\Gamma,p} \cdot \mathbf{n}_\Gamma = \frac{T_p - T_\Gamma}{d_\Gamma}, \quad (12)$$

where T_Γ is the interface temperature and T_p (with $p = l, v$) is the temperature calculated at the end of a line segment normal to the interface, at a distance d_Γ from the interface; see schematic in Fig. 5. For a sharp definition of the gradients, it is important that T_p is taken in liquid-only or vapour-only cells, and therefore d_Γ is usually one-two grid spacings away from the interface. When using this method for boiling flows [31,48,50,58,82], the interface temperature T_Γ is usually taken equal to the saturation temperature T_{sat} corresponding to the system pressure, under the assumption that temperature is continuous across the interface.

Another popular approach is based on the assumption that temperature and pressure are discontinuous at the interface and calculates \dot{m}_Γ according to the kinetic gas theory. The original model equation is often referred to as the Hertz-Knudsen-Schrage model [83] and estimates interphase mass transfer based on the liquid and vapour temperatures at the interface; Tanasawa [84] derived the following linearised version which is more suitable for implementation in macroscale simulation techniques:

$$\dot{m}_\Gamma = \frac{T_\Gamma - T_{sat}}{R_\Gamma h_{lv}}, \quad (13)$$

where R_Γ is the heat resistance at the interface:

$$R_\Gamma = \frac{2 - \gamma}{2\gamma} \left(\frac{2\pi R_{gas}}{M} \right)^{1/2} \frac{T_{sat}^{3/2}}{\rho_v h_{lv}^2}. \quad (14)$$

For boiling, γ denotes the evaporation coefficient, defined as the fraction of molecules that depart the interface during evaporation ($\gamma = [0, 1]$); M is the molecular weight of the fluid and R_{gas} the universal gas constant. In the original work of Tanasawa [84], where Eq. (13) was used for film condensation of metal vapour, T_{sat} referred to the (vapour) saturation temperature at the system pressure. Hardt and Wondra [40] were the first to utilise Eq. (13) in interface-resolved numerical simulations of boiling flows, also including a specific smoothing method for the related source terms to improve numerical stability. Since then, this method has been applied by several authors to study nucleate boiling [49,85] and microchannel flow boiling [22,86] with good agreement with experimental data. A key challenge of the model is the choice of the value for the evaporation coefficient, as γ is only known with a large degree of uncertainty even for the most common fluids [84]. Validation tests exhibit best agreement with analytical solutions when $\gamma = 1$ [22,40,49], whereas values in the range $\gamma = 0.01 - 1$ have been used to match experimental data [29]. Values of the evaporation/condensation coefficients have also been obtained via molecular dynamics simulations [87,88].

Another widely used phase change model was developed by Lee [89] in which phase change is calculated based on the temperature difference between the local liquid cell temperature and the saturated

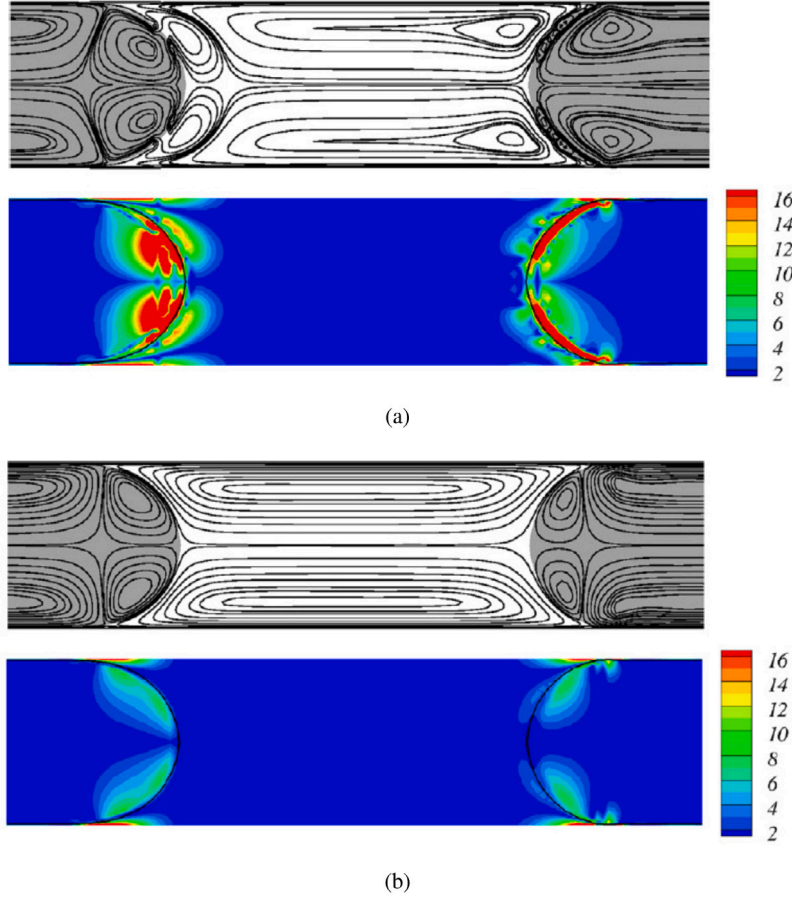


Fig. 4. Streamlines and vorticity field for the flow of an elongated bubble in a microchannel with a capillary number of $Ca = 0.002$ ($Ca = \mu_l U / \sigma$). (a) Simulation is done using an algebraic VOF method with interface curvature calculated as $\kappa_\Gamma = \nabla \cdot (\nabla\alpha/|\nabla\alpha|)$, and (b) using a LS method with $\kappa_\Gamma = \nabla \cdot (\nabla\phi/|\nabla\phi|)$.
Source: Figure from Abadie et al. [75].

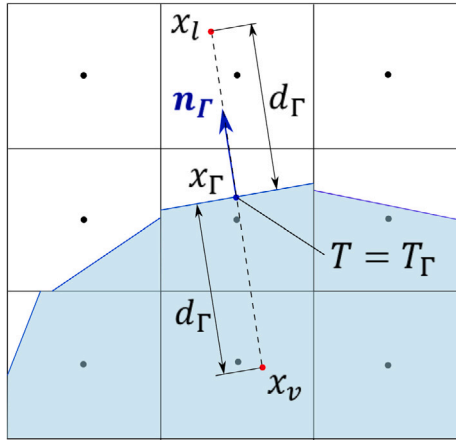


Fig. 5. Schematic of the normal probe technique [81] to reconstruct one-sided temperature gradients at a liquid-vapour interface. The temperature at the centre x_Γ of the reconstructed interface line is T_Γ . Temperatures T_l and T_v to be used in Eq. (12) are evaluated at a distance d_Γ from x_Γ , along the interface normal direction. T_l and T_v at x_l and x_v are calculated as averages of the neighbour cell centres temperatures.

temperature of the fluid. The mass transfer (m_Γ) in the Lee model is calculated as shown below,

$$\dot{m}_\Gamma = r_i \alpha_l \rho_l \frac{T_l - T_{sat}}{T_{sat}}, \quad (15)$$

where α_l and ρ_l are volume fraction and density of liquid; r_i is a relaxation factor with units of s^{-1} . The Lee model does not set any limit on the value of r_i and its value depends on various factors including operating conditions such as heat flux, mass flux, the fluid being considered, the geometry and mesh size. Lorenzini and Joshi [90] tested different r_i values ranging from 10 to $100 s^{-1}$ for their simulation of flow boiling of R245fa inside a micro-gap and found that a value of $50 s^{-1}$ worked well for their case. Lee et al. [91] compared different values of r_i in the range 1–100 during subcooled flow boiling of FC-72 inside channels of 5 mm height and obtained good agreement with the experimental results with a value of $10 s^{-1}$. These values could be taken as initial assumptions for microchannel simulations, but comparison with experimental data is necessary for an optimal tuning of r_i . The Lee model implements the mass source term already as a volumetric effect without multiplication by δ_Γ , and thus it computes a nonzero source term both across the interface and within the bulk liquid. Therefore, bubbles can nucleate in any point of the domain where $T_l > T_{sat}$ without the need to seed them.

2.1.5. Sub-grid thin-film models

Within microchannels, surface tension rearranges the liquid-vapour interface pattern into wall-bounded thin liquid films, whose thickness can be several orders of magnitude smaller than the channel hydraulic diameter D_h . For example, the film thickness h surrounding a long vapour bubble translating in water at $T_{sat} = 100^\circ C$, with mass flux $G = 100 \text{ kg}/(\text{m}^2 \text{ s})$, can be estimated using Bretherton [92] theory for circular channels as $h/D_h = 0.67Ca^{2/3} \approx 0.005$ (with $Ca = \mu_l G / (\rho_l \sigma) \approx 0.0007$); this film becomes even thinner in noncircular channels [93], and may eventually dry for non-wetting fluids [94] or under evaporation

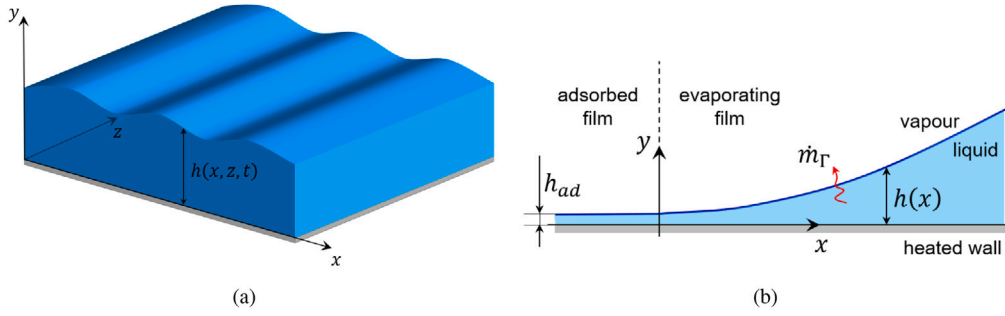


Fig. 6. (a) Sketch of a liquid film flowing along a flat wall and (b) one-dimensional representation of an evaporating thin-film evolving from a nonevaporating adsorbed film region of thickness h_{ad} to an outer meniscus.

conditions [95]. Therefore, resolving the thin film region with the same computational mesh used to discretise Eqs. (2)–(4) across the whole domain is often a prohibitive task.

A popular way forward is to assume the existence of an unresolved thin-film in a micro-region near the wall, where the flow equations are simplified using the lubrication approximation and solved on a separate sub-grid mesh, and use this sub-grid solution to adjust boundary conditions and source terms in Eqs. (2)–(4). Let $h(x, z, t)$ be the liquid film thickness measured as the distance from the channel wall, with x and z denoting orthogonal coordinates measured along the wall; see the sketch in Fig. 6(a). At leading-order, the mass balance in the liquid film writes as [96,97]:

$$\frac{\partial h}{\partial t} + \nabla \cdot \mathbf{Q} + E = 0, \quad (16)$$

where ∇ is a two-dimensional operator in (x, z) . The flux rate \mathbf{Q} can be expressed from the knowledge of the velocity field, which at leading-order is two-dimensional in (x, z) and described by:

$$\mathbf{u} = \frac{1}{2\mu_l}(y^2 - 2hy)\nabla p_l, \quad (17)$$

obtained by imposing the boundary conditions $\mathbf{u} = 0$ at $y = 0$ and $\partial \mathbf{u} / \partial y = 0$ at $y = h$ whence the flow rate \mathbf{Q} can be computed from:

$$\mathbf{Q} = \int_0^h \mathbf{u} dz = -\frac{h^3}{3\mu_l} \nabla p_l. \quad (18)$$

The pressure in the film p_l is constant along y and $p_l(x, z)$ includes contributions from surface tension and disjoining pressure [98]:

$$p_l = p_v - \sigma \kappa_\Gamma - \frac{A}{h^3}, \quad (19)$$

where the pressure in the vapour p_v is assumed constant, κ_Γ is the interface curvature and can be expressed as a function of h and its derivatives [99], and A is the Hamaker constant. The term E in Eq. (16) denotes the rate of evaporation at the interface and is calculated as $E = \dot{m}_\Gamma / \rho_l = \dot{q}_\Gamma / (\rho_l h_{lv})$, with \dot{q}_Γ being the heat flux at the interface. The latter can be written using Fourier's law, from the knowledge of the temperature field within the film which, at leading-order, is governed by heat conduction:

$$T = T_w - \frac{T_w - T_{\Gamma,v}}{h + k_l R_\Gamma} y, \quad (20)$$

where T_w is the wall temperature and R_Γ is the heat resistance at the interface defined in Eq. (14); $T_{\Gamma,v}$ is the vapour temperature at the interface, which may deviate from T_{sat} owing to capillary and disjoining pressure effects [98]:

$$T_{\Gamma,v} = T_{sat} \left(1 + \frac{\sigma \kappa_\Gamma + A/h^3}{\rho_l h_{lv}} \right). \quad (21)$$

This leads to the following expression for the rate of evaporation E :

$$E = \frac{T_w - T_{sat} \left[1 + (\sigma \kappa_\Gamma + A/h^3) / (\rho_l h_{lv}) \right]}{\rho_l h_{lv} (h/k_l + R_\Gamma)}, \quad (22)$$

and, finally, to a fourth-order partial differential equation for $h(x, z, t)$:

$$\frac{\partial h}{\partial t} + \frac{1}{3\mu_l} \nabla \cdot \left[h^3 \nabla \left(\sigma \kappa_\Gamma + \frac{A}{h^3} \right) \right] + \frac{T_w - T_{sat} \left[1 + (\sigma \kappa_\Gamma + A/h^3) / (\rho_l h_{lv}) \right]}{\rho_l h_{lv} (h/k_l + R_\Gamma)} = 0. \quad (23)$$

The equation above has been solved as a sub-grid model coupled with the full Navier–Stokes equations by Abu-Al-Saud et al. [100] and Rajkotwala [101], although for flows without phase change ($E = 0$). In these works, the solution of Eq. (23) was activated when the film thickness fell below a certain tolerance dictated by the near-wall mesh size. The sub-grid solution was then used to set partial slip boundary conditions to the momentum Eq. (3) at the wall, where the film was too thin to be resolved by the computational mesh.

A number of authors have simplified Eq. (23) by assuming steady-state and a one-dimensional geometry, to study heat transfer near contact lines [38,98,102]; see the sketch in Fig. 6(b). Using these assumptions, $h \equiv h(x)$ only and Eq. (23) becomes an ordinary differential equation (ODE):

$$\frac{1}{3\mu_l} \frac{d}{dx} \left[h^3 \frac{d}{dx} \left(\sigma \kappa_\Gamma + \frac{A}{h^3} \right) \right] + \frac{T_w - T_{sat} \left[1 + (\sigma \kappa_\Gamma + A/h^3) / (\rho_l h_{lv}) \right]}{\rho_l h_{lv} (h/k_l + R_\Gamma)} = 0. \quad (24)$$

Ajaev and Homsy [38] solved Eq. (24) using a shooting method to study steady vapour bubbles advancing in rectangular channels, with boundary conditions $h = h_{ad}$ and $h', h'' = 0$ near a nonevaporating adsorbed film region of thickness h_{ad} , and asymptotic conditions $\kappa_\Gamma \rightarrow \kappa_\infty$ as $x \rightarrow \infty$ and the interface approaches the static meniscus at the channel corner. Kunkelmann and Stephan [49] solved Eq. (24) by turning it into a set of four coupled first-order ODEs with unknowns $h, h', \Delta p = p_v - p_l$, and an integrated heat flux \dot{q} . The equations were integrated from the adsorbed film region with initial conditions $h = h_{ad}, h' = 0, \Delta p = A/h_{ad}^3, \dot{q} = 0$, until a prescribed value of x sufficiently large for disjoining pressures to become negligible. Son et al. [103] solved Eq. (24) to simulate nucleate boiling with boundary conditions $h = h_{ad}$ and $h', h'' = 0$ near the adsorbed region and $h'' = 0$ at a location x where $h = \Delta/2$, with Δ being the size of the near-wall mesh cell. In both Kunkelmann and Stephan [49] and Son et al. [103], the extension of the micro-region was smaller than the grid size and the thin-film model provided the mass and energy source terms for Eqs. (2) and (4) in contact line cells only.

Simplified versions of Eq. (24) have been adopted by other authors to simulate nucleate boiling [104], also including empirical modifications to emulate a thin-film spanning the entire near-wall region beneath the bubble [105,106]. Chen et al. [107] were the first to implement a subgrid microlayer model to simulate flow boiling in a microchannel. The model was semi-empirical and considered different film dynamics and depletion mechanisms depending on whether the microlayer developed beneath small bubbles (of radius smaller than the channel size) or elongated bubbles.

2.2. Phase field method

The computational techniques discussed in Section 2.1 are essentially sharp-interface approaches wherein the interface is assumed to be of zero thickness. In the Phase Field (PF) method, the interface between two immiscible fluids is considered to be a transition region of finite thickness. This approach builds on ideas proposed originally by Rayleigh [108] and van der Waals [109] wherein the interface is described by mixing energy. The gradual change in the phase field allows for a more natural representation of interfaces and inherently accounts for thermodynamic effects associated with phase transitions, such as surface tension and energy minimisation. A phase field parameter C is used to identify the phase in an incompressible two-phase fluid system with $C = 1$ for liquid, $C = -1$ for gas, and $-1 < C < 1$ at the interface. A number of Phase Fields methods have been proposed for boiling flows, see for example Liu et al. [110] for a brief review and Badillo [111] for a PF model based on the Allen-Cahn formulation. Below we focus on the Cahn-Hilliard formulation that has been successfully used to simulate boiling in a microchannel [112]. The Cahn-Hilliard equation is based on an energetic variational approach in which a two-phase system is characterised by the free energy of the system and diffusion at the interface is proportional to the gradient of the chemical potential Φ [113]:

$$\frac{\partial C}{\partial t} + (\mathbf{u} \cdot \nabla)C = \kappa \nabla^2 \Phi, \quad (25)$$

where, \mathbf{u} is the flow velocity and κ is the mobility parameter that controls the diffusion process. The chemical potential is defined as the rate of change of mixing energy of the system E_m with respect to C :

$$\Phi = \frac{\partial E_m}{\partial C}. \quad (26)$$

Cai et al. [114] modelled the mixing energy of the system based on the Helmholtz free energy [109]:

$$E_m = \int_V \left(\frac{1}{2} a (\nabla C)^2 + b \psi(C) \right) dV, \quad (27)$$

where V is the system domain, a and b are positive model constants, while ψ is the double-well potential defined as $\psi = \frac{1}{4} (C + 1)^2 (C - 1)^2$. Equilibrium interface profiles can be obtained by minimising the mixing energy of the system. In one-dimensional flow involving a planar interface, the variation of C at the interface is given by,

$$C = \tanh \left(\frac{x}{\sqrt{2} \epsilon_{th}} \right), \quad (28)$$

where ϵ_{th} is the mean field thickness defined as $\epsilon_{th} = \left(\frac{a}{b} \right)^{0.5}$. Jamshidi et al. [115] showed that in 1-D, if $-0.9 < C < 0.9$ is taken as a diffuse interface, then the interface thickness (l_C) where the properties change rapidly but smoothly is given by $l_C = 4.164 \epsilon_{th}$.

In the phase field method, the thermophysical properties depend on the order parameter C , and can be calculated as shown below:

$$\begin{aligned} \rho &= \frac{\rho_v + \rho_l}{2} + \frac{\rho_v - \rho_l}{2} C, & \mu &= \frac{\mu_v + \mu_l}{2} + \frac{\mu_v - \mu_l}{2} C, \\ c_p \rho &= \frac{c_{p,v} \rho_v + c_{p,l} \rho_l}{2} + \frac{c_{p,v} \rho_v - c_{p,l} \rho_l}{2} C, & k &= \frac{k_v + k_l}{2} + \frac{k_v - k_l}{2} C. \end{aligned} \quad (29)$$

Instead of the CSF model used in the macroscale methods discussed above, the surface tension force here is modelled with respect to the order parameter and chemical potential as $\mathbf{f}_\sigma = C \nabla \Phi$.

Using the phase field method described above, Dong and Shen [116] developed an algorithm to address multiphase simulations with high-density ratios. Zheng et al. [117] have also used a similar algorithm to simulate two-phase heat transfer in 3-D. Wang et al. [112] followed the same algorithm but modified the governing equations to include phase change:

$$\nabla \cdot \mathbf{u} = m_I \left(\frac{1}{\rho_v} - \frac{1}{\rho_l} \right). \quad (30)$$

Here m_I is the vaporisation rate. The model used by Wang et al. [112] to incorporate phase change based on the energy balance at the interface is as shown below:

$$m_I = \frac{k_v \nabla T \cdot \mathbf{n}_\Gamma}{h_{lv}}, \quad (31)$$

here, $\mathbf{n}_\Gamma = \frac{\nabla C}{|\nabla C|}$. If the temperature on the vapour side is equal to the saturation temperature, then the vaporisation rate is defined as:

$$m_I = - \frac{k_l \nabla T \cdot \mathbf{n}_\Gamma}{h_{lv}}, \quad (32)$$

where h_{lv} is the specific latent heat of vaporisation.

So, the governing equations are given as follows:

$$\frac{\partial \mathbf{u}}{\partial t} + \mathbf{u} \cdot \nabla \mathbf{u} = - \frac{\nabla p}{\rho} + \frac{\mu}{\rho} \nabla^2 \mathbf{u} + \frac{\mu}{\rho} \nabla (\nabla \cdot \mathbf{u}) + \frac{\nabla \mu}{\rho} \cdot (\nabla \mathbf{u} + \nabla \mathbf{u}^T) - \frac{\lambda}{\rho} (\nabla^2 C) \nabla C + \frac{\mathbf{f}}{\rho}, \quad (33)$$

$$\frac{\partial C}{\partial t} + \mathbf{u} \cdot \nabla C = - \lambda \kappa \nabla^2 [\nabla^2 C - \psi] + m_I \left(\frac{1-C}{\rho_v} + \frac{1+C}{\rho_l} \right), \quad (34)$$

$$\frac{\partial T}{\partial t} + \mathbf{u} \cdot \nabla T = \frac{k}{\rho c_p} \nabla^2 T + \frac{1}{\rho c_p} \nabla k \cdot \nabla T - \frac{\dot{\mathbf{q}}_\Gamma - \dot{\mathbf{q}}_c}{\rho c_p}, \quad (35)$$

where \mathbf{f} is a generic body force, $\lambda = \frac{3}{2\sqrt{2}} \sigma \epsilon_{th}$ is the mixing energy density and $\dot{\mathbf{q}}_\Gamma = -m_I h_{lv}$. A coupled solution of momentum and enthalpy equations alongside mass conservation leads to the heating of liquid and the cooling of vapour within the evaporation zone. This process induces a temperature peak at the interface between the two phases which is an artefact caused by the structure of mass-source term and is removed by introducing the correction term $\dot{\mathbf{q}}_c = m_I (T - T_{sat}) c_p$ in the temperature equation. With this approach, Wang et al. [112] simulated vapour bubble growth in a superheated liquid wherein they observed that a smooth spherical shape of the bubble can be maintained with velocity vectors uniformly pointing in the radial direction using Phase Field method. This can be seen in Fig. 7(a), wherein the shape of the bubble at two different time steps is shown and the spherical shape of the bubble has been maintained over the time. Further, they also simulated the growth of a single bubble inside a rectangular channel as depicted in Fig. 7(b). They compared their results with the Mukherjee et al. [118] experiments and obtained a good agreement with the experimental results.

With Phase Field, adequate grid refinement should be ensured in the interfacial region, with at least 6 cells required for the resolution of diffused interface, for accurately predicting the state of the bubble [119]. Though the Cahn-Hilliard phase field method conserves mass better than the level set method, it still does not conserve mass as accurately as the VOF method. Jamshidi [120] observed this error in mass conservation when they compared the results of the VOF and phase field method while performing a 2-D simulation of a motionless air bubble in stagnant water. They tested bubble diameters ranging from 250 μm to 1 mm, and observed that this issue became more prevalent as the bubble size was reduced. They reported that the mass conservation issues can be controlled by having a smaller Cahn number (ratio of interfacial thickness to the characteristic length scale of the bubble). This implies the necessity of having a finer grid and smaller time-steps despite the increase in computational cost.

2.3. Lattice-Boltzmann method

Particle-based discrete methods such as the Lattice Boltzmann method (LBM), have gained interest in the last decade as a mesoscale approach for simulating phase change problems. LBM is a mesoscopic method based on the kinetic Boltzmann equation [121] which can handle interfacial dynamics of multiphase flow by incorporating inter-molecular interactions [122,123] without the need for interface tracking, which greatly reduces the computational costs. Moreover, it has been shown that the automatic nucleation of bubbles can be

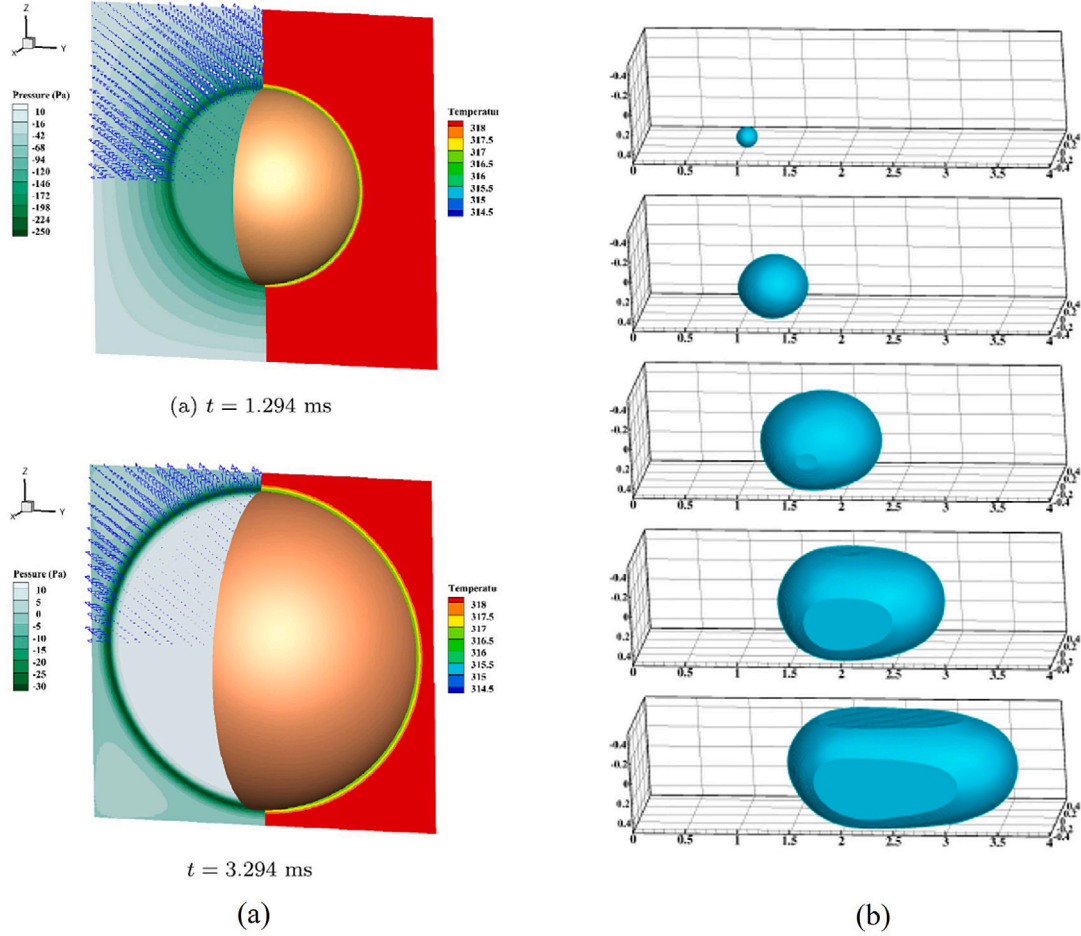


Fig. 7. Simulations of boiling flows performed using the Phase Field method: (a) bubble growth in superheated liquid; (b) temporal evolution of a vapour bubble in a microchannel [112].

achieved in LBM via the natural evolution of the energy equation [124, 125]. Hence, LBM can be used to acquire a boiling curve directly without the need for any artificial initiation of bubble nuclei and has been widely used in simulating pool boiling cases [126–129].

Among the different LB models developed for multiphase simulations, the pseudo-potential LB model and the phase field model have been widely used for simulating boiling cases for fluids with large density ratios [130–133]. Comprehensive review of the different LB methods available and their application related to different multiphase flow problems can be found in Li et al. [134] and Chen et al. [135]. Here, the pseudo-potential model will be discussed since this model has been widely used for boiling simulations. The pseudo potential model was devised by Shan and Chen [123] in which separation of fluid phases can be obtained automatically since the fluid interactions are mimicked by inter-particle potentials [136]. For boiling simulations using a pseudo-potential model, mainly two types of methods have been followed. One method, developed by Gong and Cheng [126], involves using separate distribution functions for solving multiphase flow and energy equations coupled with an equation of state. Li et al. [137], however, recognised that there are inherent numerical stability and accuracy issues with such an approach. Hence, they developed a hybrid LBM in which a pseudo-potential model is used for solving fluid flow while the energy equation was solved using a finite difference scheme.

According to the LBM methodology, the evolution of the density and velocity is realised in two steps, namely, collision and streaming. The collision step is modelled as,

$$f_i^*(x, t) = f_i(x, t) - \frac{1}{\tau}(f_i(x, t) - f_i^{eq}(x, t)) + \Delta f_i(x, t), \quad (36)$$

Here, $f_i(x, t)$ is the distribution function in the i^{th} direction on location x at time t . The superscript * and eq denote the after-collision and the equilibrium states, respectively. The relaxation time (τ) is connected to the kinematic viscosity (ν) by $\nu = c_s^2(\tau - 1/2)\delta t$, where c_s is the lattice speed of sound. For a D2Q9 model (2-dimensional with 9 discrete velocities), the equilibrium distribution function (f_i^{eq}) is given as follows:

$$f_i^{eq} = \omega_i \rho \left[1 + \frac{3(\mathbf{e}_i \cdot \mathbf{u})}{c_s^2} + \frac{9(\mathbf{e}_i \cdot \mathbf{u})^2}{2c_s^4} - \frac{(\mathbf{u} \cdot \mathbf{u})}{c_s^2} \right], \quad (37)$$

where ω_i is a weight coefficient, \mathbf{u} is the velocity, and \mathbf{e}_i is the discrete velocity set, which is described by Qian et al. [138] for a D2Q9 model; $\Delta f_i(x, t)$ is the force term, which is given as

$$\Delta f_i(x, t) = \left(1 - \frac{1}{2\tau} \right) \omega_i \left(\frac{\mathbf{e}_i \cdot \mathbf{u}}{c_s^2} + \frac{\mathbf{e}_i \cdot \mathbf{u}}{c_s^4} \cdot \mathbf{e}_i \right) \cdot \mathbf{F} \Delta t, \quad (38)$$

Here, \mathbf{F} is the net force, which is the sum of the fluid–fluid interaction force, \mathbf{F}_f , the fluid–solid interaction force, \mathbf{F}_s , and the gravitational force, \mathbf{F}_g :

$$\mathbf{F}_f(x) = -G_f \psi(x) \sum_i \omega_i (|\mathbf{e}_i|^2) \psi(x + \mathbf{e}_i \Delta t) \cdot \mathbf{e}_i \quad (39)$$

$$\mathbf{F}_s(x) = -G_s \psi(x) \sum_i \omega_i (|\mathbf{e}_i|^2) \psi(x) s(x + \mathbf{e}_i \Delta t) \cdot \mathbf{e}_i, \quad (40)$$

$$\mathbf{F}_g = (\rho - \rho_{avg}) \mathbf{g}, \quad (41)$$

where G_f is the fluid–fluid interaction strength and is taken as -1 , and the fluid–solid interaction strength G_s can be adjusted based on the required contact angle. The function $s(x + \mathbf{e}_i \Delta t)$ is considered to be equal

to unity if $x + \mathbf{e}_i \Delta t$ is a solid node, otherwise, it is set to zero. For the D2Q9 setup, the weight coefficients are set to $\omega(1) = 1/3$ and $\omega(2) = 1/12$. The pseudo-potential Ψ is taken as $\Psi = \sqrt{2(p_{EOS} - \rho c_s^2)/Gc^2}$, where the pressure p_{EOS} is given by the Peng–Robinson equation of state:

$$p_{EOS} = \frac{\rho RT}{1 - b\rho} - \frac{a\varphi(T)\rho^2}{1 + 2b\rho - b^2\rho^2}, \quad (42)$$

with $\varphi(T) = [1 + (0.37464 + 1.54226z - 0.26992z^2)(1 - \sqrt{T/T_c})]^2$, $R = 1$, $a = 3/49$, $b = 2/21$, and $z = 0.344$.

The streaming step is defined as shown below:

$$f_i(x, t + \Delta t) = f_i^*(x - \mathbf{e}_i \Delta t, t). \quad (43)$$

The macroscopic density ρ and velocity \mathbf{u} can then be obtained by taking moments of the distribution function:

$$\rho = \sum_i f_i \rho \mathbf{u} = \sum_i f_i \mathbf{e}_i + \frac{\Delta t}{2} \mathbf{F}. \quad (44)$$

In the flow boiling heat transfer case, the flow field and the temperature should be coupled. Here, the coupling is accomplished by the equation of state, and the corresponding governing equation for the temperature writes as:

$$\rho c_v \left(\frac{\partial T}{\partial t} + \mathbf{u} \cdot \nabla T \right) = \nabla \cdot (k \nabla T) - T \left(\frac{\partial p_{EOS}}{\partial T} \right) \nabla \cdot \mathbf{u} \quad (45)$$

where c_v is the specific heat at constant volume. As reported by Hu and Liu (2019) [139], the accuracy and the numerical stability can be improved by considering the finite volume method for solving the energy equation. Wang et al. [140] used this approach to study flow boiling in microchannels with different confinement heights, wherein they noted early formation of slug flow pattern for channels with smaller confinement height.

2.4. Molecular dynamics simulations

Molecular Dynamics (MD) is also a particle-based discrete method but a more fundamental one as compared to LBM since it deals with the motion of each molecule. MD is capable of handling physics where the continuum assumption breaks down and therefore phenomena such as nucleation, phase change, boiling, surface tension arise naturally from a simulation without the need for any closure model other than that for the interatomic potential used for fluid–fluid and fluid–solid interactions.

In a MD simulation, the motion of each molecule is obtained by integrating in time Newton's second law of dynamics, $\mathbf{F}_i = m_i(d\mathbf{u}_i/dt)$ where m_i is the mass of the i^{th} molecule, \mathbf{u}_i its velocity and \mathbf{F}_i the net force acting on it resulting from nearby molecules. The force exerted on the i^{th} molecule by the generic j^{th} molecule is calculated from the gradient of the interatomic potential chosen, $\mathbf{F}_i = -\nabla U_{ij}$. The most widely used interatomic potential in MD simulations of boiling is the Lennard–Jones potential, which is assumed as a good approximation of that of Argon, and is expressed as:

$$U(r_{ij}) = 4\epsilon \left[\left(\frac{\sigma_p}{r_{ij}} \right)^{12} - \left(\frac{\sigma_p}{r_{ij}} \right)^6 \right] \quad r_{ij} < r_c, \quad (46)$$

where r_{ij} is the distance between molecules i and j , ϵ is the potential well depth, σ_p is the molecular diameter, and r_c the cutoff radius. For $r_{ij} > r_c$, the intermolecular potential is set to zero. The potential well depth is different for fluid–fluid and fluid–solid interactions, the ratio of which gives rise to different wetting conditions [141].

Owing to their computational cost, MD simulations of flow boiling in microchannels are not yet possible, and the only studies available in the literature, reviewed briefly here, are limited to channels of size below $1 \mu\text{m}$. Yan et al. [142] considered a microchannel of cross-section $0.5 \times 0.5 \mu\text{m}$ and length $1 \mu\text{m}$ to compare the flow boiling of argon inside smooth and rough surfaces of cubic shape. A similar study was also done by Rostami et al. [143]. Mosavi et al. [144] employed

similar geometry conditions but considered spherical geometry for roughness elements in their simulation. Liu et al. [145] considered a similar channel geometry but compared the effect of triangular, cubic, and circular ribs on the flow boiling of argon.

Although MD simulations of flow boiling in microchannels are not yet possible, MD can be a viable tool to understand some of the fundamentals of flow boiling in microchannels such as the impact of disjoining pressure on thin film evaporation [146], or to assess the validity of the Schrage equations for different fluids [147,148], the latter being the theory from which Eq. (13) for the estimation of phase change rates in CFD frameworks originates.

2.5. Nucleation models

The modelling of nucleation remains one of the main weaknesses in macroscale simulation methods, because the continuum Navier–Stokes equations do not incorporate the molecular interactions responsible for the generation of a vapour embryo. As such, bubbles are usually artificially seeded at prescribed nucleation points. For example, Georgoulas and Marengo [149] initially performed single-phase simulations. Once the hydrodynamics and thermal boundary layers were fully-developed, a bubble was manually seeded at a certain location at the conjugate heat transfer boundary. Vontas et al. [150] also followed a similar approach, but to create a more realistic flow pattern, they initiated multiple bubbles with multiple recurring nucleation events, wherein they inserted multiple bubbles after every 0.5 ms. El Mellas et al. [151] simulated flow boiling in a micro-pin evaporator and utilised the experimental data of Falsetti et al. [152] to set nucleation spots at corresponding locations, with the nucleation frequency extracted from the experimental dataset by means of an updated three-zone model [153]. Yazdani et al. [154] assigned a randomly generated roughness value to each grid point of the boiling surface. The temperature at these grid points was compared with the wall superheat necessary for the activation of the nucleation site. A bubble was then placed at the location where enough superheat was available, with the activation temperature calculated using the model provided by Faghri [155]. Sato and Niceno [156] followed a similar approach, but instead of assigning roughness values randomly, they distributed the location of nucleation sites using a random number generator. Chen et al. [157, 158] used the nucleation density site model developed from the experimental study by Li et al. [159], first calculating the active nucleation site density and then randomly placing these nucleation sites on the wall surface. Wherever the condition for the activation of nucleation was satisfied (i.e. at the location where local wall superheat exceeded the condition for nucleation site activation), an initial bubble of $50 \mu\text{m}$ was artificially placed at that location. Progress towards physically-based bubble nucleation was made recently by approaches coupling Phase Field with Fluctuating Hydrodynamics Theory [160,161], where spontaneous bubble nucleation emerged from the description of thermal fluctuations. Another promising approach is constituted by hybrid simulations coupling MD and macroscale methods. Gennari et al. [162] used a MD simulation of boiling over a heated surface to generate data to be used as time-dependent phase fraction, velocity, and temperature boundary conditions for a VOF simulation. As such, the wall in the VOF simulation was replaced with data from the MD, allowing nucleation and contact line dynamics to be handled exclusively by MD.

Nucleation in LBM happens by the natural evolution of the energy equation, and the phase change is determined by thermodynamic relation governed by the equation of state [140,163]. Hence there is no need to artificially initiate a bubble nucleus in the case of Lattice Boltzmann method.

Besides the difficulty of modelling the fundamental aspects of nucleation, this process also depends on the actual surface conditions of the microchannel, usually quantified as mean surface roughness and/or peak-to-valley distance, which depend on the evaporator material and manufacturing method [164]. For example, Mahmoud et al. [165]

studied flow boiling of R134a in two stainless steel microchannels of the same size but manufactured by two different methods, obtaining completely different boiling characteristics and magnitudes of the heat transfer coefficients. Very few experimental studies provide detailed data about the topography of boiling surfaces, however, this is now becoming an essential information to model bubble nucleation from first principles, and thus achieve bubble dynamics and heat transfer rates in agreement with experiments.

2.6. Validation of computational methods for boiling in microchannels

Verification and validation is an essential step in the assessment of numerical methods. For phase change algorithms aimed to model processes such as boiling, evaporation and condensation, there exist a number of test cases that have analytical solutions and can be used to test the accuracy of the numerical predictions. Benchmarking against these solutions should be the first stage of validation of any computational method designed to model boiling flows. Once this first check is passed, the validation effort should be dedicated to experimental validation, based on available experimental data at conditions representative of those being simulated. This section has been divided into two subsections discussing both the analytical solutions and experimental results available for the validation of computational methods.

2.6.1. Analytical solutions for validation

The first validation benchmark typically performed for phase-change algorithms is the one-dimensional Stefan problem, in which an analytical solution for the interfacial position and temperature is available for the case when heat is being transferred from the wall to the liquid through the vapour phase. A schematic of this case is shown in Fig. 8(a). In this case, the surface is maintained at a temperature greater than the saturation temperature due to which liquid evaporates leading to a motion of interface to the right. The heat in the vapour phase is transferred by conduction, hence the energy equation at the interface is given by:

$$\frac{\partial T}{\partial t} = K_v \frac{\partial^2 T}{\partial x^2}, \quad 0 \leq x \leq x_i(t), \quad (47)$$

where K_v is the vapour thermal diffusivity and $x_i(t)$ is the location of the interface at the time instant. The initial condition is assumed to be $x_i(t=0) = 0$. The problem is closed with the boundary conditions:

$$T(x=0, t) = T_w, \quad T(x=x_i(t), t) = T_{sat}, \quad (48)$$

and the interfacial energy jump condition:

$$\rho_v h_{lv} \mathbf{u}_i = K_v \frac{\partial T}{\partial x} \Big|_{x=x_i(t)}, \quad (49)$$

in which $\mathbf{u}_i(t)$ represents the velocity at the interface. The analytical solution for the interface location $x_i(t)$ and the temperature $T(x, t)$ is given by:

$$x_i(t) = 2\beta\sqrt{K_v t}, \quad (50)$$

$$T(x, t) = T_w + \frac{T_{sat} - T_w}{\operatorname{erf}(\beta)} \operatorname{erf}\left(\frac{x}{2\sqrt{K_v t}}\right), \quad (51)$$

where β is determined from:

$$\beta \exp(\beta^2) \operatorname{erf}(\beta) = \frac{c_{p,v}(T_w - T_{sat})}{\sqrt{\pi} h_{lv}}. \quad (52)$$

A detailed explanation of Stefan problem can be found in the literature [166–168].

Another typical benchmark case is the sucking interface problem. The case is similar to the Stefan problem, with the difference that liquid is now the superheated phase and the heat transfer from the liquid to the vapour is the driving mechanism for phase change. This is more challenging than the Stefan problem because a thin temperature

boundary layer forms on the liquid side of the interface and this must be accurately resolved to achieve mesh-independent results. A schematic of the sucking interface problem is shown in Fig. 8(b). The heat transfer in the liquid phase is governed by both conduction and convection in which the energy equation is given by:

$$\frac{\partial T}{\partial t} + (\mathbf{u}_l - \mathbf{u}_i) \frac{\partial T}{\partial \xi} = K_l \frac{\partial^2 T}{\partial \xi^2}, \quad 0 < \xi < \infty \quad (53)$$

where ξ is the transformed spatial coordinate, $\xi = x - \int_0^t u_i(t') dt'$ defined such that the interface is located at $\xi = 0$. The boundary and the initial conditions are

$$\left. \begin{aligned} T(\xi=0, t) &= T_{sat} \\ T(\xi \rightarrow \infty, t) &= T_\infty \end{aligned} \right\} \rightarrow \text{boundary conditions} \quad (54)$$

$$T(\xi, t=0) = T_\infty \rightarrow \text{initial condition}$$

At the interface, we have energy and mass jump conditions respectively given by:

$$\rho(\mathbf{u}_l - \mathbf{u}_i) h_{lv} = -k_l \frac{\partial T}{\partial \xi}, \quad (55)$$

$$-\rho_v \mathbf{u}_i = \rho_l(\mathbf{u}_l - \mathbf{u}_i). \quad (56)$$

Eq. (53) can be transformed into a non-linear ordinary differential equation using a similarity variable which can be solved numerically to provide a semi-analytical solution for the validation of boiling algorithms. Further description of the sucking interface problem can be found in the literature [166,169].

The third case is the reverse of the Stefan problem, where the position of the liquid and the vapour phases are exchanged (see Fig. 8c). Hence, this case resembles a situation in which a liquid film covers the heated wall and evaporates. The wall surface is maintained at a constant temperature higher than the saturation temperature, while the boundary condition at the interface for this case is given by:

$$h_e(T(x=x_i(t)) - T_{sat}) = k_l \frac{\partial T}{\partial x} \Big|_{x=x_i}. \quad (57)$$

Here, $h_e = \frac{2\gamma}{2-\gamma} \frac{h_{lv}^2}{\sqrt{2\pi R_{gas}}} \frac{\rho_v}{T_{sat}^{3/2}}$ is the evaporative heat transfer coefficient [84]. With the use of similarity variable $\zeta(x, t) = x\beta/x_i(t)$, the analytical solution for $T(x, t)$ and $x_i(t)$ in this case is given in terms of the imaginary error function [111]:

$$T(x, t) = T_{wall} - \Delta T_w \frac{\operatorname{erfi}(\zeta)}{\operatorname{erfi}(\beta)}, \quad (58)$$

$$x_i(t) = 2\beta\sqrt{K_l(t_0 - t)}, \quad (59)$$

where K_l is the thermal diffusivity of liquid and β has already been defined in connection with Eq. (52).

The fourth case involves the heat-transfer-controlled growth of a spherical bubble in an infinite pool of superheated liquid for which analytical expressions for liquid temperature over time and distance from the interface, and law for bubble radius over time $R_b(t)$, were provided by Scriven [170]:

$$R_b(t) = 2\beta_1\sqrt{K_l t}, \quad (60)$$

where $\beta_1 = Ja\sqrt{3/\pi}$, $Ja = \frac{(T_\infty - T_{sat})\rho_l c_{p,l}}{\rho_v h_{lv}}$ is the Jakob number, and T_∞ is the far-field liquid temperature value.

2.6.2. Experimental data for validation

Besides the verification of the numerical models using analytical solutions, observations from the simulations should also be validated with available experimental results. In the case of pool boiling, advanced data processing techniques such as laser interferometry and total reflection techniques [171–173] have been used to understand the microlayer geometry and the distribution of liquid–vapour phase on the boiling surface, respectively, because of which high-resolution space and time measurement data of microlayer formation is available. MEMS

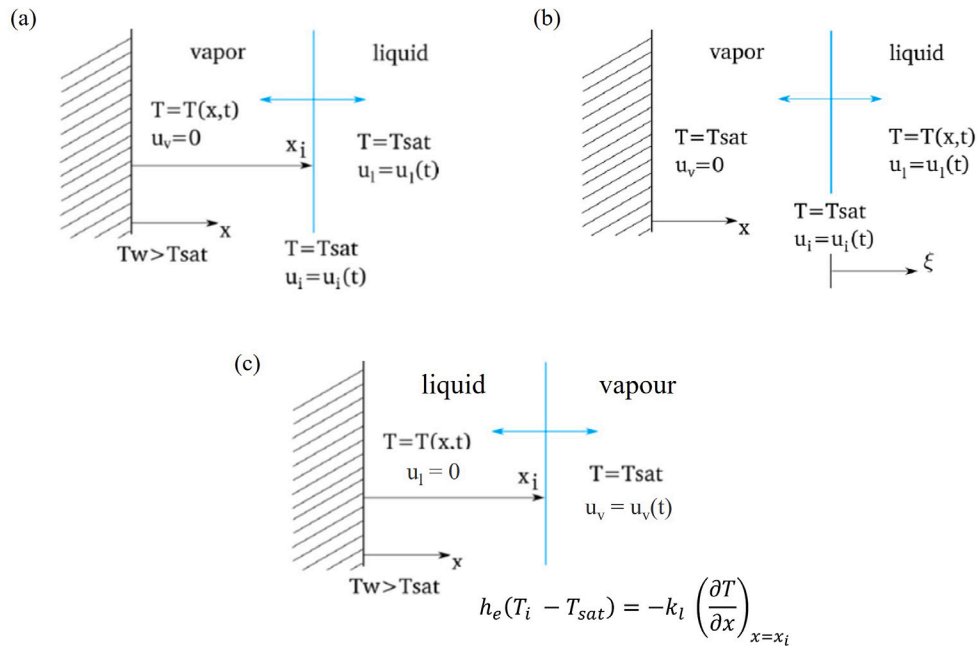


Fig. 8. Schematics showing the (a) Stefan problem, (b) sucking interface problem and (c) second Stefan problem in which the location of liquid and vapour phases are exchanged with liquid covering the wall.

sensors [174,175] and Infrared thermography techniques [173,176] have been used to acquire data on the heat transfer characteristics of the surface and local temperature during boiling. For example, Bureš and Sato [177] and Municchi et al. [178] have used the experimental data of Bucci [179], where individual isolated steam bubbles were produced in a well-controlled environment, to validate their numerical models. Moreover, even the liquid temperature distributions around the growing bubble have been measured using techniques such as rainbow Schlieren deflectometry [180] and laser-induced fluorescence [181].

The validation of numerical simulations against experimental data for flow boiling in microchannels is very challenging owing to the limited availability of spatio-temporally resolved experimental data and intrinsic limitations of the numerical methods. Multi-microchannel evaporators are usually employed in the practice. These are characterised by nonuniform heating and nonuniform flow distribution, making it difficult to set corresponding boundary conditions in simulations of one single channel or only a subset of channels. Nucleation in microchannels results in the chaotic generation of bubbles which have a distinctive signature on heat transfer, however, nucleation can only be artificially prescribed in macroscale simulation models; for the purpose of validation, it would be useful to have experimental data where isolated bubbles are generated as already done in pool boiling [179]. Experimental measurements are usually taken at steady-state, i.e. when temperature and pressure measurements have reached constant values over time, however, numerical simulations cannot really achieve steady-state conditions unless run for a very long time [23], which is too computationally expensive in 3-D. El Mellas et al. [151] have recently proposed a way forward to circumvent this problem, by extracting an initial temperature condition for the simulation from benchmark experimental data taken at steady-state [197], thus enabling the simulation to achieve a steady-state only after a few bubble nucleation cycles. Temperature and pressure measurements in experiments are not taken directly within the microchannels, e.g. temperature sensors are usually embedded in the solid block housing the evaporator and pressure sensors are installed in the inlet and outlet manifolds. The friction factor and heat transfer coefficient within the channel are then calculated according to data reduction procedures relying on a number of assumptions and correlations (e.g. to estimate the pressure drop across the many inlet and outlet restrictions and

expansions), which can significantly influence the final values [28] and prevent a coherent comparison with simulations. The geometrical features of the solid parts of the test section have a very influential impact on the heat distribution to the fluid [198] and the traditional constant temperature or constant heat flux boundary conditions applied to the fluid channel may not be representative. Finally, microchannels are usually subject to high-pressure drop and the saturation temperature may vary significantly along the channel [28]. Numerical simulations typically assume that the saturation temperature is constant and do not account for this effect, which could potentially be easily implemented by making the saturation temperature, appearing in the interfacial mass flux equations presented in Section 2.1.4, variable as a function of pressure via the Clausius–Clapeyron equation.

Nonetheless, successful comparison of flow boiling simulations with experiments have been documented; Table 1 provides a summary of experimental studies that have been used for validation of numerical simulations. Most of the researchers validate their numerical models with the single-channel experimental data provided by Mukherjee et al. [118] who conducted experiments of flow boiling of water inside a single rectangular microchannel of hydraulic diameter of 229 μm . They reported data for bubble volume over time that have been used by several authors to validate their numerical simulations [199]. Bhuvankar and Dabiri [187] used experimental data of bubble nucleation frequency and wall superheat necessary for bubble nucleation reported by Yoo et al. [186] as the initial condition. Yoo et al. [186] conducted experiments of flow boiling of HFE-301 in a square channel of side 10 mm. However, the maximum diameter of the bubbles they observed was in the range of 1 mm, hence, Bhuvankar and Dabiri [187] performed simulations by considering a square channel of 2 mm size and successfully validated the bubble contours obtained from their simulations with the experiments. Dong et al. [182] used the experimental observations of bubble growth inside microchannels provided by Xu et al. [183] for validating their numerical model; the comparison is shown in Fig. 9(a). Xu et al. [183] conducted experiments of flow boiling of methanol liquid inside a microchannel of width 200 μm and depth of 40 μm . In their experiments, homogeneous nucleation was ensured by having a perfectly smooth microchannel which was fabricated using MEMS technology (roughness in the order of 2 to 200 nm), pure degassed liquid and high flow rates while the bubble formation

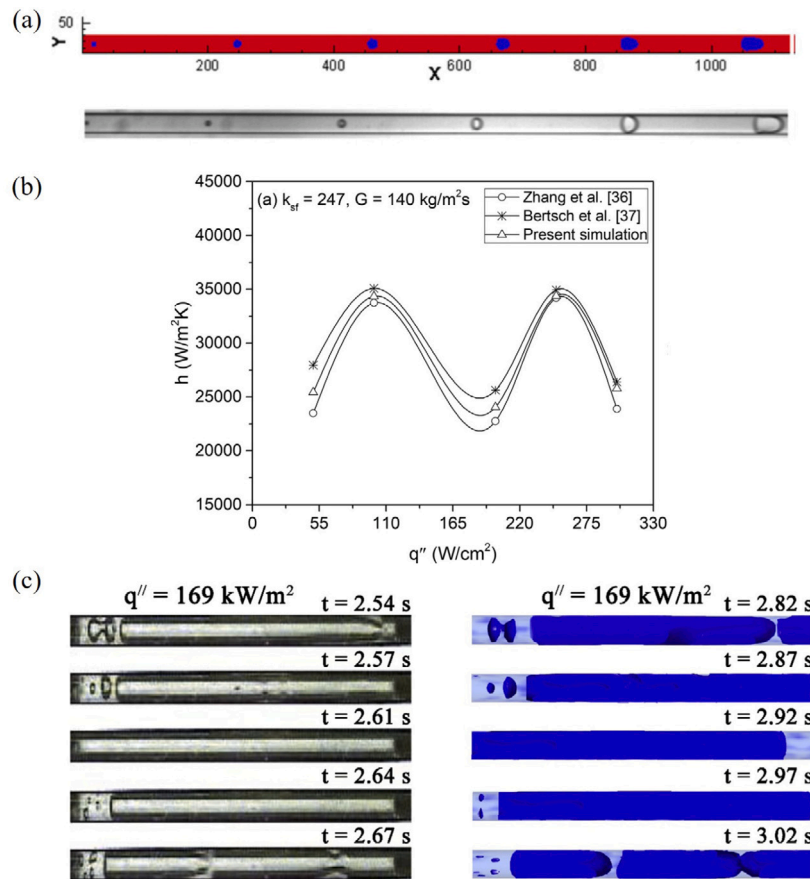


Fig. 9. (a) Comparison of simulation results of Dong et al. [182] (top figure) with the experimental observation of bubble growth inside a microchannel provided by Xu et al. [183] (bottom figure). (b) Comparison of heat transfer results obtained from the simulations performed by Tiwari and Moharana [184] with the available heat transfer correlations. (c) Flow pattern observed during flow boiling experiments [185] (left) and the corresponding simulations performed by Tiwari and Moharana [184] (right).

was controlled by regulating the voltage applied on the microheater ensuring single bubble generation for each bubble cycle. Hence these experimental results are also ideal for validating the predictions of numerical models involving confined bubble flow.

A number of researchers employed the Lee model for phase change where, although not physical, nucleation can occur in liquid-filled cells whose temperature is above saturation, thus enabling them to simulate the development of flow patterns and compare transient heat transfer coefficients with experimental results or correlations. Zhuan and Wang [189] performed 2D simulations of flow boiling of R134a inside a microchannel of height 0.5 mm and length 70.7 mm and reported a good agreement between their simulations and the experimental observations from Revellin et al. [188]. Tiwari and Moharana [184] compared the heat transfer coefficients from their 3D flow boiling simulation of water inside a microtube of diameter 0.6 mm with the correlation provided by Zhang et al. [192] and Bertsch et al. [193]. In this study, the conjugate heat transfer effect was also included. They reported a good agreement between the simulation results and the correlation results with a maximum deviation of up to 8.9% as shown in Fig. 9(b). Furthermore, Tiwari and Moharana [184] were also able to validate the flow pattern observations from their simulations with the experimental results of Huang et al. [185] who had performed experiments on flow boiling of water inside a microtube of diameter 1 mm (as shown in Fig. 9(c)). Broughton and Joshi [191] compared the heat transfer coefficient obtained from their simulation with the correlation provided by Kim and Mudawar [190] and reported a good agreement between the simulation and the predicted heat transfer coefficients (error of only 6%). Yeo and Lee [196] performed 2D simulations of flow boiling of R134a inside a microchannel of height 1 mm and length 609.6 mm

and compared the heat transfer coefficient results obtained from their simulation with in-house experimental results. They reported that CFD simulations could predict the saturated flow boiling heat transfer with a Mean Absolute Error (MAE) of $\pm 17.61\%$, however, the CFD simulations under-predicted the heat transfer coefficient for both subcooled and dryout regions leading to higher MAE (up to 35%). The critical heat flux results from the experimental work of Qu and Mudawar [200] have also been used to validate numerical studies [201,202].

Other useful datasets for flow boiling in microchannels exist, although these have not yet been utilised to validate simulations. For example, Rao and Peles [203] acquired high-resolution space and time measurements of local wall temperature during their experiment on flow boiling of HFE-7000 inside a single microchannel of hydraulic diameter of $370\ \mu\text{m}$. The temporal variation in wall temperature as the bubble moves forward from their observations is shown in Fig. 10(a). A decrease in wall temperature as the bubbles pass over the temperature sensor (region 1 in the temperature plot) and the subsequent increase in wall temperature as the bubble moves away from the sensor (region 2 in the temperature plot) can be observed from the figure, emphasising that the heat transfer is higher during the transit of the bubble. They have also provided a 1-D model for local changes in heat transfer which can be used for validation. Kingston et al. [204] adopted an interesting experimental setup to produce a well-organised slug flow using HFE-7100 in a microtube of diameter $500\ \mu\text{m}$. Saturated liquid and vapour phases were extracted separately from a fluid reservoir and combined using a T-junction upstream of the test section. This allowed to create a controlled slug flow of known bubble, liquid slug length and frequency at the inlet of a transparent microchannel, heated by a transparent ITO layer. Although the authors did not perform temperature

Table 1

Summary of experimental results used for validation of numerical simulations of flow boiling in microchannels.

Experimental observations	Numerical studies
Validation with bubble growth or flow pattern from experiments	
Mukherjee et al. [118]: Experiment on bubble growth during flow boiling of water ($T_{\text{sat}} = 100 \text{ }^\circ\text{C}$ at 101.3 kPa) in a channel of depth 266 μm and width 201 μm .	These experimental results are widely used for validating the numerical model especially to validate the simulations with single bubble growth inside microchannels.
Yoo et al. [186]: Experiments on flow boiling of HFE-301 ($T_{\text{sat}} = 34 \text{ }^\circ\text{C}$ at 1 atm) in a square channel of side 10 mm.	Bhuvankar and Dabiri [187] successfully validated the bubble contours obtained from their simulation with this experiment. However, the channel size they had considered for the simulation is 2 mm since in the experiments the diameter of the bubbles was observed to be in the range of 1 mm. Fluid used was HFE-301 ($T_{\text{sat}} = 34 \text{ }^\circ\text{C}$ at 1 atm).
Xu et al. [183]: Experiments of flow boiling of methanol liquid ($T_{\text{sat}} = 64.7 \text{ }^\circ\text{C}$ at 101.3 kPa) in a microchannel of width 200 μm and depth of 40 μm .	Used by Dong et al. [182] for validating their numerical model involving LBM at $T_{\text{sat}} = 64.7 \text{ }^\circ\text{C}$.
Revellin et al. [188]: Provided flow pattern maps during flow boiling of R134a ($T_{\text{sat}} = 30 \text{ }^\circ\text{C}$ at 7.7 bar) in tubes of diameter 509 μm and 790 μm .	Zhuan and Wang [189] verified the flow patterns observed from their 2D simulations with tube of diameter 0.5 mm. R134a was used at $T_{\text{sat}} = 30 \text{ }^\circ\text{C}$, and the phase change model was that of Lee.
Huang et al. [185]: Experiments on flow boiling of water in a microtube of diameter 1 mm.	Tiwari and Moharana [184] validated the flow pattern observations from their simulations. The Lee model was used for phase change, and the relaxation factor was approximately equal to unity.
Validation with heat transfer correlations or heat transfer calculations from their own experiments	
Kim and Mudawar [190] universal correlation.	Broughton and Joshi [191]: 3D simulations of flow boiling of water ($T_{\text{sat}} = 100 \text{ }^\circ\text{C}$). Compared heat transfer coefficient with this correlation and observed a deviation of only about 6%. The Lee model was used for phase change, and the relaxation factor was approximately equal to 75.
Zhang et al. [192] used channels with hydraulic diameters of 0.78–6.00 mm and the test fluids were Water, R11, R12, and R113. The range of system pressures was 0.101–1.21 MPa.	Tiwari and Moharana [184]: 3D simulations of flow boiling of water ($T_{\text{sat}} = 310 \text{ K}$ at 6500 Pa) in a microtube of diameter 0.6 mm. They were able to compare heat transfer coefficients with this correlation and observed a maximum deviation of up to 8.9%.
Bertsch et al. [193] used channels with hydraulic diameters of 0.16–2.92 mm, 12 different working fluids, with a saturation temperature range of -194 to 97°C .	Tiwari and Moharana [184] and Tiwari and Moharana [194]: 3D simulations of flow boiling of water inside a microchannel of width 1.8 mm and height 0.9 mm. Alugoju et al. [195]: 3D simulations of flow boiling of water inside a microchannel of width 0.2 mm and height 0.4 mm. Obtained heat transfer coefficient results with a maximum deviation of 10.5% using the Lee model for phase change, and a relaxation factor of approximately unity.
Yeo and Lee [196]: Experiments with a channel of cross section 1 mm \times 1 mm and length 609.6 mm, and R134a ($T_{\text{sat}} = 26.35 \text{ }^\circ\text{C}$).	Yeo and Lee [196] compared the heat transfer coefficient results obtained from their 2D simulations with their experimental results and reported that CFD simulations can predict the saturated flow boiling heat transfer with a Mean Absolute Error (MAE) of $\pm 17.61\%$ using the Lee model for phase change and a relaxation factor of approximately 500.

measurements, the high-speed video images of the growing bubbles, depicted in Fig. 10(b), can be potentially used for numerical validation. Korniliou et al. [205] combined infrared temperature measurements with high-speed visualisation to study the flow boiling of FC-72 in a rectangular microchannel of cross-section $2.26 \times 0.1 \text{ mm}^2$. They provided time-resolved two-dimensional maps of wall temperatures and heat transfer coefficients alongside the observed liquid-vapour interface patterns from the camera images, see Fig. 11(a), which can be valuable for the validation of numerical simulations. Zhang et al. [206] performed measurements of transient liquid film thickness during flow boiling of ethanol inside a microchannel of hydraulic diameter of 700 μm with a mass flux of $26 \text{ kg}/(\text{m}^2\text{s})$ and heat flux in the range of $10\text{--}80 \text{ kW}/\text{m}^2$. Fig. 11(b) shows the transient liquid film thickness variation during flow boiling in a microchannel from their study. As the bubble passes through the measurement point, initially a sudden decrease in film thickness is observed (transition region in Fig. 11(b)) representing the transition between the bubble nose and microfilm region. Afterwards, the liquid film thickness reduced slowly (microfilm region in Fig. 11(b)) which happens due to evaporation, shearing, and transversal flow. They have also provided a model for predicting the liquid film thickness using the data obtained from their experiments, which can be used for validation.

Finally, several heat transfer correlations for boiling heat transfer in microchannels exist, which have been derived from experimental data, and these can potentially be utilised for the validation of numerical methods. A summary is provided in Table 2. A comprehensive review of databases and correlations for flow boiling heat transfer can be found in Kim and Mudawar [190].

2.7. Boiling simulation software and computational cost

Both ANSYS and COMSOL have been successfully used to simulate flow boiling in microchannels by implementing user-defined routines to improve the built-in models [22,112]. However, these improved versions of commercial software are not publicly available. Open-source software has been increasingly used over the last few years thanks to the open-source toolbox OpenFOAM. Nabil and Rattner [209] were the first to publicly release in Github interThermalPhaseChangeFoam, a full library to simulate boiling using a VOF method in OpenFOAM. Another self-developed VOF-based solver, phaseChangeHeatFoam, was released shortly afterwards by Samkhaniani and Ansari [210]. Recently, Muncichi et al. [178] released boilingFOAM, a VOF-based boiling solver based on OpenFOAM v2106 that incorporates conjugate heat transfer alongside strategies to improve surface tension. boilingFOAM was specifically developed for flow boiling in microchannels and validated using

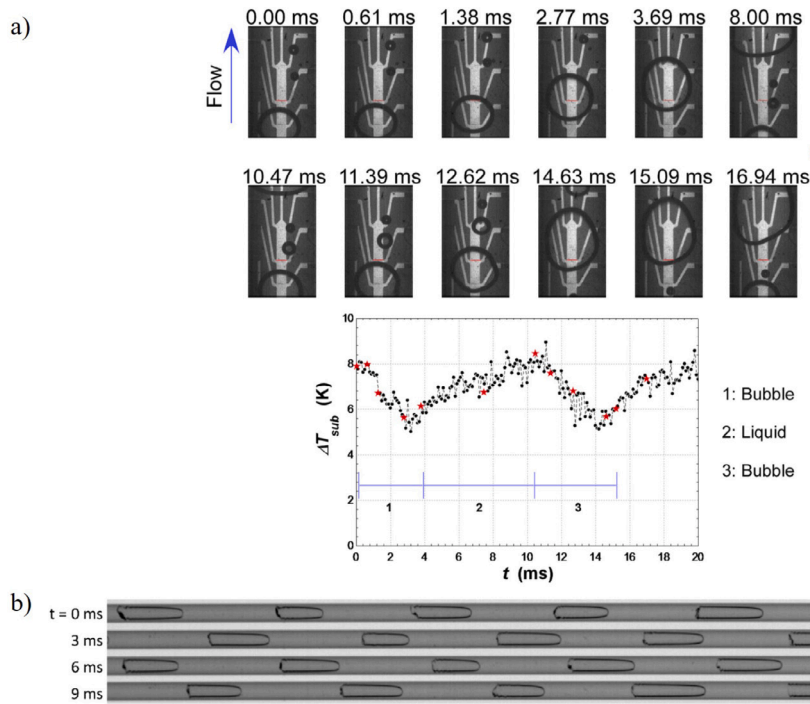


Fig. 10. (a) High-speed images and associated time-dependent temperature measurement during flow boiling of HFE-7000 in a microchannel [203]. (b) Well-controlled slug flow generated in the experimental setup of Kingston et al. [204].

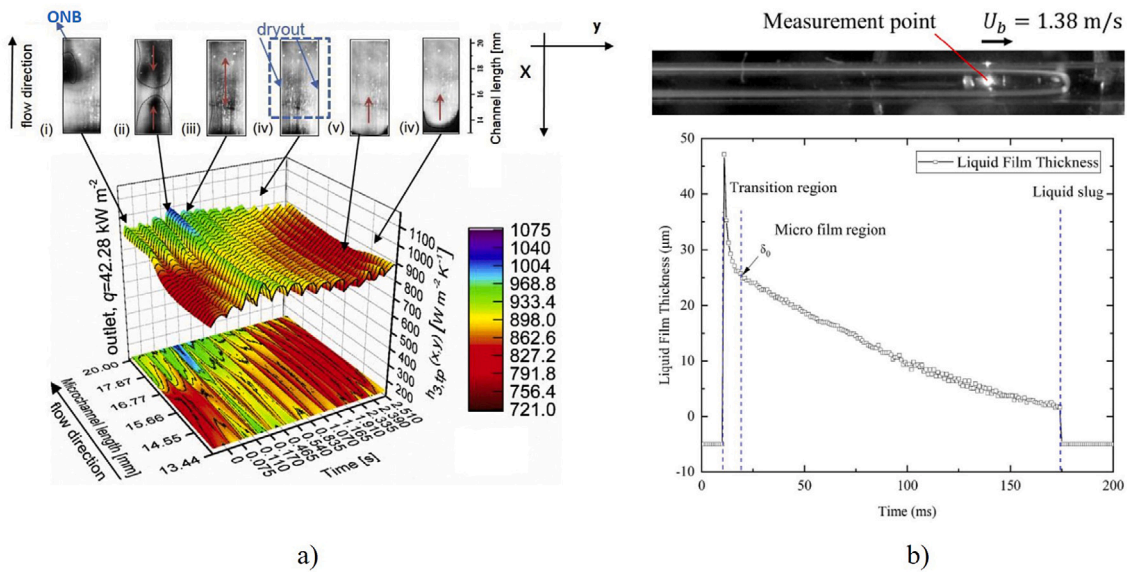


Fig. 11. (a) 2-D space-time dependent map of heat transfer coefficient and corresponding flow patterns observed by Korniliou et al. [205] during flow boiling of FC-72 in a flattened microchannel. (b) Transient liquid film thickness variation measured by Zhang et al. [206] around an elongated bubble during flow boiling in a microchannel.

experimental data from the literature. The most complete OpenFOAM library for two-phase flows with phase change is the TwoPhaseFlow library released by Scheufler and Roenby [211] for OpenFOAM v1812 and v2106. The library is based on the compressible VOF formulation of OpenFOAM, includes conjugate heat transfer, and routines to calculate phase change rates using either single-side heat fluxes via Eq. (11) or using the model of Tanasawa, Eq. (13), and to calculate surface tension based on a selection of highly accurate geometrical interface reconstruction schemes. Malan et al. [50] utilised the free code Parallel Robust Interface Simulator (PARIS), which combines VOF and FT methods for macroscale simulations of interfacial flows, and developed

new methods to implement phase change and handle the resulting velocity jump at the interface, validating the solver with a series of benchmark cases. Another in-house code publicly available in Github for two-phase boiling simulations is PSI-BOIL (Parallel Simulator of BOILING phenomena), developed at Paul Scherrer Institute. The code is based on a VOF method, it implements a number of libraries to model microlayer evaporation, turbulent flows, conjugate heat transfer, and it has been extensively used to simulate pool and flow boiling in various configurations [65,105,212–214].

The computational cost of simulations of flow boiling in microchannels is typically high, owing to the need to discretise the thin liquid

Table 2

Summary of heat transfer correlations proposed to predict flow boiling inside microchannels that could be employed for validation of numerical methods.

Reference	Correlation	Applicability range
Li and Wu [207]	$h_{ip} = [334 Bo^{0.3} (Bd Re_f^{0.36})^{0.4}] \frac{k_l}{D_h}$	More than 3744 data from 18 different sources
Mahmoud and Karayiannis [208]	For $D = 4.26 - 1.1$ mm and for $D = 0.52$ mm, $x_c \leq 0.3$ $h_{ip} = 3320 \frac{Bo^{0.63} W_f^{0.2} Re_f^{0.11}}{C_{\phi}^{0.6}} \frac{k_l}{D}$ For $D = 0.52$ mm, $x_c \leq 0.3$ $h_{ip} = 5324 \left[\frac{Bo^{0.3} W_f^{0.23}}{N_{c\phi}^{0.23}} \right] \frac{k_l}{D}$	For hydraulic diameter ranging from 4.26 to 0.52 mm
Kim and Mudawar [190]	$h_{ip} = (h_{nb}^2 + h_{cb}^2)^{0.5}$ $h_{nb} = \left[2345 \left(Bo \frac{P_{HT}}{P_{FT}} \right)^{0.70} P_r^{0.38} (1 - x_c)^{-0.51} \right] \left(\frac{0.023 Re_f^{0.8} Pr_l^{0.4} k_l}{D_h} \right)$ $h_{cb} = \left[5.2 \left(Bo \frac{P_{HT}}{P_{FT}} \right)^{0.08} We_{Lo}^{-0.54} + 3.5 \left(\frac{1}{X_{tt}} \right)^{0.94} \left(\frac{\rho_v}{\rho_l} \right)^{0.25} \right] \left(\frac{0.023 Re_f^{0.8} Pr_l^{0.4} k_l}{D_h} \right)$	10805 pre-dryout points from 31 sources. Hydraulic diameters ranging from 0.19 mm to 6.5 mm. 18 different working fluids.

films trapped between bubbles and walls, and the thin thermal boundary layers around liquid-vapour interfaces. For example, the evaporation microlayer trapped beneath steam bubbles at atmospheric pressure during their unconfined growth stage has thickness on the order of 1 μm , thus requiring cells of thickness of 0.5 μm or below, unless a subgrid film model is used. When the bubble growth becomes confined, Bretherton's law [92] can be used to estimate the film thickness for elongated bubbles whereas the models of Harirchian and Garimella [215] and Cioncolini and Thome [216] can be used for annular flow. In typical conditions, these thicknesses are often on the order of 1/50 of the channel diameter, thus requiring mesh sizes on the order of the micrometre to adequately capture the film dynamics and heat transfer in channels of $D_h \approx 100 \mu\text{m}$. Hence, a rough estimate suggests that about 1 million cubic cells are required to discretise a channel of length D_h , with 20 million cells required to model a channel of length $20D_h$, necessary to observe some flow pattern development [178,217]. Time-steps are typically on the order of $10^{-8} - 10^{-7}$ s to ensure Courant numbers well below unity, and thus $10^4 - 10^5$ time-steps are required to achieve 1 ms of simulation time, still too small to attain steady-state conditions but sufficient for a fundamental analysis of the boiling dynamics.

These aforementioned simulations must run on high-performance computers; their computational cost depends on the hardware available and their overall duration depends on the number of cores used. For example, Mucicchi et al. [199] used OpenFOAM to model the flow boiling of water at atmospheric pressure in a $D_h = 229 \mu\text{m}$ channel of the length of $20D_h$, using a symmetric boundary condition to halve the domain width, employing about 3 million cells. Simulations were run on the UK Tier-1 national supercomputer ARCHER2, which features computing nodes with two AMD EPYC 7742 2.25 GHz 64-core processors, thus making 128 cores and 256 GB of RAM per node. A representative simulation required 2 days on 2 computing nodes to achieve an elapsed time of about 1 ms, which makes about 12,000 CPU hours. Hence, roughly 4000 CPU hours were required for each million of cells to complete a simulation. Similarly, Andredaki et al. [217] simulated flow boiling in microchannels in domains composed of about 13 million cells, and reported an average of 60,000 CPU hours necessary to complete each simulation, providing an estimate of 4600 CPU hours for every one million cells.

2.8. Summary and challenges

Various numerical methods available for phase change simulation ranging from macro to molecular scale have been discussed in the preceding sections. The interface-resolving methods such as level-set

method and VOF have been widely used for simulating multiphase flows involving phase change. Though attempts have also been made to improve these methods either by adopting reinitialisation techniques to reduce mass loss error in the case of level-set method or by adopting the height function method to reduce spurious currents in the case of the VOF method, there is still room for betterment to accurately capture interface topologies in complex phase change scenarios. Care should be taken to avoid spurious currents since these can be especially detrimental for flows in microscale channels. Diffuse interface numerical techniques such as the phase field method, although conservation of mass is not as accurate as VOF, can still capture essential physics at the interface with a lesser magnitude of spurious currents. Hence, the focus should be given to further improving these models in the future to capture interfacial physics accurately. Moreover, there is a higher computational cost associated with most of these methods owing to the need for having uniform square meshes to suppress the generation of spurious currents to the greatest extent. Pan et al. [218] demonstrated a method which allows the use of non-uniform meshes. They demonstrated that spurious currents can be reduced by employing an artificial moving reference frame to increase the local velocity near the interface.

Further, the phase change models utilised with the interface resolving techniques have been discussed. The major challenge with both Lee model and Schrage model for phase change is in deciding the value of the empirical coefficients. The phase change model based on the energy jump condition is free from empiricism, but it does not account for kinetic energy contributions. Further, with the Schrage model and model based on energy jump condition, phase change can only happen along the two-phase interface, which requires artificial initiation of the bubble nucleus. Therefore, there is a need to develop improved phase change models addressing the issues present in the existing ones to accurately calculate mass and energy transfer at the interface.

Meso-scale methods such as the LBM have become popular recently for simulating boiling flows in microchannel owing to their advantages such as the ability to capture the interfacial behaviour even without any interface-tracking algorithms, and to achieve bubble nucleation without any initial artificial assignment of bubbles. However, most of the research on flow boiling inside microchannels using LBM available in the literature employed 2-D simulations since they are computationally cheaper. Though such simulations have been used to predict boiling curves successfully, they cannot appropriately predict the dry patches at the wall or critical heat flux [219,220]. Hence, there is a necessity to extend and check the adaptability of existing LBM in a 3-D domain. Further, fundamental discrete particle-based approaches such as MD simulations are capable of simulating micro-scale phenomena such as

bubble nucleation, at which scale the continuum assumption breaks down. These MD simulations, however, are computationally costly for simulating at a micro-scale level and hence have been mainly employed for studying boiling in nanochannels so far. However, molecular dynamics have been used in conjunction with CFD to model nucleation in the pool boiling case which can be looked into in the future for the flow boiling case.

A discussion has also been provided of the experimental studies involving flow boiling in microchannels available for validation of the numerical methods. A large number of experiments and correlations are available to validate numerical codes. However, there is still limited availability of finely resolved spatio-temporal data for bubble dynamics, evaporating liquid film thickness, and local heat transfer measurements, which are on the other hand becoming available for pool boiling. Significant algorithmic steps forward are also necessary for numerical methods, in particular, to approach experimental time scales where data are taken at steady-state conditions, which are difficult to achieve in numerical simulations due to their computational cost.

Furthermore, conventional CFD methods have a high computational cost since they require a fine uniform mesh to capture the small scales and gradients, such as the liquid-vapour interface. Interface-tracking adaptive mesh refinement models, which dynamically refine the mesh only in the regions of interest and allow a coarser mesh in the rest of the domain, might help in reducing the computational cost. Potgieter et al. [221] had proposed an interface-tracking adaptive model to simulate slug flow inside microchannels and they claimed that using adaptive mesh refinement can reduce the number of cells by 25 to 60 times compared to static meshes. They were able to predict the interface profile during slug flow boiling with a maximum error of 6.7% by using the adaptive mesh refinement method. However, further study is necessary in future to establish this as a reliable method and the adaptability of such methods should also be tested for complex flow phenomena, such as interactions between multiple bubbles. Moreover, though dynamic adjustment of meshes can reduce the number of computational cells, they can still significantly increase computational complexity and processing time, particularly in capturing rapid phase changes and interface movements and it is also quite challenging to ensure numerical stability and accuracy during mesh refinement transitions.

3. Fundamental analyses of microchannel flow boiling

In this section, we review the computational studies of flow boiling in microchannels that aimed at elucidating essential aspects of bubble dynamics, two-phase fluid mechanics, and heat transfer processes. Section 3.1 discusses analyses devoted to different flow patterns inside microchannels and associated heat transfer characteristics. Conjugate heat transfer studies are tackled in Section 3.2, while Section 3.3 reports results of multi-microchannel investigations.

3.1. Flow patterns during flow boiling inside microchannels

Fig. 12 shows experimental snapshots of two-phase flow patterns visualised inside tubes of different diameters, i.e. a 100 μm , a 1.1 mm and a 2.2 mm diameter tube. From these images, the flow patterns inside small diameter tubes can be broadly classified into three types of flows in general: (i) Dispersed bubbly flow, which is defined by bubbles of size smaller than the tube diameter, dispersed in the liquid phase; (ii) Annular flow, characterised by a gas core surrounded by a thin liquid film near the wall, and (iii) Intermittent flows which include slug, elongated bubbles or churn flow. Very few studies attempted to simulate all flow patterns in one single simulation because that would require a very long domain with a significant computational effort. Furthermore, different flow patterns have different mesh requirements, for example, bubbly flows require a fine mesh only around the isolated

bubbles, whereas slug and annular flows require very fine meshes to capture the thin liquid films. Hence, most of the numerical studies in the literature have focused on specific flow patterns. Accordingly, this section is organised in three subsections. In Section 3.1.1, we review the computational studies that focused on single, isolated bubbles, from their inception until they become elongated in the direction of the flow. Section 3.1.2 is focused on the interaction between multiple bubbles, including bubble coalescence which eventually leads to annular flow. Most of the numerical studies for flow boiling in microchannels modelled bubbly and slug flows, and thus the results for these flow regimes are discussed in detail. Slug to annular flow pattern transitions and annular flows have received less attention and the available studies are reviewed in Section 3.1.3.

3.1.1. Confined bubble and elongated bubble flow

Mukherjee and Kandlikar [225] were among the first to numerically study the dynamics of a single bubble inside a microchannel, using a level set method. The single bubble case was considered since in the experiments of boiling inside a microchannel, a bubble nucleating at the wall is observed to grow large enough rapidly to cover the entire channel [226]. In their simulation, they considered a channel of hydraulic diameter 198 μm with water as the fluid at the inlet having a velocity of 0.146 m/s, and the wall surface was maintained at a constant surface temperature of 107 $^{\circ}\text{C}$. They observed that the bubble undergoes sudden expansion and touches the wall and a thin layer of liquid is trapped between the superheated wall and the saturated vapour wherein a high rate of evaporation exists.

The sudden expansion of the bubble inside the channel is unique to microchannels because of the confined space. This difference in the dynamic growth of the bubble in channels of various sizes was shown by Lee and Son [227] using the level set method with modifications to include a model to predict the evaporative heat flux from the microlayer. Square channels of hydraulic diameter 3 mm, 0.8 mm, and 0.4 mm were considered in their study with saturated water at 1 atm at a velocity of 0.12 m/s as fluid at the inlet. The wall temperature was maintained at 105 $^{\circ}\text{C}$. They observed that, in the case of narrow channels ($D_h = 0.4$ mm), the nucleating bubble grew to occupy the entire cross-section and then expanded along the channel developing into a slug. In contrast, in the case of bigger channels ($D_h = 3$ mm), the bubble initially travelled along the wall but detached from the surface as buoyancy force became dominant. They also reported a rapid increase in wall heat flux in the case of narrow channels ($D_h = 0.4$ mm) as compared to the channels of bigger size owing to the slug formation and the existence of a thin liquid layer between the channel corner and bubble. Hence, it can be said that the evaporation in this thin liquid layer controls the bubble growth in microchannels. The same authors also studied the effect of variation in contact angle on thin film dynamics inside the microchannel. They considered different contact angles within the range of 30 $^{\circ}$ –50 $^{\circ}$ in their study and observed that the thickness of the liquid layer between the bubble and the channel corner decreased with an increase in contact angle. Based on their simulations with different contact angles, they suggested that a contact angle less than 45 $^{\circ}$ is better for narrow channels (or microchannels) since the liquid layer between the bubble and the channel corner might cease to exist for contact angles greater than 45 $^{\circ}$, resulting in a decrease in heat transfer. The effect of contact angle on bubble dynamics was also studied by Mukherjee [228] but by considering different advancing and receding contact angles instead of static contact angles. The channel geometry, fluid properties, and boundary conditions were the same as those considered in Mukherjee and Kandlikar [225]. The receding contact angles used were 20 $^{\circ}$, 40 $^{\circ}$, and 60 $^{\circ}$, whereas the advancing contact angle considered were 40 $^{\circ}$, 60 $^{\circ}$, and 80 $^{\circ}$. They observed a decrease in bubble growth rate when the advancing contact angle is increased keeping the receding contact angle at 20 $^{\circ}$. In contrast, the bubble growth rate improved when the receding contact angle was increased keeping a constant advancing contact angle of 80 $^{\circ}$, owing to

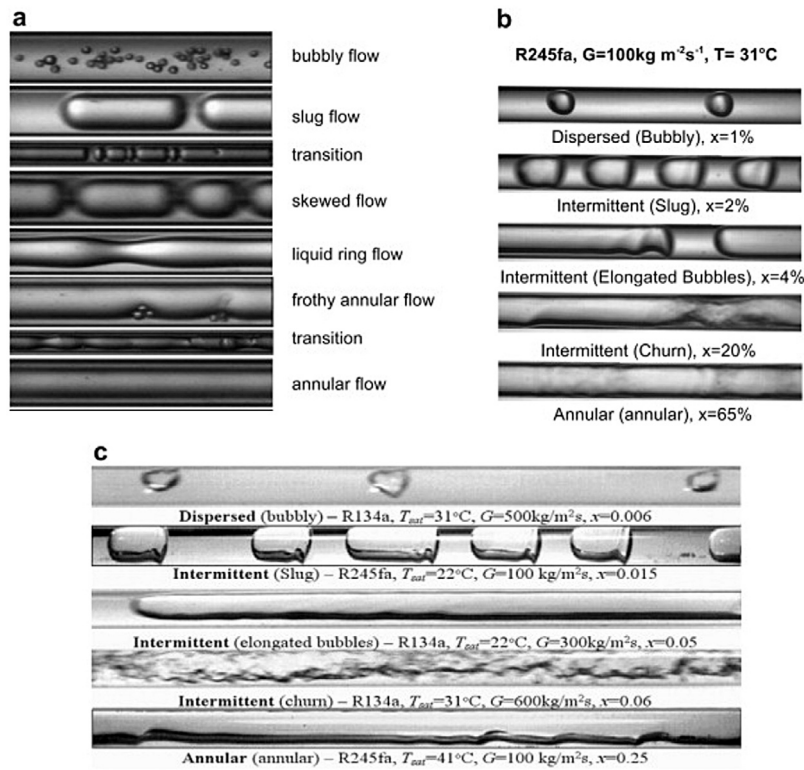


Fig. 12. (a) Air–water two-phase flow patterns in a 100 μm tube [222]. (b) Halocarbon refrigerant flow patterns in a 1.1 mm tube [223]. (c) Halocarbon refrigerant flow patterns for 2.2 mm tube [224].

a decrease in surface tension at the receding side of the bubble. Overall, they also reported that thin film evaporation was the dominant mode of heat transfer and was more effective at lower receding and advancing contact angles.

Mukherjee et al. [118] further extended their study to compare the flow boiling characteristics at different contact angles. The contact angles considered in their study were 20°, 40°, 60°, and 80°. From their simulations, the heat transfer and bubble growth rate were observed to be highest at lower contact angles, owing to the formation of a liquid layer between the wall and bubble interface at the downstream, supporting the results of Lee and Son [227] and Mukherjee [228]. They also performed simulations with different wall superheats (5, 8, and 10 K), Reynolds numbers (50, 100, and 200), and surface tension (0.03, 0.04, 0.05, and 0.0589 N/m). A significant increase in the average heat transfer at the wall was observed with an increase in wall superheat due to increased bubble growth rates. However, the effect of varying the Reynolds number and surface tension on the wall heat transfer was found to be insignificant. Overall, from the studies mentioned till now, one can say that the heat flux (or wall superheat) and the contact angle significantly influences the heat transfer during flow boiling in microchannels while the effect of mass flux (or Reynolds number) is insignificant. The heat transfer is better at lower contact angles (typically less than 45°) while it increases with increase in heat flux.

Some studies have also been carried out by considering microchannels with a circular cross-section. Magnini et al. [229] performed a numerical simulation of flow boiling in a circular microchannel of 0.5 mm diameter. Three refrigerants were considered in their study, namely, R113, R245a, and R134a with mass flux ranging from 500 to 600 $\text{kg}/(\text{m}^2\text{s})$, and heat flux ranging from 5 to 20 kW/m^2 . The circular microchannel considered was a 2-D axisymmetric model. Among the fluids considered, the bubble growth rate was found to be fastest in R113 owing to a higher liquid–vapour density ratio. Magnini et al. [229] also highlighted that the evaporation from the thin film formed

between the bubble and the wall was the dominant mode of heat transfer even in circular microchannels. However, they emphasised that transient thermal effects could be relevant even in micron-sized liquid films when the bubble was not sufficiently long, and showed that the analytical solution of the 1-D unsteady heat conduction equation across the film was capturing very well the time-dependent wall temperature during the transit of a bubble.

Magnini and Thome [230] investigated the heat transfer and flow dynamics associated with slug flow boiling in circular microchannels of diameters in the range 0.3–0.7 mm. The simulations were conducted with R245a as a fluid, a mass flux in the range of 400–700 $\text{kg}/(\text{m}^2\text{s})$, heat flux of 5–20 kW/m^2 , and different values of the frequency of generation of bubbles. They reported that at low heat flux of 5 kW/m^2 , the thickness of the liquid film between the bubble and the wall increased with time. They also observed the formation of interfacial waves near the rear end of the bubble where the liquid film thickness was lower, which eventually might lead to the formation of a dryout region at higher heat fluxes. The heat transfer coefficient during the two-phase flow regime was found to be in a transient state wherein initially it was found to increase with time, but eventually reached a steady-periodic regime which happened only after a few bubbles had passed inside the channel. This suggests that analysis of single bubble dynamics may not be sufficient for a complete understanding of flow boiling heat transfer inside a microchannel.

A comparison of the flow boiling phenomenon of refrigerant inside microchannels with square and circular cross-sections was carried out by Ferrari et al. [231]. Channels with a hydraulic diameter of 100 μm with R245a as the fluid ($T_{\text{sat}} = 31^\circ\text{C}$) were considered. The heat flux was maintained constant at 5 kW/m^2 , while different mass fluxes within the range of 230–2300 $\text{kg}/(\text{m}^2\text{s})$ were considered. In the case of square channels, they observed that the shape of the bubble was axisymmetric at higher mass fluxes; at lower mass flux, the bubble was non-axisymmetric, with much thinner liquid film along the channel centre than that at the corners. Hence, they reported that the heat

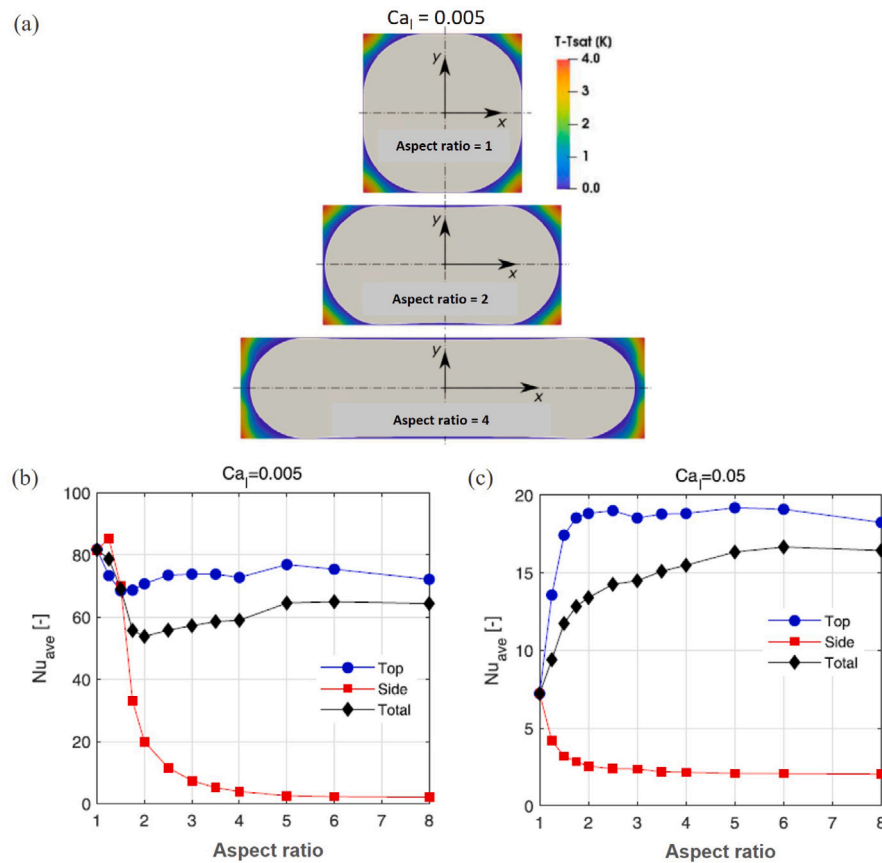


Fig. 13. (a) Cross-sectional views of the bubble (grey regions) and corresponding temperature contours for flow boiling in non-circular microchannels with different aspect ratios from the work of Magnini and Matar [232]. (b,c) Variation of Nusselt number with cross-section aspect ratio at (b) $Ca_1 = 0.005$ and (c) $Ca_1 = 0.05$ [232]. The capillary number of the liquid is calculated as $Ca_1 = \mu_l U_l / \sigma$, where U_l is the average liquid velocity.

transfer was higher in square channels at lower mass flux when the bubble was non-axisymmetric with a thinner liquid film compared to that in circular channels. In contrast, at higher mass fluxes, when the bubble was axisymmetric, the heat transfer in circular microchannels was superior to that in square channels.

Further, the effect of the cross-sectional shape of the rectangular channel on heat transfer and bubble dynamics was explored by Magnini and Matar [232]. They performed numerical simulations with channel cross-sectional aspect ratios ranging from 1 to 8, while maintaining constant hydraulic diameter, and established a direct correlation between the local liquid film thickness and local heat transfer. In their simulations, the capillary numbers tested were 0.005, 0.01, and 0.05 with a constant heat flux of 10 kW/m^2 . A comparison of temperature contours along with the profile of the bubble, taken on a cross-sectional plane located half-way along the bubble for different aspect ratios at $Ca_1 = 0.005$, is provided in Fig. 13(a). The cross-sectional distribution of the liquid film is profoundly different from circular channels, as in noncircular channels surface tension forces rearrange the liquid-vapour interface in very thin liquid films established at the walls centre and thick liquid lobes at the corners [93]. Fig. 13(b) and (c) show the variation in average Nusselt number versus aspect ratio at $Ca_1 = 0.005$ and $Ca_1 = 0.05$, respectively. From Fig. 13(b), it can be observed that, at lower capillary number ($Ca_1 = 0.005$), i.e. at lower flow rate, the square channel exhibited the best heat transfer performance owing to a very thin liquid film at the centre of the channel compared to the rectangular channels, as can be observed from Fig. 13(a). In contrast, it can be inferred from Fig. 13(c) that, at higher flow rates ($Ca_1 = 0.05$), the heat transfer performance is the lowest for the square channels since the liquid film was found to be thicker in the square channels at higher flow rates. The microchannels with higher aspect ratios showed

better heat transfer performance since they promoted the formation of extended liquid films along the longer wall. A summary of the studies that addressed the fundamental physics of bubble growth, indicating the numerical method, phase change model, simulation details, and a short description of their observation is presented in Table 3.

The numerical studies discussed thus far featured a constant liquid velocity at the inlet. It is therefore impossible to study a scenario in which a slug bubble oscillates inside the channel leading to flow reversal, since the fluid flow direction is always towards the outlet. In order to emulate this behaviour, a pressure boundary condition should be set at the inlet. Andredaki et al. [233] employed oscillating pressure boundary conditions at the inlet to study the instabilities associated with elongated bubbles inside a circular microchannel of diameter 0.5 and 1 mm during saturated flow boiling of R245a. A constant heat flux of 5 kW/m^2 was applied to the wall. They were able to observe capillary ridge formation at the leading edge of the bubble, and liquid jet penetration at the rear end of the bubble, leading to either encapsulation of droplets or detachment of small bubbles from its leading and/or its trailing edges.

3.1.2. Interaction between bubbles and bubble coalescence

In many experimental observations of flow boiling inside a microchannel, researchers have observed the nucleation of multiple bubbles [243,244]. The interaction between these multiple bubbles and their coalescence has a significant effect on heat transfer, hence, researchers have recognised the necessity to study the dynamics of multiple bubbles in detail. Dong et al. [182] investigated the effect of bubble interactions on the fluid and temperature fields during flow boiling of carbinol ($T_{sat} = 64.7 \text{ }^\circ\text{C}$) inside a 2-D microchannel of height 0.2 mm using LBM. A constant velocity of 0.486 m/s was set at the inlet with the

Table 3

Summary of studies on fundamental bubble dynamics available in the literature. Unless otherwise mentioned, the simulations are three-dimensional.

Reference	Method	Simulation details	Observations
Mukherjee and Kandlikar [225]	- Level Set method without conjugate heat transfer. - Phase change model: energy jump condition.	- Square microchannel of side $200\ \mu\text{m}$ - Fluid: water. - Inlet fluid velocity: $0.146\ \text{m/s}$, wall temperature: $107\ ^\circ\text{C}$.	- Recognised evaporation in a thin film between bubble and wall to be the prominent mode of heat transfer in microchannels. - No significant changes in the bubble growth in the presence or absence of gravity.
Fukagata et al. [234]	Level set method without conjugate heat transfer.	- 2-D axisymmetric. - Microtube of diameter $20\ \mu\text{m}$. - Fluid: water (at 1 atm, and $T_{\text{sat}} = 298\ \text{K}$). - Re_f : 16 to 490 with constant heat flux at the wall.	Enhancement in momentum exchange was observed due to the presence of strong circulations in the vicinity of the bubble which in turn increases the heat transfer in the liquid slug.
Lee and Son [227]	- Level set method without conjugate heat transfer. - Phase change model: energy jump condition.	- Square channels of hydraulic diameter 3, 0.8, and $0.4\ \text{mm}$. - Fluid: saturated water at 1 atm. - Inlet fluid velocity: $0.12\ \text{m/s}$. - Wall superheat: 5, 10, and $20\ \text{K}$. - Contact angles within the range of $30^\circ - 50^\circ$.	- Sudden expansion of bubble was observed in the case of narrow channels ($0.4\ \text{mm}$ in this case). - Heat transfer performance was observed to be best with the contact angle of 45° .
Mukherjee [228]	- Level set method without conjugate heat transfer. - Phase change model: energy jump condition.	- Geometry and boundary conditions similar to Mukherjee and Kandlikar [225]. - Advancing contact angles: 40° , 60° , and 80° . - Receding contact angles: 20° , 40° , and 60° .	Better heat transfer performance with lower contact angles, i.e. with advanced contact angle of 40° and a receding contact angle of 20° .
Mukherjee et al. [118]	- Level set method without conjugate heat transfer. - Phase change model: energy jump condition.	- Geometry and fluid similar to Mukherjee and Kandlikar [225]. - Wall superheat: 5, 8, and $10\ \text{K}$. - Reynolds number: 50, 100, and 200. - Surface tension ranging from 0.03 to $0.0589\ \text{N/m}$. - Contact angle ranging from 20 to 80° .	- Heat transfer increases with an increase in wall superheat but no significant changes were observed with variation in surface tension or Reynolds number. - Better heat transfer performance at lower contact angles.
Zu et al. [235]	- VOF method without conjugate heat transfer. - Software: ANSYS Fluent.	- Rectangular channel of cross-section $0.38\ \text{mm} \times 1.6\ \text{mm}$. - Fluid: water (at $370\ \text{K}$). - Heat flux: $210\ \text{kW/m}^2$ and mass flux: $747\ \text{kg}/(\text{m}^2\text{s})$.	They observed the variations in fluid field inside the channel and heat transfer from the channel wall in the presence of a growing bubble.
Magnini et al. [229]	- VOF model improved by Height function method without conjugate heat transfer. - Phase change model: Tanasawa [84]. - Software: ANSYS Fluent 12.	- 2-D axisymmetric. - Circular microchannel: $0.5\ \text{mm}$ diameter. - Fluid: R113, R245a, and R134a. - Mass flux ranging from 500 to $600\ \text{kg}/(\text{m}^2\text{s})$ and heat flux ranging from 5 to $20\ \text{kW/m}^2$.	At the same heat and mass flux, R113 provides a higher average heat transfer coefficient owing to a faster bubble growth rate due to the high liquid-vapour density ratio.
Jafari and Okutucu-Özyurt [236]	- Cahn-Hilliard phase field method without conjugate heat transfer. - Phase change model: Lee model. - Software: Comsol Multiphysics.	- Square channel of side $229\ \mu\text{m}$. - Fluid: water at $373\ \text{K}$. - Wall superheat: $2\ \text{K}$. - Re_f : 50, 100, and 200. - Contact angle: 20° , 40° , and 80° .	For all Reynolds numbers, heat transfer coefficient was observed to be highest when the contact angle is 30° since the bubble is elongated and the amount of thin layer trapped between the wall and the bubble nose is higher compared to other contact angles.
Jafari and Okutucu-Özyurt [237]	- Cahn-Hilliard phase field method without conjugate heat transfer. - Phase change model: Lee model. - Software: Comsol Multiphysics.	- 2-D simulations. - Square channel of side $100\ \mu\text{m}$. - Fluid: water at $298\ \text{K}$. - Mass flux: $7.97 - 255.04\ \text{kg}/(\text{m}^2\text{s})$. - Wall superheat: $2\ \text{K}$.	- Heat transfer performance during boiling was found to be 8 times that during the single phase. - Bubble generation frequency increased with an increase in mass flux up to a mass flux of $64\ \text{kg}/(\text{m}^2\text{s})$, beyond which it starts decreasing since the convective mechanism dominates nucleation at higher mass fluxes.
Magnini and Thome [230]	- VOF model improved by Height function method without conjugate heat transfer. - Phase change model: Tanasawa [84]. - Software: ANSYS Fluent 14.5.	- 2-D axisymmetric. - Circular microchannel: 0.3, 0.5 and $0.7\ \text{mm}$ diameter. - Fluid: R245a. - Mass flux: $550\ \text{kg}/(\text{m}^2\text{s})$ and heat flux: $5\ \text{kW/m}^2$.	Single or two bubble simulations might not be able to match the essential features of heat transfer in confined bubble flow.
Pan et al. [218]	- VOF method with a novel saturated interface volume phase change model. - No conjugate heat transfer. - Software: ANSYS Fluent 15.0.	- Square channel of side $0.5\ \text{mm}$. - Fluid: R113 at $323.15\ \text{K}$. - Heat flux: $9\ \text{kW/m}^2$, mass flux: $600\ \text{kg}/(\text{m}^2\text{s})$.	- Developed a novel phase change model which allows the use of non-uniform meshes. - Validated their method with the results available in the literature and demonstrated that a good match can be obtained by using their cost-effective model.

(continued on next page)

Table 3 (continued).

Reference	Method	Simulation details	Observations
Katiyar et al. [238]	- Dual grid Level set method without conjugate heat transfer. - Phase change model: Lee model.	- 2-D simulations. - Width of channel: 229 μm . - Fluid: water at 373 K. - Wall superheat: 5, 8, and 10 K. - Re_f : 50, 100, and 200. - Contact angles: 20°, 40°, 60°, 80°. - Surface tension: 0.03, 0.04, and 0.0589 N/m. - System pressure: 101.33, 198.53, 361.3, and 475.8 kPa.	- The growth rate of the bubble increases with an increase in wall superheat but decreases with an increase in contact angle and system pressure. - No prominent changes in growth rate were observed with changes in surface tension.
Ferrari et al. [231]	- VOF method without conjugate heat transfer. - Phase change model: Tanasawa model [84]. - Software: OpenFOAM 2.3.1.	- Square and circular channels with a hydraulic diameter of 100 μm . - Fluid: R245a ($T_{\text{sat}} = 31^\circ\text{C}$). - Heat flux: 5 kW/m^2 . - Mass fluxes within the range of 230 to 2300 ($\text{kg}/\text{m}^2\text{s}$).	- Bubble shape transitions from axisymmetric to non-axisymmetric in square channels with decreasing Reynolds number in square channels. - Heat transfer for square channel was found to be higher than the circular channel only at a lower Reynolds number, when the bubble shape is non-axisymmetric.
Wang et al. [112]	- Phase field method without conjugate heat transfer. - Phase change model: energy jump condition.	- Square channel of side 229 μm . - Fluid: water at $T_{\text{sat}} = 373\text{ K}$. - Boundary conditions similar to Mukherjee [228]	Aim was to see the capability of Cahn-Hilliard phase field method to simulate flow boiling in microchannels.
Magnini and Matar [232]	- VOF model without conjugate heat transfer. - Phase change model: Tanasawa [84]. - Software: OpenFOAM.	- Simulations with channel aspect ratios ranging from 1 to 8 with constant hydraulic diameter. - Fluid: R245a ($T_{\text{sat}} = 31^\circ\text{C}$). - Mass flux range: 200 to 2000 $\text{kg}/(\text{m}^2\text{s})$. - Heat flux: 10 kW/m^2	- The heat transfer performance is higher for square channels at lower flow rates, but reduces with an increase in flow rate due to an increase in film thickness. - At higher flow rates, the microchannels with higher aspect ratios showed better heat transfer performance since they promote the formation of extended liquid film along the longer wall.
Rajkotwala et al. [239]	Local front reconstruction method without conjugate heat transfer.	- 3-D simulations. - Square channel of side 198 μm . - Fluid: water at 375.15 K. - Re_f : 50, 100, and 200. - Wall superheat: 5, 8, and 10 K. - ρ_l/ρ_v : 406, 812, and 1624. - Prandtl number: 0.88, 1.76, and 2.64.	- Higher bubble growth rate and net heat transfer rate were observed at higher wall temperatures and lower liquid velocities. - The heat transfer between the bubble and the channel wall was also found to be inversely proportional to the liquid film thickness between the bubble and the wall. Bubble growth rate was found to increase with an increase in density ratio and Prandtl number.

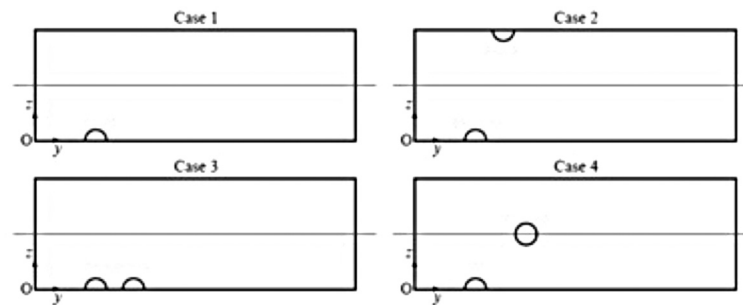


Fig. 14. Cases studied by Ling et al. [240] by considering two bubbles initiated at different locations in the channel.

wall maintained at a constant temperature of 66.4°C. The average heat transfer coefficient was observed to be approximately the same for the cases when bubbles nucleated synchronously or asynchronously from two different nucleation sites, however, the resistance to the fluid flow was higher when nucleation occurs synchronously. The effect of distance between the nucleation sites on the bubble dynamics, however, was not examined in their study.

The effect of the presence of leading and trailing bubbles on flow boiling heat transfer was investigated by Magnini et al. [245]. A circular microchannel of diameter 0.5 mm was considered in their study and this was modelled as a 2-D axisymmetric channel in which elongated slug vapour bubbles were initiated at the inlet. Two refrigerants were

considered in their study namely, R113 and R245a with mass flux ranging from 550–600 $\text{kg}/(\text{m}^2\text{s})$ and heat flux ranging from 5–20 kW/m^2 . The growth rate of the trailing bubble was found to be smaller than that of the leading one since the passage of the leading bubble reduced the temperature of the superheated liquid, such that the trailing bubble was in contact with cooler liquid. However, the heat transfer associated with the trailing bubble was considerably higher due to the overlap of perturbations caused by the bubbles on the local thermal field. Overall the heat transfer coefficient with the bubbles was found to be nearly twice that during single-phase.

The interaction between two bubbles nucleating in different spatial arrangements as shown in Fig. 14 was investigated by Ling et al. [240]. A square microchannel of side 200 μm was selected for their study with

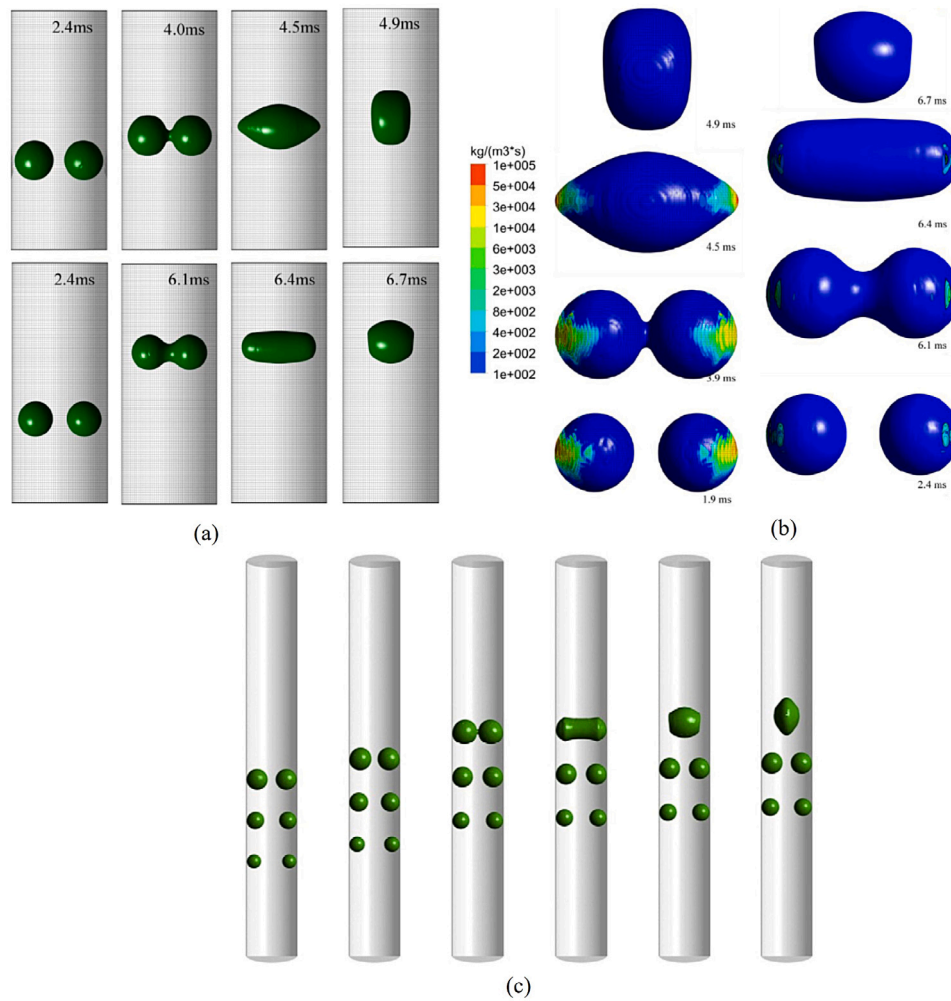


Fig. 15. (a) Interaction between two bubbles placed inside a vertical tube and (b) contours showing the variation in evaporation rate over the bubbles as the two bubbles start merging with each other [241]. (c) Flow boiling simulations with multiple bubbles placed inside a vertical tube mimicking the phenomenon of bubbly flow [242].

water as the fluid at the inlet. Fluid velocity at the inlet was kept at 0.146 m/s and the wall was maintained at superheat of 2.1 K. Four scenarios, as shown in Fig. 14, were considered in their study: a single bubble (Case 1), two bubbles initiated at the opposite sides (Case 2) and on the same side of the channel (Case 3), and two bubbles with one on the bottom wall and the other floating at the centre of the channel (Case 4). In Cases 2 and 3, they observed that the two bubbles grew equally as they slid along the walls and oscillations were produced at the interface as the bubbles merged. Because of this oscillation, they observed a temporary increase in wall heat flux as the two bubbles merged and departed from the wall. However, in Case 4 they observed that the bubble nucleated at the corner had a higher growth rate compared to the one floating in the liquid and as it grew it engulfed the floating bubble. No fluctuations in the interface were observed after merging. Since the floating bubble was relatively smaller when the merging phenomenon occurred, the heat transfer was observed to be similar to the single-bubble case. However, in all the cases studied, a temporary enhancement in wall heat flux was observed as the two bubbles merged.

Liu and Palm [241] performed numerical simulations to study the bubble growth and merging phenomenon in a vertical microtube of diameter 0.64 mm; R134a was considered as the fluid. The heat and mass fluxes considered were 14 or 28 kW/m², and 56 kg/(m²s), respectively. They placed two bubbles initially on the wall, as shown in Fig. 15(a), and observed the differences in growth and coalescence patterns at two different heat fluxes. The two bubbles were observed to grow at a faster rate when they slid along the walls. As the bubbles grew

and merged, they expanded in the radial direction and penetrated the thermal boundary layer, following which a slight enhancement in heat transfer was observed. In the later stages after merging, the bubble contracted and its growth rate diminished since it pulled the fluid away from the thermal boundary layer. The changes in the evaporation rate at different stages of the bubble growth can be seen in Fig. 15(b). Liu et al. [242] further extended the study of Liu and Palm [241] by performing numerical simulations to observe the growth and merging pattern when three pairs of spherical bubbles were placed in the microtubes (Fig. 15(c)) under different heat and mass fluxes. In another study, the heat transfer characteristics during flow boiling inside a microchannel when a train of bubbles passes inside the channel were investigated by Liu et al. [246]. They also observed that the growth rate was highest for the first bubble since it encountered a warmer liquid compared to the other bubbles. The temperature of the wall was observed to be significantly affected by the passing bubble train, with the lowest temperature observed in the region where the liquid film thickness between the bubbles and the wall was the thinnest.

Rahman and Mukherjee [247] used the Level Set method to investigate the effect of interaction between two bubbles on heat transfer in a microchannel. The geometry and the inlet fluid velocity were similar to those used by Mukherjee and Kandlikar [225]. The wall was maintained at a superheat of 8 K. The heat transfer rate was observed to be slightly higher when two bubbles did not merge as compared to the single bubble case and a case in which the two bubbles merged, owing to a smaller vapour patch on the wall. They also compared the effect

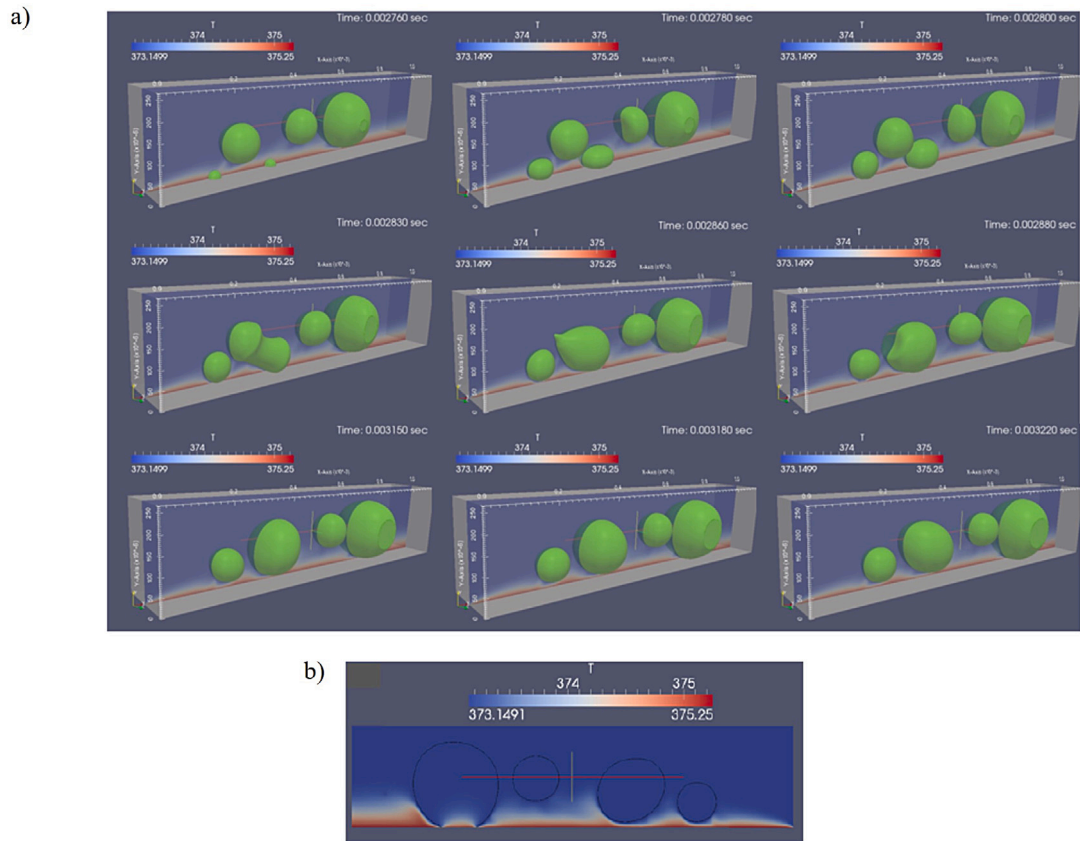


Fig. 16. Flow boiling of water in a microchannel while initiating bubble nuclei at different stages of the simulation [149].

of the contact angle on bubble growth by considering three different contact angles (20° , 40° , and 60°) and observed the presence of a thin liquid layer at the downstream of the bubbles at lower contact angle due to which heat transfer coefficient was slightly higher. They further extended this study with three bubbles placed inside the channel [248], though the observations on bubble dynamics and contact angle were very similar to the two bubble case. They also performed simulations with three different wall superheats (5 , 8 , and 11°C) and Reynolds numbers (50 , 100 , and 200). While heat transfer significantly increased with an increase in wall superheat (nearly 27.5% higher for 11°C compared to that at 5°C) owing to increased bubble growth rate, the effect of the Reynolds number on heat transfer was found to be insignificant.

While in the studies described before bubbles were initiated at the beginning of the simulation, Georgoulas and Marengo [149] repeated the nucleation events at specified time intervals and at different locations. A representative image showing the growth and merging of the bubbles can be seen in Fig. 16(a). These simulations were performed in a rectangular channel of width 0.201 mm and height 0.266 mm with water as the fluid at a Reynolds number of 100 and $T_{\text{sat}} = 100^\circ\text{C}$. The bottom wall was maintained at a constant superheat of 2.1 K . They also observed that there was significant distortion in the initial thermal boundary layer due to the growth and merging of bubbles (as seen in Fig. 16(b)) resulting in an enhancement in heat transfer. Guo et al. [249] further investigated the effect of waiting time, i.e. the time between a bubble departing from a nucleating site and the formation of the new bubble, on heat transfer. 2-D simulations were performed with a microchannel having a width of 0.2 mm with water as fluid. The Reynolds number was set to 100 , and the wall was maintained at a superheat of 5 K . For the waiting time period range considered in their study, the average Nusselt number was found to be inversely proportional to the waiting time owing to an increase in the number

of bubbles resulting in an increase in the number of thin liquid films between the bubble and the wall.

3.1.3. Flow pattern transitions and annular flow

A number of computational studies focused also on the transitions among two-phase flow patterns during boiling in microchannels. Zhuan and Wang [189] conducted 2-D simulations to visualise and analyse the flow pattern transitions during flow boiling of R134a inside a microchannel of height 0.5 mm and length 70.7 mm . The heat and mass flux considered were in the range of $4 - 129\text{ kW/m}^2$ and $350 - 2000\text{ kg/(m}^2\text{s)}$, respectively. Fig. 17(a) shows the flow pattern map for R134a in which region A represents the transition from bubbly to slug flow wherein the bubbles coalesce to form slug bubbles. In contrast, region B represents the transition from slug to semi-annular flow wherein the slug bubbles grow and coalesce to form semi-annular flow. A comparison between numerical and experimental observations of flow patterns can also be seen in the figure and the results obtained from their simulations were consistent with the experimental results. The effect of aspect ratio on the flow boiling of water ($T_{\text{sat}} = 60^\circ\text{C}$) when a non-uniform heat flux was applied from the bottom of the wall was investigated by Yan et al. [250]. They considered a microchannel of $142\text{ }\mu\text{m}$ hydraulic diameter with aspect ratios ranging from 1 to 5 . The mass flux used was $500\text{ kg/(m}^2\text{s)}$ and the non-uniformity in the heat flux was obtained by applying heat flux in the range of $0 - 270\text{ W/cm}^2$ in different sections of the bottom wall (as shown in Fig. 17(b)). The wall temperature was observed to be the lowest for the microchannel with an aspect ratio of 1 . The transition from dispersed bubbly flow to confined bubble flow happened faster in microchannels with a lower aspect ratio as compared to the same in a higher aspect ratio. Under the same heat and mass flux conditions, the heat transfer coefficient increased with increasing aspect ratio only near the inlet section, which they attributed to high heat flux density and lower wall temperature.

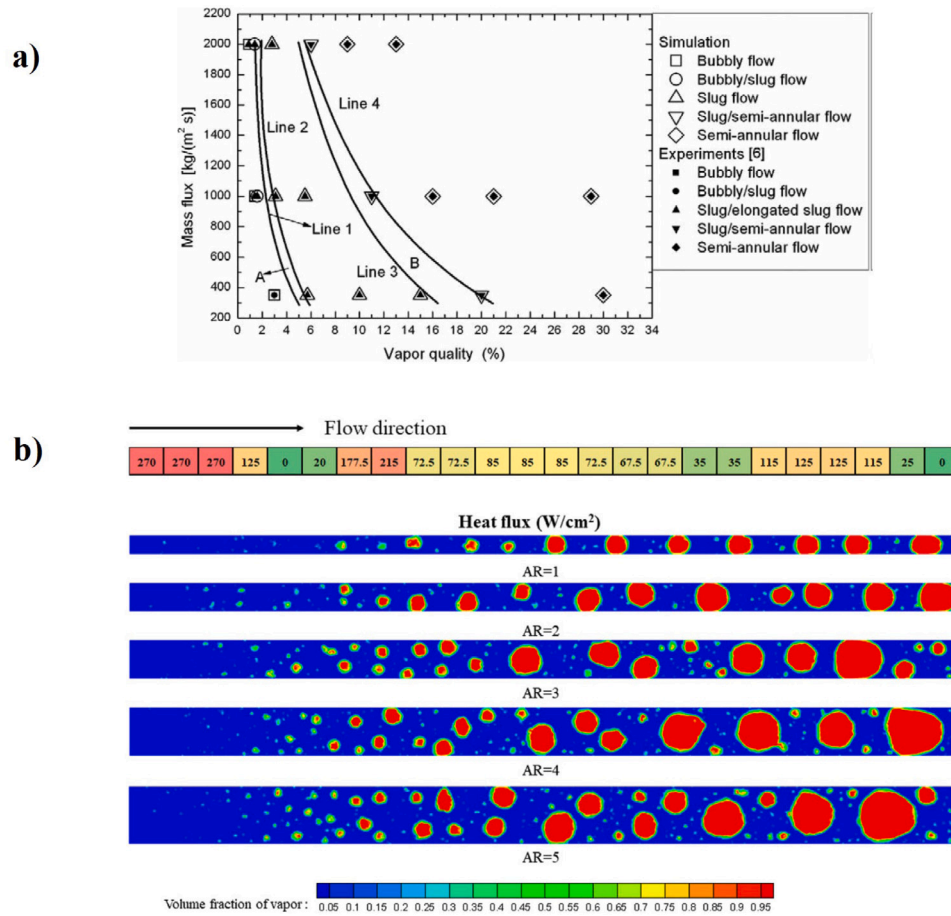


Fig. 17. (a) Flow pattern map for R134a for $D_h = 0.5$ mm, $T_{\text{sat}} = 30$ °C [189]. (b) Heat flux applied on different sections of the bottom wall of a microchannel and variation in flow pattern with changes in aspect ratio [250].

In the channel downstream, the heat transfer coefficient remained nearly the same for all aspect ratios. The two-phase pressure drop was found to be independent of changes in aspect ratio. To simulate flow boiling under marine motion, Tian et al. [202] introduced the effect of rolling motion by adding an additional force in the momentum equation. Two-dimensional numerical simulations were performed with a channel of height of 4 mm and length of 400 mm with water as the fluid. Rolling amplitude and rolling period considered were in the range of $10^\circ - 20^\circ$ and $1 - 2$ s, respectively. While comparing the flow patterns under static and rolling conditions, they observed bubbly, slug, and annular flow patterns in the former, whereas, only bubbly flow was observed in the latter case owing to a reduction in coalescence of bubbles under rolling motion. They compared the differences in CHF (critical heat flux) variation trends under rolling motion with that under static conditions and noticed a significant reduction in CHF when rolling motion was introduced which in turn resulted in a reduction in heat transfer capacity of the microchannel. Hence, they concluded that, when designing a heat exchange device for marine conditions, the assessment of the performance of the heat exchanger should be made by considering the effect of rolling motion. However, they have observed up to 30% deviation in CHF results obtained from their simulations as compared to the experimental results of Qu and Mudawar [200]. This might be because these simulations are two dimensional and cannot appropriately predict the dry patches at the wall.

In the studies mentioned above, the focus was mainly on the dispersed bubble or slug/confined bubble flow regimes. However, Cheng et al. [13] pointed out in their review of experiments on boiling in microchannels that, while nucleation dominates near the upstream of the microchannel, film evaporation in annular flow becomes prominent

at the downstream. Moreover, Zhang et al. [251] in their experiments with microchannels of hydraulic diameters ranging from 25 to 60 μm , observed annular flow to prevail over bubbly or slug flow. Guo et al. [24] performed 2-D CFD simulations of flow boiling of water, focusing specifically on annular flow. They considered tubes of hydraulic diameters ranging from 0.5 to 2 mm, heat flux ranging from 5 – 40 kW/m^2 , and mass flux ranging from 50 – 180 $\text{kg}/(\text{m}^2\text{s})$. The heat transfer coefficient was observed to increase with an increase in heat and mass flux but reduced with an increase in hydraulic diameter. Liu et al. [252] identified the lack of studies available on understanding the heat transfer variations during flow pattern transitions and performed numerical simulations to study slug to annular flow transition using a coupled level-set and VOF method. A microchannel of diameter 0.4 mm was considered on which a constant heat flux of 160 kW/m^2 was applied. Water was considered as a working fluid with inlet mass flux of 400 $\text{kg}/(\text{m}^2\text{s})$. They initialised a bubble and an annulus in the channel and observed the evolution of the flow pattern from slug to annular flow. The disturbance in the thermal boundary layer as the trailing bubble coalesced with the annulus resulted in faster growth of the trailing bubble. Luo et al. [253] conducted a three-dimensional numerical study of annular flow in a narrow rectangular channel of cross-section 0.5×0.5 mm^2 with water as a fluid, heat flux ranging from 6.7 to 20 W/cm^2 and two different mass fluxes (240 and 360 $\text{kg}/(\text{m}^2\text{s})$). Augmentation in heat transfer coefficient was observed with an increase in applied heat flux owing to a decrease in the liquid film thickness. Conversely, the heat transfer coefficient decreased with an increase in mass flux. In order to study the interfacial behaviour as the flow pattern transitioned from bubbly to annular flow, Yeo and Lee [196] performed 2-D simulations of flow boiling of R134a in

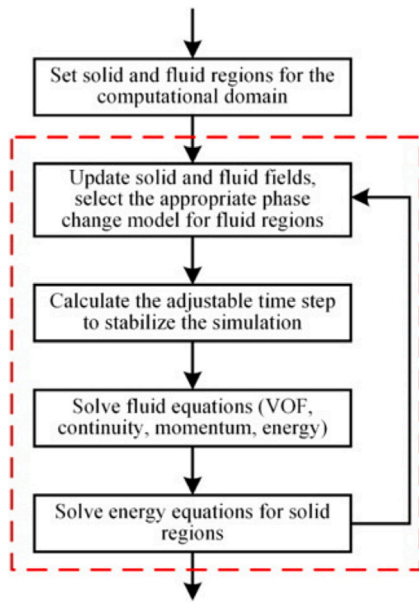


Fig. 18. Solution algorithm for solving phase change problem including conjugate heat transfer between fluid and solid regions [258].

microchannels with a large length-to-diameter ratio (diameter of 1 mm and length of 609.6 mm). They reported that 2-D simulations can predict flow patterns with reasonable accuracy from bubbly flow up to annular flow, but during the annular flow regime, a pseudo-dry-out situation arose leading to an unexpected rise in temperature. They suggested that such problems cannot be solved just by increasing the grid resolution but can be probably handled by adopting 3-D simulations.

It is evident that annular flows have received far less attention than bubbly and slug flows in terms of numerical simulations, while up to the authors' knowledge, there are no studies which attempted to model dryout and critical heat flux in microchannels. One possible reason is that annular flows are particularly challenging for what concerns resolving the thin liquid films at the wall, requiring intensive computational resources unless efficient adaptive mesh refinement is implemented. Furthermore, even within microchannels, the flow in the high-speed vapour core may become turbulent, but turbulence models for two-phase flow simulations are still poorly established. Most of the computational studies of annular flows in turbulent regimes in conventional size channels [254,255] employed RANS and the $k-\omega$ SST [256] model. However, RANS turbulence models were developed for single-phase flows and their application in two-phase simulations is not robust. For annular flows, it has been demonstrated that RANS turbulence models tend to overestimate turbulence near interfaces and thus various turbulence damping strategies have been recently proposed [257]. However, these are still empirical adjustments relying on a damping factor whose values are case-dependent, and no attempt has yet been made to verify its effectiveness for annular flow simulations in microchannels. Hence, significant developments of the numerical algorithms, as well as physical descriptions of two-phase turbulence, are necessary to make numerical simulations a robust tool to investigate flow regimes leading to dryout and critical heat flux, which are of paramount importance, for example, in electronics cooling.

3.2. Conjugate heat transfer

Microevaporators during operational conditions are usually in contact with the surface to be refrigerated only on one side. The overall heat transfer mechanism involves heat conduction through the solid and then convection to the fluid. Therefore, heat distribution is highly

nonuniform and requires the solution of a conjugate heat transfer problem. It can be seen from Table 3 that most studies have not considered conjugate heat transfer effects, and have performed simulations essentially assuming the wall thickness to be zero and heat to be conducted only perpendicular to the fluid flow with negligible axial conduction in the wall. This assumption can be valid for macrochannels in which the ratio of solid wall thickness to fluid domain thickness is very low and length over height ratio of the channel is very high. In the case of microchannels, however, the scale of the wall thickness is very similar to that of the fluid flow channel, and the length of the heat sink is comparable to its overall width and height. Hence, axial heat conduction cannot be ignored in microchannels [259]. Maranzana et al. [260] proposed an axial conduction number, Ma , to assess the rate of axial heat conduction which is given by,

$$Ma = \frac{q_{cond}}{q_{conv}} = \frac{k_s e_w}{G c_{p,f} e_f L_{heated}} \quad (61)$$

where e_w and e_f are the wall and channel thickness, respectively, L_{heated} is the length of the heated section of the channel, G is the mass flux, $c_{p,f}$ is the specific heat of fluid, and k_s is the thermal conductivity of the wall. Maranzana et al. [260] proposed that axial conduction and hence conjugate heat transfer cannot be neglected if $Ma > 0.01$.

The numerical model and the solution algorithm for considering conjugate heat transfer between fluid and solid domains involving phase change was described by Luo et al. [258]. In this model, the energy equations for the liquid and the solid regions are solved separately. Conjugate heat transfer within the solid region is accounted for by solving the heat conduction equation:

$$\rho_s \frac{\partial}{\partial t} (c_{p,s} T_s) = \nabla \cdot (k_s \nabla T_s), \quad (62)$$

where k_s and $c_{p,s}$ are the (potentially temperature-dependent) solid thermal conductivity and specific heat capacity, and T_s and ρ_s are the solid temperature and density, respectively. The solid and fluid temperature (T_f) fields are coupled by imposing continuity of temperature and heat flux, at the boundary between solid and fluid regions, given by Eqs. (63) and (64), respectively:

$$T_s = T_f, \quad (63)$$

$$k_f \frac{\partial T_f}{\partial n} = k_s \frac{\partial T_s}{\partial n}, \quad (64)$$

where k_f is the fluid thermal conductivity. The solution algorithm adopted by Luo et al. [258] is sketched in Fig. 18. A similar method has been adopted to solve the conjugate heat transfer problem in most of the research articles cited in this section. Since the energy equations for fluid and solid are coupled at the common boundary, they must be solved iteratively with a predictor–corrector approach until the fluid and solid temperature solutions at the boundary satisfy both Eqs. (63) and (64); a viable alternative is to implement an implicit coupling where the fluid and solid energy equations are discretised within a single matrix [82]. The effect of thickness and the material properties of the wall on flow boiling heat transfer in a square microchannel was studied by Lin et al. [261]. A square microchannel of side $200 \mu\text{m}$ was considered with different bottom wall thicknesses ranging from 5 to $160 \mu\text{m}$ and different wall materials, silicon, aluminium, and copper. Water with a saturation temperature of 373.15 K and uniform velocity of 0.147 m/s was used as the fluid with a constant heat flux of 100 kW/m^2 applied at the bottom of the wall. They showed that both the bubble growth rate and heat transfer performance depended on the wall thickness. A higher bubble growth rate was observed when the thickness and the thermal diffusivity of the wall were higher, as shown in Fig. 19(a). The heat transfer coefficient was observed to be initially lower for higher wall thickness since the increase in wall thickness not only resulted in an increase in thermal resistance, but it also yielded a decrease in the single phase heat transfer coefficient. However, the increase in the rate of phase change enhanced the heat transfer performance at the later stages (Fig. 19(b)).

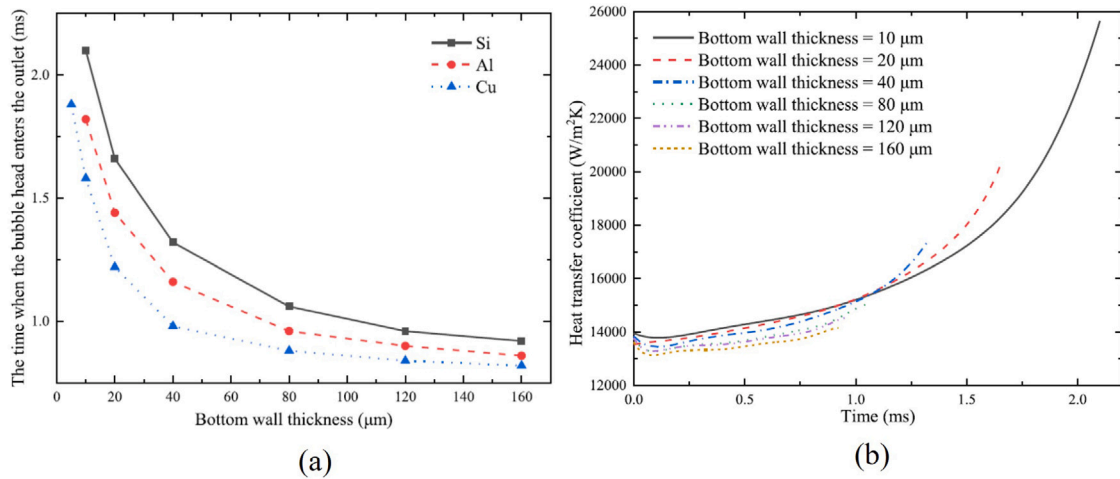


Fig. 19. (a) Comparison of the time when the bubble head enters the microchannel outlet for different solid materials and (b) comparison of the space-average heat transfer coefficient for different wall thicknesses [261].

Municchi et al. [199] modelled a microchannel with the surrounding lateral and base walls, with heat provided only through the base wall, to emulate the three-side heating configuration usually encountered in experiments. They studied different noncircular channels with cross-sectional aspect-ratios ranging from 0.25 to 4, while fixing the hydraulic diameter to $0.229 \mu\text{m}$. Water at atmospheric pressure was considered as working fluid, with a heat flux of 100 kW/m^2 applied on the outer surface of the bottom wall. Different values of the thickness of the walls between the channels were tested. The effect of the variation of the wall thickness and channel aspect-ratio on the base wall temperature and Nusselt number can be seen in Fig. 20. The base temperature increased monotonically with both aspect-ratio and wall thickness due to the increased overall thermal resistance of the evaporator. The Nusselt numbers were higher for thicker walls because the higher temperatures enabled less dryout as the bubbles were growing faster. However, the trends of Nu versus the aspect-ratio were not monotonic owing to the complex bubble and thin film dynamics. In a follow-up study [178], the same group investigated the impact of a number of operating parameters such as heat flux, wetting conditions, fluid and solid material. They observed a common trend where lower aspect-ratio channels (of height larger than their width) provided better heat transfer performances, in particular for hydrophilic walls which gave much higher Nusselt numbers owing to the formation of extended evaporating liquid films.

Andredaki et al. [217] also investigated the effect of channel aspect ratio on the flow boiling of ethanol inside microchannels by including conjugate heat transfer between the solid and the fluid domain. A microchannel of hydraulic diameter $200 \mu\text{m}$ was selected with three different aspect ratios (0.5, 1.0, and 2.5). The heat and mass flux range considered were 20 to 100 kW/m^2 and 73 to $687.6 \text{ kg/(m}^2\text{s)}$, respectively. The channel aspect ratio was found to have a significant effect on heat transfer inside microchannels as it governs the single-phase heat transfer, bubble dynamics, and the mode of heat transfer. At low heat fluxes, they observed that the dominant mode of heat transfer was liquid film evaporation for narrow channels (aspect ratio = 0.5) while for the square (aspect ratio = 1) and wide channels (aspect ratio = 2.5), it was found that contact line evaporation dominated. With an increase in heat flux, however, liquid film evaporation was found to be the dominant mode for all the channel aspect ratios considered. They also reported, based on the global Nusselt number, that the highest heat transfer was observed in the case of wide channels majorly owing to the significant improvement in heat transfer during the single-phase flow stage. The effect of channel aspect ratio on the dynamics of bubbles when multiple bubbles were seeded initially inside the channel at arbitrary locations was also investigated. For all the aspect ratios considered in their study,

they observed that the arbitrarily distributed bubbles merged rapidly leading to the formation of elongated vapour slug initially, but observed smaller bubbles with slug-plug flow arrangement at the later stages. The size and length of the bubbles at this stage though were dependent upon the channel aspect ratio, as the elongated length of the vapour bubble increased with the channel aspect ratio.

Vontas et al. [150] further investigated the effect of varying thermo-physical properties of the solid surface of the microchannel on boiling heat transfer characteristics. Flow boiling simulations with conjugate heat transfer were conducted and a comparison of the heat transfer performance of five different solid materials (including aluminium, brass, copper, silver, and stainless steel) was made. A microchannel of width $150 \mu\text{m}$ and height $300 \mu\text{m}$ with a solid base wall of thickness $90 \mu\text{m}$ was considered in their study. Ethanol was used as the fluid with a mass flux of $150 \text{ kg/(m}^2\text{s)}$ and a constant heat flux of 20 kW/m^2 was applied at the bottom of the wall. During the boiling simulations, they seeded 30 bubbles (distributed randomly over the entire bottom wall) after every 0.5 s in the simulation domain so as to mimic a realistic boiling scenario wherein multiple recurring nucleation events can be observed. They observed that, in the microchannels with higher thermal conductivity surfaces such as aluminium, silver, and copper, the bubble coalescence rate was higher resulting in larger volume slugs and lesser bubbly flow regime, which in turn resulted in better heat transfer performance compared to brass and stainless steel. They also modified an existing correlation to predict the Nusselt number provided by Li and Wu [207] to include the effect of thermophysical properties of the solid surface.

3.3. Multi-channel configurations

Generally, a microchannel heat exchanger includes multiple channels arranged parallel to each other wherein all the microchannels are connected to the same inlet and outlet header. Hence, efforts have been made by researchers to extend numerical simulations to study bubble dynamics and heat transfer characteristics of parallel microchannels. Suh et al. [263] used the level set method to understand the dynamics of bubble growth in parallel channels. Heat sinks with two and three-parallel microchannels were considered in their study with each channel having a height of 0.2 mm and a width of 0.4 mm . The wall thickness and distance from the inlet to the dividing wall were kept at 0.1 mm and 0.125 mm , respectively. The effects of contact angle (30° and 40°) and wall superheat (5 , 10 , and 15 K) were also investigated. They observed that, in both the heat sinks, especially in the case when bubble nucleation does not happen simultaneously in both channels, the flow reversal phenomenon occurs as the bubble in one channel

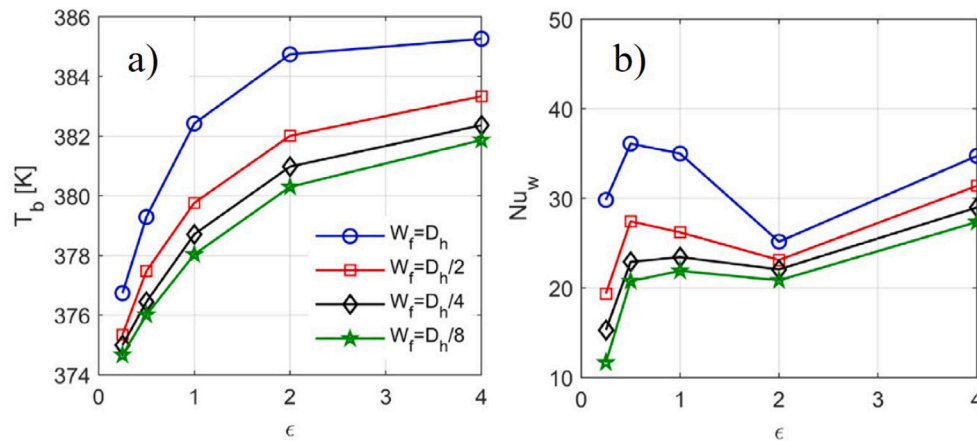


Fig. 20. Impact of cross-sectional aspect-ratio (ϵ) and thickness of the fin between parallel channels (W_f) on the (a) base evaporator temperature and on the (b) spatially-averaged Nusselt number [199].

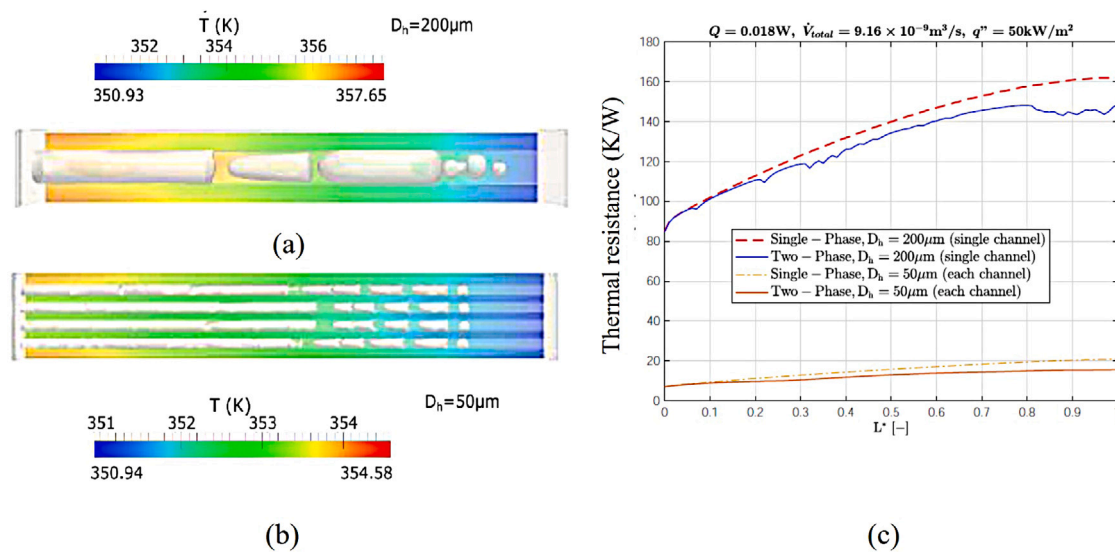


Fig. 21. Comparison of flow pattern during boiling inside (a) single and (b) multi-channel setup. (c) Comparison of thermal resistance for single and multi-channel heat sinks. Images are adapted from Vontas et al. [262].

grows in both upstream and downstream directions. The backward bubble growth also resulted in a decrease in boiling heat transfer in parallel channels. In the case when bubble nucleation happened at the same time in both channels, flow reversal was not observed. Further, the reversed flow condition was observed to be strongly dependent on wall superheat and contact angle as it became more pronounced at higher wall superheat and lower contact angle.

Vontas et al. [262] compared the performance of a single microchannel of hydraulic diameter $200 \mu\text{m}$ with a microchannel comprising four channels of hydraulic diameter $50 \mu\text{m}$ arranged parallel to each other. In both cases, the heat flux, volumetric flow rate, wall thickness, and aspect ratio were kept the same while having 30 bubbles seeded every 0.4 ms in both channels. Fig. 21(a) and (b) show the difference in flow patterns in single and multi-microchannels, respectively. It can be observed that the flow pattern in the single channel transformed to slug flow towards the end of the channel, whereas churn flow was observed in all the channels in the multichannel setup. From the temperature profiles, it can be inferred that the spatial temperature gradient was lower in the case of multiple channels ($\Delta T = 3.6 \text{ K}$ for multichannels compared to $\Delta T = 6.7 \text{ K}$ for single channel). Moreover, the convective thermal resistance was also significantly lesser for multiple channels as compared to the single channel case, as exemplified in Fig. 21(c). The authors attributed these advantages to the presence of thinner liquid

film in the multiple channel case, induced by the smaller hydraulic diameter of each channel compared to the single channel case. This resulted in an increase in the convective heat transfer coefficient and the overall transfer performance for the multiple channels cases. Lin et al. [264] attempted to address the issue of flow boiling instability in parallel microchannels by comparing the single bubble growth in one of the channels in a straight parallel microchannel with that of parallel microchannels with microgap and a finned microchannel. Each microchannel had a cross-section of $200 \times 200 \mu\text{m}^2$. The difference in bubble dynamics in a traditional parallel microchannel and a finned microchannel can be seen in Fig. 22. Among the channels considered in their study, they observed that flow reversal could be mitigated by finned microchannels, as the bubble growing in one channel would flow into the neighbouring channels through the gap between the fins.

3.4. Summary and challenges

Studies involving flow boiling in microchannels are still being conducted without considering conjugate heat transfer effects. As mentioned before, in the case of microchannels, ignoring the axial heat conduction leads to erroneous results in Nusselt number, especially when the thermal conductivity ratio of solid to fluid is very high. Since

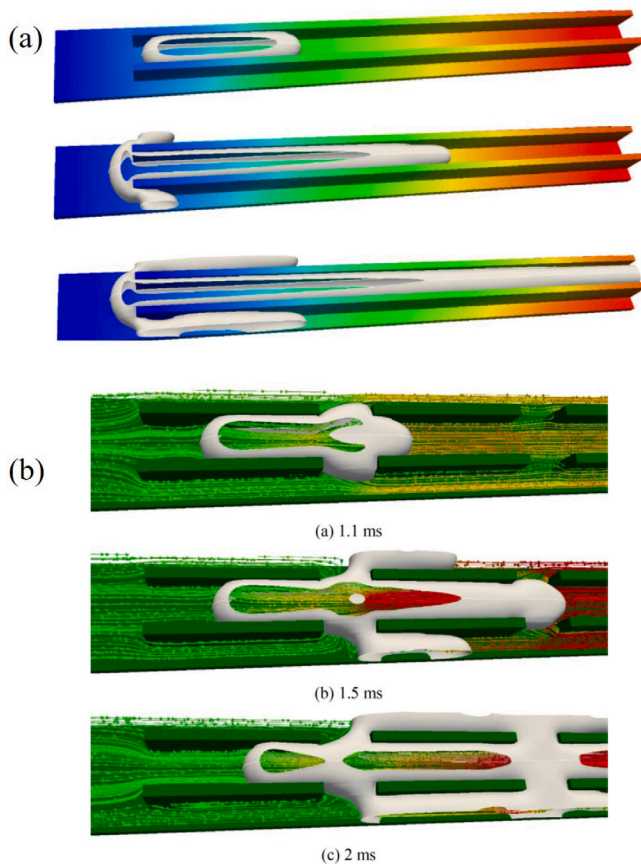


Fig. 22. Bubble dynamics inside (a) a traditional microchannel, and (b) a fined microchannel. The bubble growth in upstream direction leading to the bubble flowing back into the inlet chamber can be seen in (a), whereas in case (b) only downstream movement of the bubble is observed [264].

usually a microchannel heat exchanger is made up of high thermal conductivity metals with refrigerants in the fluid flow channel which have comparatively lower thermal conductivity, it is important to consider conjugate heat transfer effects to assess the heat transfer performance accurately.

Three types of flow patterns have been identified in microchannels through experiments, namely, isolated bubble, confined bubble or slug flow, and annular flow [265]. The evaporation of thin film around the confined bubble has been recognised to be a dominant mode of heat transfer [266]. Hence, extensive research using numerical simulations can be found considering heat transfer analysis during the evolution of a single bubble into a slug flow. However, accurately simulating different flow patterns such as the coalescence and breakup of multiple bubbles, and annular flow in microchannels is particularly challenging chiefly because of the requirement of high resolutions and accurate modelling of complex phenomena involved in such cases. In the case of simulating multiple bubbles, interface reconstruction is a significant challenge especially in grid-based methods since it is difficult to accurately reconstruct interfaces between multiple bubbles, with numerical diffusion and merging of interfaces resulting in incorrect bubble shapes and interaction dynamics. Furthermore, the presence of multiple bubbles creates complex flow patterns, including recirculation zones and vortices which require fine meshes and small time-steps for stable and accurate solutions. Annular flows are particularly challenging due to the very fine meshes required to capture the liquid film dynamics and the fact that, even in microchannels, the vapour core may flow in a turbulent regime. The latter is a critical characteristic, as turbulence models for two-phase simulations are poorly established

and even more so for annular flows in microchannels. This has resulted in a very limited availability of numerical studies of annular flows in microchannels. Since annular flow is likely the flow pattern which occupies the largest area in microchannel flow pattern maps, there is a need for significant computational developments to enable robust simulations of these flows.

Conjugate heat transfer in microchannels is another aspect that has received insufficient attention in numerical simulations so far. Although several studies have emphasised that conjugate heat transfer plays an important role in a microevaporator due to the fact that channels have sizes comparable to the wall surrounding them, many simulation studies still do not account for it. Conjugate heat transfer libraries are readily available in commercial simulation software but may be challenging to implement in open-source and in-house software, however, it emerges as a key requirement for high-fidelity simulations of boiling in microchannels.

Simulating a multi-microchannel involving complex phenomena such as phase change demands a high computational requirement. Hence, we see considerably fewer research articles published on flow boiling inside multi-microchannels. Saenen and Thome [267] developed a dynamic numerical evaporator model to study the instabilities occurring in parallel microchannels. They solved the one-dimensional homogeneous two-phase flow conservation equations to simulate the flow in the parallel channels with common inlet and outlet manifolds, thus being able to reproduce stable and unstable flow configurations from experiments. This approach offers a cost-effective means to simulate flow boiling in multi-channel systems. The 3-D simulation of an entire multi-microchannels evaporator is still a prohibitive task due to the computational requirements, for example, the heat sink studied experimentally by Szczukiewicz et al. [268] incorporated 67 parallel channels. Nonetheless, adaptive mesh refinement techniques may be valuable to reduce the computational task by adopting a coarse mesh which becomes refined only across the fluid interface. Although commercial codes and open-source software such as OpenFOAM do offer adaptive mesh refinement, the out-of-the-box libraries lack load balancing and thus are inefficient in the presence of two-phase flows with large topology changes (e.g. bubbly and slug flows).

Further, there is a need to devise a method to understand flow boiling instability even with a single channel. However, as reported before, with constant velocity boundary conditions at the inlet, no observations on reverse flow boiling instability scenarios can be made with a single microchannel setup. There is only one study by Andredaki et al. [233] in which they have explored the possibilities of using pressure boundary conditions at the inlet. But even in their study, they had considered a slug bubble of a certain initial length and different mechanisms might be revealed when different initial lengths of bubble are considered. Ideally, the pressure oscillations to be used as boundary conditions should come from time-dependent pressure data from experiments, or from a wider model of the microevaporator.

4. Applications: Heat transfer enhancement

Heat transfer enhancement represents a very active research field for flow boiling in microchannels, fuelled in particular by the tremendous cooling challenges faced by the IT industry, where the average heat flux to be dissipated from microprocessor chips is predicted to reach 4.5 MW/m^2 by 2026, with peaks of 45 MW/m^2 in the presence of hot spots [1]. Methods for heat transfer enhancement can be broadly classified into two categories, namely, active and passive methods. Active methods promote heat transfer enhancement by introducing rotation, vibration, electric or magnetic fields from an external power source, but are difficult to implement in a microscale system due to its compact size. Experimental observations suggest that passive methods, involving enhancement through modification of heat transfer geometry and surfaces, provide remarkable improvement in heat transfer; a comprehensive review on heat transfer enhancement in

microchannels can be found in Deng et al. [12], while Mahmoud and Karayiannis [269] compiled studies dedicated to enhancement in pool boiling. This section focuses on the numerical studies that investigated heat transfer enhancement through different passive techniques: use of micro-structured surfaces in Section 4.1, wettability patterns in Section 4.2, enhancement of flow geometry in Section 4.3.

4.1. Micro-structured surfaces

Experimental observations suggest that heat transfer enhancement can be obtained either by providing microstructures such as fins/pin fins which provide enhancement by disrupting the flow [270], or by providing artificial nucleation cavities/re-entrant cavities which improve the heat transfer performance by promoting bubble nucleation [271]. Lee et al. [272] performed numerical simulations to study the bubble dynamics during flow boiling inside a microchannel with and without transverse fins using the level set method. In their study, a microchannel of width 400 μm , height 200 μm , and length 4 mm was considered with saturated water as the fluid at the inlet having a uniform velocity of 0.3 m/s. The bottom wall was maintained at a constant temperature of 110 $^{\circ}\text{C}$. The effect of fin height and pitch on the growth rate of the bubble and the heat transfer performance of the microchannel was studied by considering fins of height ranging from 0–50 μm and pitch ranging from 0–200 μm . The growth rate of the bubble and the heat transfer coefficient increased with the introduction of transverse fins as compared to a plain microchannel. They attributed this increase to the increased contact between the liquid-vapour-solid interface due to the addition of fins and liquid trapped between the fins. Interestingly, they observed a higher heat transfer performance with shorter fin height and higher spacing between the fins since the liquid-vapour interface stayed in contact with both fins and the bottom wall in the inter-fin region with these fin configurations. Overall enhancement in heat transfer of up to 33% based on total fin surface area was reported. Lee and Son [273] further continued this research to compare the heat transfer performance of the microchannel with longitudinal and transverse fins. Fig. 23(a) and (b) show the configuration of the transverse and longitudinal microchannels that were considered in their study. The channel dimension, fluid properties, and boundary conditions were similar to those considered by Lee et al. [272]. An increase in heat transfer in the range of 49–59% was observed for finned microchannels as compared to the plain microchannels, with higher heat transfer enhancement observed for microchannels having longitudinal fins. However, both of these studies were conducted with one single wall temperature and fluid inlet velocity, and therefore their impact on heat transfer was not assessed. Furthermore, in experiments on microchannels with fins, especially at lower effective heat fluxes and vapour quality, nucleate boiling is still observed to be a dominant heat transfer mechanism with bubble nucleation being observed from the walls of the fins [274]. However, nucleation cannot be observed when using phase change models such as the Hertz-Knudsen-Schrage model [83], which is one of the limitations of numerical simulations.

Lorenzini and Joshi [275] conducted numerical simulations of flow boiling of HFE-7100 (at $T_{\text{sat}} = 81^{\circ}\text{C}$) flowing inside a microchannel of height 200 μm and width 500 μm with variable pin fin densities over its surface. The pin fins considered were of height 200 μm and diameter 150 μm with pitch 225 μm in both transverse and longitudinal directions everywhere, except in three hot-spot arrays (near the entrance, centre, and exit regions) where pin fins of diameter 75 μm with pitches of 112.5 μm were used, as shown in Fig. 23(c) wherein the red boxes indicate the hotspot locations where higher density of pin fins was produced. At the inlet, a mass flow rate of $1.099 \cdot 10^{-7}$ kg/s was specified, with a base heat flux of 30 W/cm², while the heat flux at the three hot-spot regions was varied from 60 to 120 W/cm². With the pin fins, the wall maintained a relatively uniform temperature. When the applied heat flux was highest at the inlet or exit hot-spots, the rise in local temperature was observed to be lesser compared to that achieved when

the heat flux was highest at the central hot-spot location. Based on these observations, they suggested that in a microcooling system, it is better to place the microchannel such that the region with higher heat flux conditions is either at the inlet or exit of the channel. The effect of variation in dimensions of the pin geometry was however not investigated. Studying the variations in flow boiling behaviour with varying geometry parameters of pin fins will be important to get a heat transfer optimised geometry of the structure. Li et al. [276] studied flow boiling in an elliptical microchannel (hydraulic diameter of 1.7 mm) with microfins. R410 A refrigerant (at $T_{\text{sat}} = 278.15$ K) was considered as fluid in their study with heat and mass flux of 3 kW/m² and 150 kg/(m²s), respectively. An increase in the heat transfer area and a reduction in dryout area with flow converting into an annular flow regime was observed, which favoured improvement in boiling heat transfer. Chen et al. [220] performed 2-D simulations of flow boiling in microchannels with micropillar surfaces using LBM. They observed that there was an optimum value for the number of pillars or height of pillars, beyond which increasing these geometric parameters resulted in deterioration of heat transfer enhancement. They defined a parameter named pillar geometric factor S_p ($S_p = (W_p + D_p)/H_p$, where, W_p , H_p , and D_p represent width, height, and distance between pillars) and reported that the optimum value of S_p was 7, beyond which heat transfer enhancement started diminishing. The effect of providing biphilic pattern on the micropillared surfaces having different wettability conditions on the top, bottom, and sides of the pillars was also investigated. They observed enhancement of up to 105% when they had a superhydrophobic surface on the top and a hydrophilic surface on the bottom and side regions. More recently, El Mellas et al. [151,277] performed fundamental studies of two-phase flows within micro-pin fin evaporators both in adiabatic [277] and boiling conditions [151]. The authors replicated the geometry and conditions of Falsetti et al. [197], where refrigerant R236fa was used in a micro-pin evaporator with in-line pin fins of diameter of 50 μm and height 100 μm . The pin-fins were observed to enhance heat transfer via a combined effect of film evaporation, as the bubbles trapped a thin liquid layer around them, and heat convection in the gaps between the cylinders, achieving Nusselt numbers up to 50% higher than single-phase flow. The effect of mass flux and inlet subcooling was also investigated, keeping the pin-fin arrangement and size constant, and therefore no systematic analysis of the geometry of the pin-fins was conducted.

Few numerical studies have investigated heat transfer enhancement by providing nucleation cavities/re-entrant cavities. Zhou et al. [278], with the help of 2-D numerical simulations using the level set method, studied the effect of introducing re-entrant cavities in a microchannel. A microchannel of width 200 μm was considered in their study with water as the fluid having a constant mass flux of 80 kg/(m²s). The heat flux applied was in the range of 30 to 190 kW/m². Promotion in stable and continuous bubble formation at lower superheating was observed due to the presence of re-entrant cavities. They also reported an increase in critical heat flux for the microchannels with re-entrant cavities as compared to the plain microchannels. Further simulations with different cavity heights, widths, and diameters were also performed to find an optimal re-entrant geometry configuration that offered the best heat transfer performance. This was achieved for cavity mouth opening of 9.5 μm , depth of 60 μm and diameter of 120 μm . Lin et al. [26] investigated the effect of having microstructures such as microcavities or microfins on the flow boiling of water inside silicon microchannels using the VOF method with the Lee model [89] for handling phase change. A microchannel of hydraulic diameter 200 μm and length 1200 μm was considered in their study. The micro-structured surface was formed by providing fins of height, width, length, and spacing of 25 μm , while the surface with microcavity was developed by providing cavities of equivalent dimensions. The simulations were also performed with three different contact angles (5 $^{\circ}$, 30 $^{\circ}$, and 60 $^{\circ}$) to understand the effect of surface wettability on heat transfer. Saturated water (at pressure of 1 atm) was used as a fluid with a mass flux of 500 kg/(m²s) while

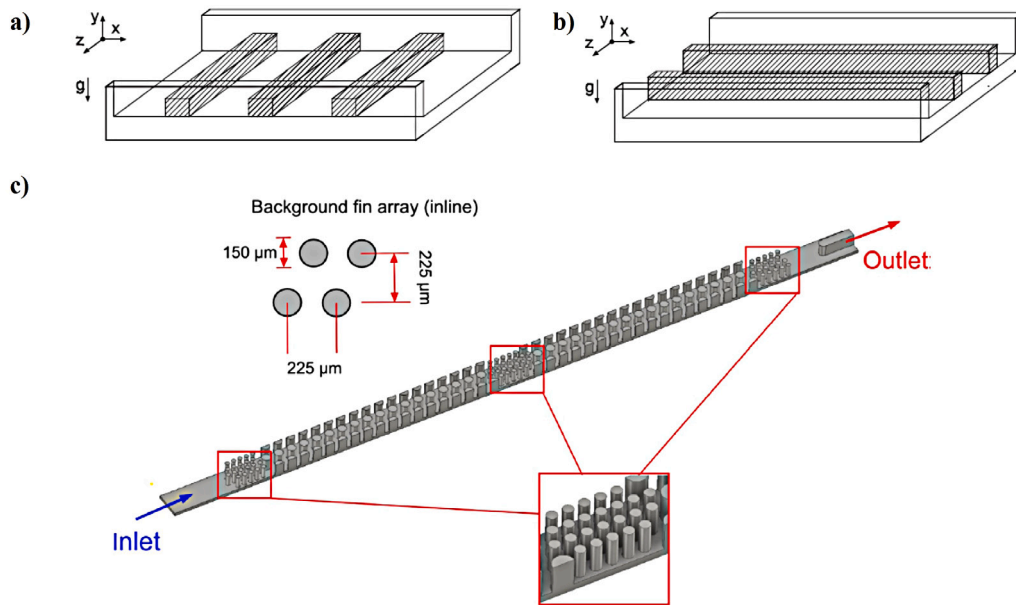


Fig. 23. Enhanced microchannels with (a) transverse fins (b) longitudinal fins [272]. (c) Microchannel with variable pin fin densities [275].

a uniform heat flux of 700 kW/m^2 was applied at the base. Enhancement in bubble nucleation due to increased heat transfer area in the case of microchannels with structures was observed which in turn resulted in lower microchannel wall temperature as compared to that of plain microchannels. With contact angle at 60° , enhancement in heat transfer of up to 62% was observed for channels with microfins compared to the smooth surface, while the enhancement for microcavities was only up to 17%. The enhancement in microfinned channels was attributed to a smaller/delayed dryout area and the improved convective heat transfer due to vortex formation in the presence of microfins. Further, they also observed that the increase in wettability led to a decrease in heat transfer performance in the case of plain and microcavity surfaces, whereas the effect of wettability was negligible for the surface with microfins.

Guo et al. [279] investigated the effect of providing random roughness on the microchannel surface. Random roughness on the surface was generated using the Fourier series method proposed by Lu et al. [280]. A microchannel of width $300 \mu\text{m}$, height $150 \mu\text{m}$ and length 4.5 mm was considered with water ($T_{\text{sat}} = 373.15 \text{ K}$) as fluid having inlet velocity ranging from 0.125 to 1 m/s . A uniform heat flux of 50 W/cm^2 was applied at the bottom surface. They observed an increase in the overall thermo-hydraulic performance of microchannel with random roughness as compared to that with a smooth surface. A maximum increase in performance factor (ratio of increase in heat transfer to increase in pressure drop) of up to 47% was reported, owing to reduced average wall temperatures because of improvement in convective heat transfer and bubble nucleation due to the presence of roughness elements. However, the advantage diminished at higher relative roughness because the bubbles remained trapped within the valleys, increasing the thermal resistance and leading to a reduction in heat transfer.

4.2. Enhanced wettability of boiling surfaces

Though heat transfer enhancement can be achieved by providing structures over the surface, the fabrication of microchannels with structures can be quite challenging. On the other hand, surface characteristics can also be modified by coating the surface with different materials, which can be done easily by employing any coating techniques without deforming the surface. The wettability of the surface affects the thermal fluid behaviour and can be easily controlled to enhance heat transfer performance by providing the necessary coating

over the surface. Hence numerical efforts have also been made to understand the heat transfer enhancement through modification in the wettability of the surface. Gong and Cheng [163] studied the effect of contact angle during flow boiling inside a microchannel by considering three different contact angles (57° , 96° , and 118°). LB method was used in their simulations and they were able to study the effect of contact angle on nucleation time and temperature. They reported that both nucleation time and temperature decreased with an increase in contact angle. Wi et al. [282] performed numerical simulations on surfaces with patterned wettability in which strips of hydrophobic and hydrophilic layers were arranged alternately. They performed simulations with different pattern ratios ($L_{\text{pho}}/L_{\text{phi}}$ where L_{pho} is length of hydrophobic strip and L_{phi} is length of hydrophilic strip) to study the effect of heterogeneous wettability on heat transfer performance. A contact angle of 123° was used for the hydrophobic area and 54° for the hydrophilic area. A higher heat transfer coefficient was observed on a surface that had a wider hydrophobic strip and a smaller hydrophilic strip arranged alternately (i.e. a hydrophobic surface with a higher pattern ratio). At certain pattern ratios, the heat transfer for the heterogeneous surfaces was observed to be higher than the uniform hydrophobic surface owing to a stable bubble nucleation-departure cycle. Although they were able to perform optimisation of heat transfer through a hydrophobic pattern, it is based only on a simple stripe pattern. Further investigation is required with different types of patterns and channel dimensions to get optimised results.

Kim and Lee [283] investigated the effect of varying the wettability of the surface on the flow boiling of a fluid inside a vertical microchannel of height $500 \mu\text{m}$, width $200 \mu\text{m}$, and length 30 mm . A constant heat flux of 350 kW/m^2 was applied at the base wall with different mass fluxes ranging from 20 – $500 \text{ kg/(m}^2\text{s)}$. Similar flow patterns were observed at different mass fluxes for boiling over hydrophilic and hydrophobic surfaces, namely, annular flow at $20 \text{ kg/(m}^2\text{s)}$, churn flow at $50 \text{ kg/(m}^2\text{s)}$, slug flow at $100 \text{ kg/(m}^2\text{s)}$ and bubbly flow for mass flux greater than $300 \text{ kg/(m}^2\text{s)}$. However, at higher mass fluxes, the bubble dynamics differed as bubbles were observed to lift off from the heated surface in the case of a hydrophilic channel, whereas the bubble slid along the hydrophobic surface. The critical heat flux increased with an increase in mass flux for both cases. For mass fluxes in the range 20 – $100 \text{ kg/(m}^2\text{s)}$, CHF was found to be lower for the hydrophobic case as compared to the hydrophilic case because the movement of bubbles was slower due to weak inertia, which promoted the coalescence of

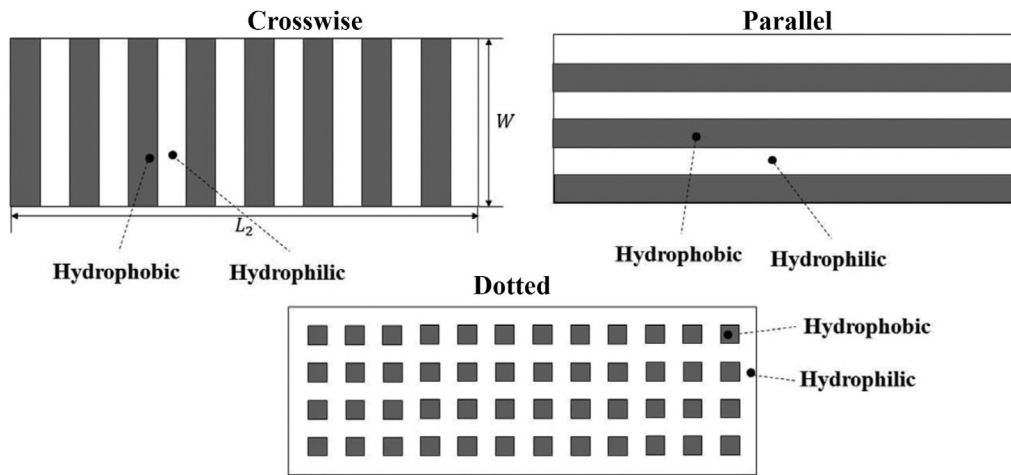


Fig. 24. Different wettability pattern shapes considered in the study of Kim et al. [281].

bubbles leading to a higher void fraction. This in turn led to a decrease in heat transfer between the wall and the fluid resulting in an increase in wall temperature. However, at higher mass fluxes, CHF was found to be higher for hydrophobic cases because the inertia was strong enough to reduce bubble coalescence and promote sliding of bubbles, leading to enhancement in heat transfer and to a reduction in wall temperature. They also studied flow boiling over a surface with heterogeneous wettability [281] using both experimental and numerical methods. They conducted a study with different wettability patterns, namely, crosswise, parallel, and dotted patterns, as shown in Fig. 24. A degradation in heat transfer performance was observed at a lower mass flux (below $500 \text{ kg}/(\text{m}^2\text{s})$) owing to delayed bubble movement and coalescence, while the performance increased at higher mass flux for all the patterns due to improvement in bubble mobility and detachment. The highest enhancement was observed in the case of the surfaces with dotted patterns with a hydrophobic area fraction of 0.32, as the nucleation site density was observed to be comparatively larger on dotted patterns.

Vontas et al. [284], using the VOF method, studied the effect of wettability on single and multiple bubble growth during flow boiling of ethanol inside a microchannel of width $150 \mu\text{m}$ and height $300 \mu\text{m}$. Three different values of heat flux ($20, 50, 100 \text{ kW}/\text{m}^2$) and mass flux ($74, 150, 295 \text{ kg}/(\text{m}^2\text{s})$) were considered in their study. Properties of stainless steel were used for the solid domain with three different combinations of advancing (θ_a) and receding (θ_r) contact angles for both hydrophilic ($\theta_a = 19^\circ, \theta_r = 8^\circ; \theta_a = 49^\circ, \theta_r = 0^\circ; \theta_a = 72^\circ, \theta_r = 40^\circ$) and hydrophobic ($\theta_a = 105^\circ, \theta_r = 95^\circ; \theta_a = 120^\circ, \theta_r = 80^\circ; \theta_a = 120^\circ, \theta_r = 115^\circ$) cases. They observed that the dominant mode of heat transfer was liquid film evaporation and contact line evaporation for hydrophilic and hydrophobic surfaces, respectively. Overall, with a single bubble, the hydrophilic surface performed slightly better at lower mass flux, while the performance of the hydrophobic surface was slightly better at higher mass flux. With multiple bubbles and multiple nucleation events, they reported an increase in Nusselt number up to 43.9% for hydrophilic surface and up to 17.85% for hydrophobic surface as compared to their respective single phase results. Tan et al. [285] explored the flow boiling of water inside a microtube of diameter $300 \mu\text{m}$, having either a hydrophilic surface (contact angle of 40°), or a hydrophobic surface (contact angle of 120°), or a surface with a wettability gradient where the contact angle decreased linearly from 120° to 40° . A constant heat flux of $15 \text{ W}/\text{cm}^2$ was applied on the wall and three different mass fluxes ($140 \text{ kg}/(\text{m}^2\text{s}), 280 \text{ kg}/(\text{m}^2\text{s}),$ and $560 \text{ kg}/(\text{m}^2\text{s})$) were considered. They observed that the heat transfer coefficient was higher for hydrophilic surfaces in subcooled and bubbly flow regions, because bubbles quickly detached from the surface whereas bubbles slid on the surface without detaching on the other surfaces. However, in

the slug flow regime, the heat transfer performances of all the surfaces considered were similar, since the bubble size reached the limit of the microtube size in all cases. The surface with a wettability gradient had a middle-level heat transfer coefficient in all the regions but achieved lower superheat than the others, especially in the regions where a slug flow pattern was established due to shorter bubbles.

Song et al. [286] performed 2-D simulations to understand flow boiling in microchannels having hybrid wettability surfaces using LBM. They performed simulations on a surface having hydrophilic-hydrophobic patterns arranged alternatively, with different sets of hydrophobic and hydrophilic contact angles. At first, they compared the performance of a hybrid wettability surface with that of a homogeneous wettability surface. Hybrid wettability surface offered advantages both in terms of higher heat transfer and lesser pressure drop fluctuations, as compared to the homogeneous hydrophobic surface. Further, in the case of the hybrid wettability surface, increasing the hydrophobic contact angle while keeping the hydrophilic contact angle constant, had the effect of increasing the heat flux up to a contact angle of 120° . Conversely, the heat flux increased with a decrease in hydrophilic contact angle when the hydrophobic contact angle was kept constant. The hybrid wettability surface with contact angles $30^\circ/120^\circ$ provided the best heat transfer performance, with an increase of up to 18.8% while the corresponding increase in pressure drop was only 12.7% compared to the hydrophilic surface.

From all these studies, it can be inferred that the surfaces with hybrid wettability can offer advantages both in terms of an increase in heat transfer performance and reduction in overall pressure drop. However, a systematic investigation of different parameters such as contact angles, pattern shapes, channel hydraulic diameter or wall thickness, is necessary to obtain an optimised surface.

4.3. Enhanced geometry

In parallel channels, the bubble nucleation inside the channels is both temporally and spatially random, and researchers have observed maldistribution in fluid flow which in turn results in flow reversal [268]. The reversed flow condition causes deterioration in heat transfer and also leads to early CHF conditions. Kandlikar et al. [271] showed that the instability in boiling can be reduced by introducing pressure drop elements at the inlet. Following this, Mukherjee and Kandlikar [287] performed numerical simulations of flow boiling inside a square microchannel of hydraulic diameter $198 \mu\text{m}$ with a restricted inlet to understand the changes in the bubble dynamics due to the presence of restrictions at the inlet. Simulations were performed with three different inlet-to-outlet area ratios which were 1, 0.5, and 0.04. Water at 100°C with a mass flux of $20 \text{ kg}/(\text{m}^2\text{s})$ was considered and

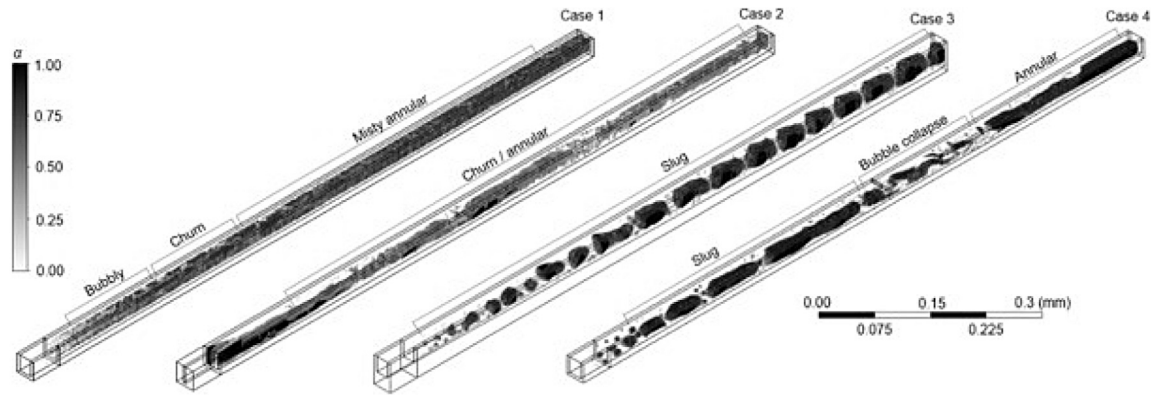


Fig. 25. Comparison of flow patterns in a straight channel, a channel with a restriction at the inlet, a diverging channel, and a channel with vapour venting [191].

the wall surface was maintained at a constant temperature of 112°C . They observed an increase in the thickness of the liquid film between the top of the bubble and the channel wall due to an increase in fluid velocity with a decreasing restriction ratio, which in turn suppressed the thin film evaporation around the bubbles. Hence, the growth rate of the bubble decreased with decreasing inlet-to-outlet area ratio. This mitigated the risk of flow reversal as the bubble no longer blocks the channel cross-section. They also suggested that flow reversal might be reduced by having a microchannel in which the area of the channel continuously increases from inlet to outlet. However, it should be noted that these observations were based on simulations with low mass flux, whereas at higher mass fluxes, the dynamics of the flow instabilities may change substantially owing to the flow field becoming asymmetric [288], which has an impact on the bubble growth evolution. Alugoju et al. [289] expanded on this idea and conducted a 2-D numerical simulation of flow boiling inside a diverging microchannel using the VOF method with the Lee model for handling phase change. A microchannel with an inlet width of $200\ \mu\text{m}$ and different diverging angles ranging from $0\text{--}8^{\circ}$ were considered in their study. They observed an increase in heat transfer performance and bubble nucleation only for diverging microchannels with a diverging angle of 2° , as they observed flow reversal resulting in a reduction in performance for higher diverging angles.

Lin et al. [290] performed numerical simulations in 3-D to study the dynamics of a vapour slug in a diverging microchannel. They considered a microchannel with a height and inlet width of $200\ \mu\text{m}$ but varied the outlet width of the channel to model a diverging microchannel. The outlet widths considered in their study were $256\ \mu\text{m}$, $312\ \mu\text{m}$ and $368\ \mu\text{m}$ corresponding to diverging angles of 0.57° , 1.15° and 1.72° , respectively. R113 refrigerant at a saturation temperature of $323.15\ \text{K}$ was considered as the fluid with two different mass fluxes (500 and $1000\ \text{kg}/(\text{m}^2\text{s})$). Constant heat fluxes of 10 , 20 , and $50\ \text{kW}/\text{m}^2$ were applied on all the walls of the heated section. The velocity of the flow was observed to be higher at both upstream and downstream the bubble in the diverging channel and the bubble was propelled to move towards the outlet. Moreover, because of the expanding area in the cross-section, the bubble had more freedom to expand in the cross-stream direction while growing in the flow direction. This helped avoid complete clogging of the channel. These two factors contributed to reduced boiling instabilities compared to a straight microchannel. The advantage in terms of boiling instability was prominent mainly at lower mass flux and higher heat flux. However, the heat transfer coefficient was observed to decrease with increasing diverging angles due to an increase in liquid film thickness.

Broughton and Joshi [191] compared the flow boiling heat transfer characteristics of a straight microchannel, an inlet-restricted microchannel, an expanding microchannel, and a microchannel with auxiliary jetting. The width and height of the straight microchannel were $200\ \mu\text{m}$ and $250\ \mu\text{m}$. The channel dimension was kept the same for the

inlet-restricted microchannel with only the width at the inlet changed to $40\ \mu\text{m}$. For the diverging channel the dimension at the inlet was similar to the straight microchannel, but the height at the outlet was changed to $424\ \mu\text{m}$ accounting for an expansion angle of 1° . The dimensions of the channel with auxiliary jetting were also similar to a straight microchannel with a secondary inlet of width $20\ \mu\text{m}$ provided at the centre of the channel length for the auxiliary jet. A constant heat flux of $200\ \text{W}/\text{cm}^2$ was applied at the bottom wall with water ($T_{\text{sat}} = 100^{\circ}\text{C}$) as fluid at the inlet having mass flux of $1000\ \text{kg}/(\text{m}^2\text{s})$. Fig. 25 shows the flow patterns in the different configurations of microchannels considered in their study. They observed that the prevailing flow pattern inside the straight and the microchannel with inlet restrictions was essentially churn/annular flow, while in the diverging channel this was a confined slug flow. In the case of the microchannel with an auxiliary vent, the flow pattern was slug flow before the vent. Near the vent, they observed a region of collapsing bubbles because of the jet from the vent. Near the outlet, the flow pattern was found to be annular. The best heat transfer characteristics were observed for a diverging microchannel, with a higher enhancement in heat transfer coefficient and reduced pressure drop compared to the other configurations.

Numerical simulations have also been conducted with wavy microchannels as researchers have experimentally observed that wavy microchannels may provide an augmented heat transfer coefficient along with prevention of dryout and delay CHF condition [291]. Tiwari and Moharana [194] did a numerical study on a wavy microchannel by considering conjugate heat transfer effects. In their study, a microchannel with a width of $0.6\ \text{mm}$ and height of $0.9\ \text{mm}$ was considered and a comparison of flow boiling inside wavy microchannels with waviness (γ) ranging from 0 to 0.267 (with $\gamma = 0$ representing a straight microchannel) was made. Here waviness was defined as $\gamma = A/\lambda$, where A is the amplitude and λ is the wavelength of the wave shape considered for the channels. Water at sub-atmospheric pressure and $300\ \text{K}$ was considered as a fluid at the inlet with two different mass fluxes ($G = 118$ and $590\ \text{kg}/(\text{m}^2\text{s})$), while a constant heat flux of $300\ \text{kW}/\text{m}^2$ was applied at the bottom of the wall. It can be observed from Fig. 26(a) that the size of the bubbles formed is relatively smaller inside channels with higher waviness (for $\gamma = 0.133$ to 0.267). Hence, at higher waviness, clogging of the flow area by the bubbles is reduced resulting in a reduction in boiling instability. It can also be observed from Fig. 26(a) that wall temperatures are comparatively lower for channels with higher waviness, because of which their heat transfer coefficient values were found to be higher. Further, they also reported that, for both the straight and wavy microchannels, an increase in wall thickness could lead to a reduction in instability in boiling. A similar effect of the waviness of the channel on flow boiling was reported by Bhuva et al. [292] who conducted investigations on a raccoon microchannel. In raccoon microchannels, the crests of the wave on one side of the channel wall face the troughs of the wave on the other side (as seen in Fig. 26(b)), and hence they differ from wavy microchannels where the

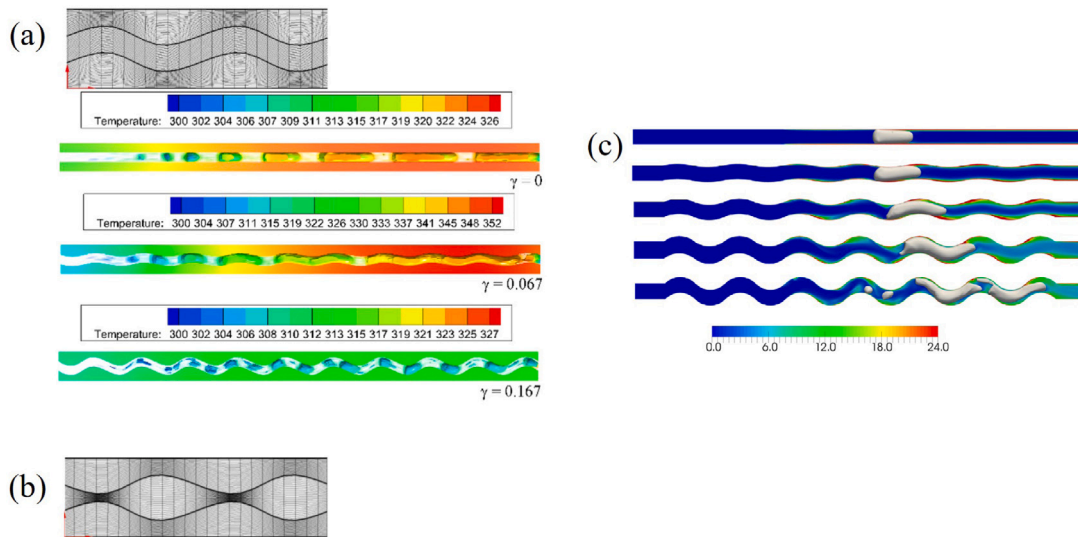


Fig. 26. (a) Bubble pattern variation with time in a wavy microchannel [194]. (b) Image of a raccoon microchannel [292]. (c) Evolution of an elongated vapour bubble in a wavy channel [293].

waves on either side of the channel wall runs parallel to each other (as seen in Fig. 26(a)). The channel dimension and the boundary conditions considered were similar to those considered by Tiwari and Moharana [194]. They also reported a reduction in instability and enhancement in heat transfer for waviness in the range of 0.134 to 0.267. Odumosu et al. [293] compared the growth of an elongated vapour slug inside square channels of 1 mm side with different waviness ranging from 0 to 0.1. R134a at $T_{\text{sat}} = 30^\circ\text{C}$ was considered with the mass flux of $308 \text{ kg}/(\text{m}^2\text{s})$ and a constant heat flux of $90 \text{ kW}/\text{m}^2$ was applied at the wall. It can be observed from Fig. 26(c) that with an increase in waviness, the bubble growth increased due to its deformation in the wavy channel. Heat transfer performance of the wavy channels also increased due to the perturbation of the bubble, and a maximum increase in the Nusselt number up to 2.6 times compared to straight microchannels was reported. Conjugate heat transfer was not included in this study. All the studies on modified geometry presented above were obtained with simulations of a single channel and hence we can only see advantages in terms of controlled bubble growth rate or reduced variation in wall temperature. The advantages or disadvantages in terms of reduction in flow maldistribution cannot be observed with a simulation on single channel, but can only be observed in a multichannel setup with at least a few interconnected parallel microchannels.

Few attempts have been made to mitigate flow boiling instability inside a multi-channel evaporator setup. Prajapati et al. [219] conducted both experimental and 2-D numerical analyses of microchannels with segmented fins in which along with the primary channel in the flow direction, the secondary channels were cut at an angle of 30° with respect to the primary channel. Both the primary and secondary channels were of width 0.4 mm. They observed that as the bubble grew inside the channel, it interacted with the segmented fin such that the bubble could elongate freely in both primary and secondary channels. This prevented blockage of the primary channel as the bubble did not completely expand in the primary channel itself, which mitigated flow reversal. They also reported faster nucleation, higher bubble growth rate, and early bubble detachment for the microchannels with segmented fins. Qiu et al. [294] compared the flow boiling performance of a rectangular multichannel heat sink (RMHS) with that of a cobweb-shaped microchannel heat sink (CMHS) using the VOF method with the Lee model [89] for phase change. A cobweb-shaped microchannel was first developed by Tan et al. [295] inspired by natural structures such as spider web and is composed of a set of concentric hexagon structures, as illustrated in Fig. 27(a). Qiu et al. [294] modified this shape further and considered two types of CMHS in their study, one with horizontal inlet

and outlet (CMHS-H) wherein horizontal channels were added on the four edges of the hexagon, and the other with inclined inlet and outlet (CMHS-I) in which 45° inclined channels were added on four edges of hexagon. The length and the width of the heat sink were 9.93 mm and 9.5 mm, respectively, while each channel had a width and height of 0.5 mm. Water at atmospheric pressure and inlet temperature of 300 K was used as fluid, with mass fluxes of 149.4, 199.2, $248.5 \text{ kg}/(\text{m}^2\text{s})$. A constant heat flux (ranging from $75\text{--}125 \text{ W}/\text{cm}^2$) was applied at the bottom of the heat sink. From Fig. 27(a), it can be observed that in the case of cobweb-shaped microchannels (both CMHS) bubbles nucleated majorly in the secondary channels due to their higher wall superheat, triggered by reduced flow velocities. Further, comparatively lesser bubble clogging, stable flow boiling, lower wall temperatures, and better heat transfer characteristics were observed in the case of CMHS-H as compared to the other heat sinks considered in their study.

Premature critical heat flux due to intermittent dryout or flow instabilities is one of the major problems associated with two-phase cooling in a microchannel. Bergles and Kandlikar [296] have suggested that CHF can be delayed or increased either by increasing wetted area, mass flux, and channel diameter or by reducing channel length. One of the methods employed to reduce the effective length of a microchannel heat sink is to place an array of dividers over the microchannel heat sink [297]. Microchannels with such a design are called manifold microchannels. Experimental observations of flow boiling in manifold microchannels revealed that reduction in pressure drop, uniformity in flow and heat transfer could be achieved by employing manifold microchannels owing to the reduced effective flow length of the device [298,299]. Numerical studies on flow boiling of HFE-7100 ($T_{\text{sat}} = 339 \text{ K}$) inside manifold microchannels have been performed by Luo and Li [300]. They compared the applicability of two phase change models, namely, the Lee model and the interface heat resistance models. No microlayer model was included in their study since no experimental data of liquid film thickness between the bubble and solid wall was available for HFE-7100. Because of this, early contact between vapour and the solid wall was observed, which led to underestimation of the heat transfer coefficient and thus overprediction in the average temperature in the domain for both the phase change models. The predicted temperature value by the interface heat transfer model was found to be slightly closer to the experimental results, within an error band of -5 to $+10\%$ as compared to the Lee model in which the error band was -5 to 20% . Luo et al. [301] further extended this study and compared the performance of manifold microchannels with different manifold arrangements. The microchannel heat sink they considered included 10

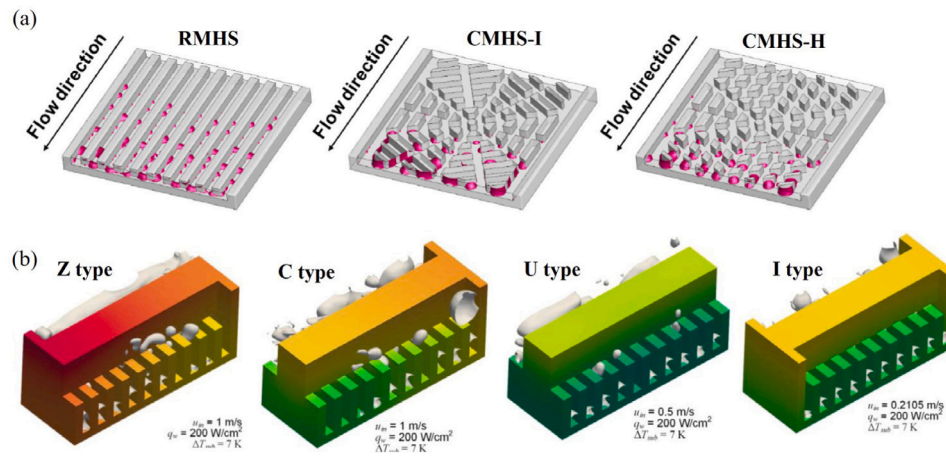


Fig. 27. (a) Comparison of flow boiling in rectangular and cobweb shaped microchannel heat sinks [294]. (b) Comparison of flow boiling in microchannels with different manifold arrangements [301].

microchannels of width $50 \mu\text{m}$ and height $100 \mu\text{m}$ having a total length of $400 \mu\text{m}$, with a divider of $200 \mu\text{m}$ placed at the centre of the heat sink to separate the inlet and the outlet. The shape of the divider varied according to the type of manifold arrangements considered which were, namely, Z-type, C-type, H-type, and U-type manifold arrangements (configurations shown in Fig. 27(b)). They observed that in both H-type and U-type manifold arrangements, the distribution of mass flux in each channel was quite uniform, which helped the bubbles formed in the channels to easily exit the heat sink. This turn resulted in better temperature uniformity for these two arrangements compared to other types. They also observed better heat transfer with lower pressure drop for both microchannels with H-type and U-type manifold arrangements, owing to stable boiling and uniform mass flux distribution.

4.4. Summary and challenges

In summary, many heat transfer enhancement methods for flow boiling in microchannels have been investigated via numerical simulations in recent years, from micro-structured surfaces to several wettability patterns and different levels of complexity of heat sink geometries. However, these have often been isolated efforts, with limited systematic analyses aimed to explore the whole parameters space, and thus deliver an optimal solution.

The majority of the studies related to understanding and reducing instability in boiling using numerical simulations in the literature have mainly considered simulations with a single channel. However, a microchannel heat exchanger always contains multiple channels with common manifolds and hence in order to model and understand the resulting flow distribution and potential backflow issues, multi-channel configurations should be modelled, with efficient adaptive meshing techniques constituting a key enabler for this.

Hybrid enhancement methods, wherein the merits of different enhancement methods are combined to further enhance the heat transfer characteristics or improve stability in boiling, have been gaining popularity. Experimental efforts have shown improvement in heat transfer characteristics and boiling stability by combining pressure drop elements such as inlet restriction with nucleation sites [271], pin fins with re-entrant channels [302], pin fins with porous walls [303,304]. Studies on such hybrid enhancement methods have not been explored numerically with sufficient depth and should be investigated in the future.

Additive Manufacturing offers nowadays unlimited degrees of freedom in the design of heat exchangers, and optimisation of the heat transfer solutions is becoming a crucial aspect in design. Numerical simulations can become an even more valuable tool to explore a large number of solutions than what is possible with experiments,

thus creating a database useful for optimisation techniques or machine learning algorithms. For example, Kametani et al. [305] combined adjoint-based shape optimisation with a single-phase heat and fluid flow solver to find the shape of pin fins that maximise heat transfer while limiting pressure drop in a heat exchanger; in their method, the shape of prescribed boundaries (the pin fins) becomes an unknown that is obtained upon the solution of the adjoint equations, deriving from a variational formulation of the Navier–Stokes equations. Topology optimisation with numerical simulations was also employed by Ozguc et al. [306] to optimise the geometry of a single-phase microchannel heat sink subject to non-uniform heating, the optimal configuration of which was then manufactured via AM and tested experimentally. A machine-learning method based on genetic algorithms applied to the results of numerical simulations was proposed by Moon et al. [307] to optimise additively manufactured single-phase heat sinks. Hence, optimisation algorithms combined with numerical simulations are being used increasingly frequently in single-phase heat transfer, although to the authors' knowledge only Weibel et al. [308] have so far successfully attempted to extend these to boiling heat transfer and two-phase simulations. Therefore, the combination of numerical simulations, optimisation algorithms and additive manufacturing is expected to become a very active research topic over the next years, as a crucial step towards delivering enhanced miniaturised evaporators capable of dissipating the record-high heat loads generated by next-generation microprocessors.

5. Current status, challenges and future direction

Numerical simulations have achieved significant milestones in the past decade towards the fundamental understanding of flow boiling in microchannels, and have been successfully used to investigate and propose novel heat transfer enhancement strategies for compact heat sinks. Two-phase interface capturing methods such as VOF and LS have emerged as robust and reliable techniques to overcome some of the difficulties intrinsic to the simulation of microscale flows [22,118], with Phase Field and Lattice-Boltzmann methods showing great potential to incorporate interfacial mass transfer phenomena in a thermodynamically consistent manner [112,140]. The majority of the studies reviewed in this article have employed commercial simulation software (mostly ANSYS and COMSOL) which offer a robust framework and flexibility to complex geometries and meshes, however, open-source software such as OpenFOAM has been increasingly used and a number of public Github repositories have been released in recent years for high-fidelity two-phase simulations [178,211].

There remain several challenges that must drive the future direction in simulation technology, building upon stronger links between simulations and experiments to perfect the 'handshake' of experimental setups

and numerical models. The following recommendations for numerical simulations stem from the present review:

- Surface tension remains a weakness in the most widely used Volume Of Fluid method; novel, accurate algorithms exist, but these are still infrequently employed in microchannel simulations, as such modellers should focus on improving the reliability of simulations of complex flow patterns and heat sink geometries.
- Despite the fact that sub-grid thin-film models are well established in pool boiling simulations, there is a lack of validated models for films developing around confined bubbles, which are needed for an accurate representation of key phenomena such as liquid film dewetting and dryout.
- Bubble nucleation is still artificially prescribed; development of physics-based nucleation models are necessary, possibly incorporating surface topography information and validated against experimental data.
- Adaptive mesh refinement in both fluid and solid regions is an essential algorithmic development to resolve heat transfer in thin liquid films, while maintaining an affordable computational overhead.
- Only very few computational studies have tackled flow boiling instabilities, which are one of the main issues in microchannel flow boiling. Researchers should increase their efforts towards modelling of multiple parallel channels with common inlet/outlet manifolds.
- The combination of numerical simulations with optimisation and machine learning algorithms represents the most exciting future perspective for simulations to guide the thermal design of future heat transfer elements, however, these techniques have not yet been widely exploited for two-phase flows.

Since numerical simulations require experimental observation and data for model development and validation, the following wish-list is proposed:

- Most of the experimental studies in microchannel flow boiling aimed at characterising the time- and spatially-averaged thermal hydraulic performances of multichannel evaporators. More fundamental studies dedicated to single channels, finely-resolved temperature maps and liquid film thickness measurements are welcome for the purpose of model validation.
- Experimental flow boiling setups are often very difficult to reproduce by numerical simulations; experimentalists and modellers should collaborate on the design of fundamental experiments whose initial and boundary conditions can be emulated by simulations.
- Temperature and pressure measurements in experiments are not usually taken within the channels and the final values of friction factors and heat transfer coefficients published depend significantly on the data reduction procedure. An accurate analysis of the uncertainty deriving from the assumptions and correlations utilised in data reduction is currently missing and this hinders a fair comparison of numerical and experimental results.
- Mesoscale and molecular models for simulations would benefit from the availability of topography maps of boiling surfaces alongside nucleation data in an attempt to capture nucleation over 'real' surfaces from first principles.

6. Conclusions

This article presented a comprehensive review of the vast literature of scientific papers dedicated to numerical simulations of boiling in microchannels. Flows within microchannels possess distinctive features such as clear separation of liquid and gas phases, very thin liquid films, dominance of surface tension forces, large Laplace pressures, and interfacial resistance to mass transfer, that make them differ significantly

from boiling flows in unconfined spaces and require tailored numerical methods to achieve accurate simulations. The most recent advances in traditional and emerging computational techniques for interface-resolved simulations were reviewed, spanning from macroscale models based on the solution of the continuum Navier–Stokes equations, to mesoscale and molecular dynamics models. The review then encompassed literature studies that investigated, via simulations, prevailing fluid dynamics features in microchannel flow boiling, such as the confined bubble dynamics, flow pattern development, conjugate heat transfer and flow instabilities deriving from multi-channel configurations. Lastly, the results of computational studies dedicated to heat transfer enhancement through engineered surfaces and novel geometrical arrangements were illustrated. The remaining challenges and future directions for research in microchannel flow boiling stemming from the present review were summarised in Section 5, alongside recommendations for future computational research and a wish-list for experimental work aimed at improving and validating numerical algorithms.

Accurate estimation of surface tension, availability of sub-grid thin film models applicable to flow boiling conditions, physics-based modelling of nucleation, and adaptive mesh refinement remain the major challenges to achieving reliable numerical simulations of boiling in microchannels, and thus significant algorithmic developments are required to overcome these difficulties. Furthermore, replicating experimental microchannel flow boiling conditions remains a formidable challenge for simulations. A closer collaboration between experimentalists and modellers would be greatly beneficial to tailor the design of fundamental experiments whose initial and boundary conditions can be replicated faithfully by simulations. As future directions for numerical modelling of boiling in microchannels, an increased use and integration of mesoscale models, such as Lattice Boltzmann and phase field methods, is recommended to incorporate bubble nucleation and other interfacial effects from first principles within simulations, as well as the development of coupling strategies for multiphase fluid dynamics solvers with machine learning and optimisation algorithms, to drive the design of miniaturised heat transfer elements.

Declaration of competing interest

The authors declare that they have no known competing financial interests or personal relationships that could have appeared to influence the work reported in this paper.

Data availability

No data was used for the research described in the article.

Acknowledgements

This work was supported by the UK Engineering and Physical Sciences Research Council (EPSRC) through the BONSAI project (grant numbers EP/T033398/1, and EP/T03338X/1).

References

- [1] T.G. Karayiannis, M.M. Mahmoud, Flow boiling in microchannels: fundamentals and applications, *Appl. Therm. Eng.* 115 (2017) 1372–1397.
- [2] I. Mudawar, Two-phase microchannel heat sinks: theory, applications, and limitations, *J. Electron. Packag.* 133 (2011) 041002.
- [3] J.R. Thome, A. Cioncolini, Chapter four - flow boiling in microchannels, in: *Advances in Heat Transfer*, Vol. 49, 2017, pp. 157–224.
- [4] S.G. Kandlikar, Review and projections of integrated cooling systems for three-dimensional integrated circuits, *J. Electron. Packag.* 136 (2014) 024001.
- [5] N. Gilmore, V. Timchenko, C. Menictas, Microchannel cooling of concentrator photovoltaics: A review, *Renew. Sustain. Energy Rev.* 90 (2018) 1041–1059, <http://dx.doi.org/10.1016/j.rser.2018.04.010>.
- [6] J. Lee, I. Mudawar, Low-temperature two-phase microchannel cooling for high-heat-flux thermal management of defense electronics, *IEEE Trans. Compon. Packag. Technol.* 32 (2) (2009) 453–465, <http://dx.doi.org/10.1109/TCAPT.2008.2005783>.

- [7] M. Pedram, S. Nazarian, Thermal modeling, analysis, and management in VLSI circuits: Principles and methods, *Proc. IEEE* 94 (8) (2006) 1487–1501, <http://dx.doi.org/10.1109/JPROC.2006.879797>.
- [8] Z. He, Y. Yan, Z. Zhang, Thermal management and temperature uniformity enhancement of electronic devices by micro heat sinks: A review, *Energy* 216 (2021) <http://dx.doi.org/10.1016/j.energy.2020.119223>.
- [9] S.G. Kandlikar, A.V. Bapat, Evaluation of jet impingement, spray and microchannel chip cooling options for high heat flux removal, *Heat Transf. Eng.* 28 (11) (2007) 911–923, <http://dx.doi.org/10.1080/01457630701421703>.
- [10] A.C. Cotler, E.R. Brown, V. Dhir, M.C. Shaw, Chip-level spray cooling of an LD-MOSFET RF power amplifier+, *IEEE Trans. Compon. Packag. Technol.* 27 (2) (2004) 411–416, <http://dx.doi.org/10.1109/TCAPT.2004.828550>.
- [11] C.J. Chang, H.T. Chen, C. Gau, Flow and heat transfer of a microjet impinging on a heated chip: Part II - heat transfer, *Nanoscale Microscale Thermophys. Eng.* 17 (2) (2013) 92–111, <http://dx.doi.org/10.1080/15567265.2012.761304>.
- [12] D. Deng, L. Zeng, W. Sun, A review on flow boiling enhancement and fabrication of enhanced microchannels of microchannel heat sinks, *Int. J. Heat Mass Transfer* 175 (2021) <http://dx.doi.org/10.1016/j.ijheatmasstransfer.2021.121332>.
- [13] P. Cheng, G. Wang, X. Quan, Recent work on boiling and condensation in microchannels, *J. Heat Transfer* 131 (4) (2009) 1–15, <http://dx.doi.org/10.1115/1.3072906>.
- [14] M. Asadi, G. Xie, B. Sundén, A review of heat transfer and pressure drop characteristics of single and two-phase microchannels, *Int. J. Heat Mass Transfer* 79 (2014) 34–53, <http://dx.doi.org/10.1016/j.ijheatmasstransfer.2014.07.090>.
- [15] T.G. Karayiannis, M.M. Mahmoud, Flow boiling in microchannels: Fundamentals and applications, *Appl. Therm. Eng.* 115 (2017) 1372–1397, <http://dx.doi.org/10.1016/j.applthermaleng.2016.08.063>.
- [16] L. Cheng, G. Xia, Fundamental issues, mechanisms and models of flow boiling heat transfer in microscale channels, *Int. J. Heat Mass Transfer* 108 (2017) 97–127, <http://dx.doi.org/10.1016/j.ijheatmasstransfer.2016.12.003>.
- [17] N.A.C. Sidik, M.N.A.W. Muhamad, W.M.A.A. Japar, Z.A. Rasid, An overview of passive techniques for heat transfer augmentation in microchannel heat sink, *Int. Commun. Heat Mass Transfer* 88 (2017) 74–83, <http://dx.doi.org/10.1016/j.icheatmasstransfer.2017.08.009>.
- [18] S. Xie, M. Shahmohammadi Beni, J. Cai, J. Zhao, Review of critical-heat-flux enhancement methods, *Int. J. Heat Mass Transfer* 122 (2018) 275–289, <http://dx.doi.org/10.1016/j.ijheatmasstransfer.2018.01.116>.
- [19] G. Liang, I. Mudawar, Review of channel flow boiling enhancement by surface modification, and instability suppression schemes, *Int. J. Heat Mass Transfer* 146 (2020) <http://dx.doi.org/10.1016/j.ijheatmasstransfer.2019.118864>.
- [20] J.R. Thome, V. Dupont, A.M. Jabobi, Heat transfer model for evaporation in microchannels. part I: presentation of the model, *Int. J. Heat Mass Transfer* 47 (2004) 3375–3385.
- [21] A. Cioncolini, J.R. Thome, Entrained liquid fraction prediction in adiabatic and evaporating annular two-phase flow, *Nucl. Eng. Des.* 243 (2012) 200–213.
- [22] M. Magnini, B. Pulvirenti, J.R. Thome, Numerical investigation of hydrodynamics and heat transfer of elongated bubbles during flow boiling in a microchannel, *Int. J. Heat Mass Transfer* 59 (2013) 451–471.
- [23] M. Magnini, J.R. Thome, A CFD study of the parameters influencing heat transfer in microchannel slug flow boiling, *Int. J. Therm. Sci.* 110 (2016) 119–136.
- [24] Z. Guo, D.F. Fletcher, B.S. Haynes, Numerical simulation of annular flow hydrodynamics in microchannels, *Comput. & Fluids* 133 (2016) 90–102, <http://dx.doi.org/10.1016/j.compfluid.2016.04.017>.
- [25] M. Ilic, M.M. Petrovic, V.D. Stevanovic, Boiling heat transfer modelling: A review and future prospectus, *Therm. Sci.* 23 (2019) 87–107, <http://dx.doi.org/10.2298/TSCI1807252491>.
- [26] Y. Lin, Y. Luo, E.N. Wang, W. Li, W.J. Minkowycz, Enhancement of flow boiling heat transfer in microchannel using micro-fin and micro-cavity surfaces, *Int. J. Heat Mass Transfer* 179 (2021) <http://dx.doi.org/10.1016/j.ijheatmasstransfer.2021.121739>.
- [27] Z. Guo, D.F. Fletcher, B.S. Haynes, A review of computational modelling of flow boiling in microchannels, *J. Comput. Multiph. Flow* 6 (2) (2014) 79–110.
- [28] S. Szczukiewicz, M. Magnini, J.R. Thome, Proposed models, ongoing experiments, and latest numerical simulations of microchannel two-phase flow boiling, *Int. J. Multiph. Flow* 59 (2014) 84–101, <http://dx.doi.org/10.1016/j.ijmultiphaseflow.2013.10.014>.
- [29] C.R. Kharangate, I. Mudawar, Review of computational studies on boiling and condensation, *Int. J. Heat Mass Transfer* 108 (2017) 1164–1196.
- [30] R.C. Lee, J.E. Nydahl, Numerical calculation of bubble growth in nucleate boiling from inception through departure, *J. Heat Transfer* 111 (2) (1989) 474–479.
- [31] S.W.J. Welch, J. Wilson, A volume of fluid based method for fluid flows with phase change, *J. Comput. Phys.* 160 (2000) 662–682.
- [32] S. Mehendale, A. Jacob, R. Shah, Fluid flow and heat transfer at micro-and meso-scales with application to heat exchanger design, *Appl. Mech. Rev.* 53 (2000) 175–193, URL: http://asmedigitalcollection.asme.org/appliedmechanicsreviews/article-pdf/53/7/175/5438045/175_1.pdf?casa_token=qGtHio1CSTAAAAAA:U5JWVGNIBq6gH9RUBsRzh9DZP-g9UNn9kVFa8DTV37WrihVq86Eh9fBPHXJqbWqOuC9yQ.
- [33] S.G. Kandlikar, W.J. Grande, Evolution of microchannel flow passages-thermohydraulic performance and fabrication technology, *Heat Transf. Eng.* 24 (1) (2003) 3–17, <http://dx.doi.org/10.1080/0145763030404040>.
- [34] P.A. Kew, K. Cornwell, Correlations for the prediction of boiling heat transfer in small diameter channels, *Appl. Therm. Eng.* 17 (1997) 705–715.
- [35] G. Tryggvason, R. Scardovelli, S. Zaleski, *Direct Numerical Simulations of Gas-Liquid Multiphase Flows*, Cambridge University Press, Cambridge, 2011.
- [36] M.Z. Podowski, R.M. Podowski, Mechanistic multidimensional modeling of forced convection boiling heat transfer, *Sci. Technol. Nucl. Install.* (2008).
- [37] A. Ferrari, M. Magnini, J.R. Thome, A flexible coupled level set and volume of fluid (flexCLV) method to simulate microscale two-phase flow in non-uniform and unstructured meshes, *Int. J. Multiph. Flow* 91 (2017) 276–295.
- [38] V.S. Ajaev, G.M. Homsy, Three-dimensional steady vapor bubbles in rectangular microchannels, *J. Colloids Interface Sci.* 244 (2001) 180–189.
- [39] D. Juric, G. Tryggvason, Computations of boiling flows, *Int. J. Multiph. Flow* 24 (1998) 387–410.
- [40] S. Hardt, F. Wondra, Evaporation model for interfacial flows based on a continuum-field representation of the source terms, *J. Comput. Phys.* 227 (2008) 5871–5895.
- [41] R. Scardovelli, S. Zaleski, Direct numerical simulation of free-surface and interfacial flow, *Annu. Rev. Fluid Mech.* 31 (1999) 567–603.
- [42] C.W. Hirt, B.D. Nichols, Volume of fluid (VOF) method for the dynamics of free boundaries, *J. Comput. Phys.* 39 (1981) 201–225.
- [43] M. Sussman, P. Smereka, S. Osher, A level set approach for computing solutions to incompressible two-phase flow, *J. Comput. Phys.* 114 (1994) 146–159.
- [44] S.O. Unverdi, G. Tryggvason, A front-tracking method for viscous, incompressible, multi-fluid flows, *J. Comput. Phys.* 100 (1992) 25–37.
- [45] J.U. Brackbill, D.B. Kothe, C. Zemach, A continuum method for modeling surface tension, *J. Comput. Phys.* 100 (1992) 335–354.
- [46] R.P. Fedkiw, T. Aslam, B. Merriman, S. Osher, A non-oscillatory Eulerian approach to interfaces in multimaterial flows (the ghost fluid method), *J. Comput. Phys.* 152 (1999) 457–492.
- [47] F. Gibou, R. Fedkiw, S. Osher, A review of level-set methods and some recent applications, *J. Comput. Phys.* 353 (2018) 82–109.
- [48] L. Anumolu, M. Trujillo, Gradient augmented level set method for phase change simulations, *J. Comput. Phys.* 353 (2018) 377–406.
- [49] C. Kunkelmann, P. Stephan, CFD simulation of boiling flows using the volume-of-fluid method within openFOAM, *Numer. Heat Transfer A* 56 (2009) 631–646.
- [50] L.C. Malan, A.G. Malan, S. Zaleski, P.G. Rousseau, A geometric VOF method for interface resolved phase change and conservative thermal energy advection, *J. Comput. Phys.* 426 (2021) 109920, <http://dx.doi.org/10.1016/j.jcp.2020.109920>.
- [51] D.L. Youngs, Time-dependent multi-material flow with large fluid distortion, in: K.W. Morton, M.J. Baines (Eds.), *Numerical Methods for Fluid Dynamics*, Academic Press, 1982, pp. 273–285.
- [52] M. Rudman, Volume tracking methods for interfacial flows calculations, *Internat. J. Numer. Methods Fluids* 24 (1997) 671–691.
- [53] O. Ubbink, R.I. Issa, A method for capturing sharp fluid interfaces on arbitrary meshes, *J. Comput. Phys.* 153 (1999) 26–50.
- [54] F. Denner, B.G.M. van Wachem, Compressive VOF method with skewness correction to capture sharp interfaces on arbitrary meshes, *J. Comput. Phys.* 279 (2014) 127–144.
- [55] Y. Sato, B. Niceno, A conservative local interface sharpening scheme for the constrained interpolation profile method, *Internat. J. Numer. Methods Fluids* 70 (2012) 441–467.
- [56] D. Fuster, T. Arrufat, M. Cialesi-Espósito, Y. Ling, L. Malan, S. Pal, R. Scardovelli, G. Tryggvason, S. Zaleski, A momentum-conserving, consistent, volume-of-fluid method for incompressible flow on staggered grids, 2018, arXiv, <https://arxiv.org/abs/1811.12327v1>.
- [57] G. Son, V.K. Dhir, Numerical simulation of film boiling near critical pressures with a level set method, *J. Heat Mass Transfer* 120 (1998) 183–192.
- [58] G. Son, V.K. Dhir, A level set method for analysis of film boiling on an immersed solid surface, *Numer. Heat Transfer B* 52 (2007) 153–177.
- [59] S. Tanguy, M. Sagan, B. Lanalle, F. Couderc, C. Colin, Benchmarks and numerical methods for the simulation of boiling flows, *J. Comput. Phys.* 264 (2014) 1–22.
- [60] J.-S. Jiang, D. Peng, Weighted ENO schemes for Hamilton-Jacobi equations, *J. Sci. Comput.* 21 (2000) 2126–2143.
- [61] F. Gibou, L. Chen, D. Nguyen, S. Banerjee, A level set based sharp interface method for the multiphase incompressible Navier-Stokes equations with phase change, *J. Comput. Phys.* 222 (2007) 536–555.
- [62] A. Esmaeeli, G. Tryggvason, Computations of film boiling. part I: numerical method, *Int. J. Heat Mass Transfer* 47 (2004) 5451–5461.
- [63] C.S. Peskin, Numerical analysis of blood flow in the heart, *J. Comput. Phys.* 25 (1977) 220–252.
- [64] M. Sussman, E. Fatemi, P. Smereka, S. Osher, An improved level set method for incompressible two-phase flows, *Comput. & Fluids* 27 (1998) 663–680.
- [65] Y. Sato, B. Niceno, A sharp-interface phase change model for a mass-conservative interface tracking method, *J. Comput. Phys.* 249 (2013) 127–161.

- [66] M.M. Francois, S.J. Cummins, E.D. Dendy, D.B. Kothe, J.M. Sicilian, M.J. Williams, A balanced-force algorithm for continuous and sharp interfacial surface tension models within a volume tracking framework, *J. Comput. Phys.* 213 (2006) 141–173.
- [67] S. Popinet, Numerical models of surface tension, *Annu. Rev. Fluid Mech.* 50 (2018) 49–75.
- [68] S.J. Cummins, M.M. Francois, D.B. Kothe, Estimating curvature from volume fractions, *Comput. Struct.* 83 (2005) 425–434.
- [69] Y. Renardy, M. Renardy, PROST: a parabolic reconstruction of surface tension for the volume-of-fluid method, *J. Comput. Phys.* 183 (2002) 400–421.
- [70] S. Popinet, An accurate adaptive solver for surface-tension-driven interfacial flows, *J. Comput. Phys.* 228 (2009) 5838–5866.
- [71] M. Sussman, E.G. Puckett, A coupled level set and volume-of-fluid method for computing 3D and axisymmetric incompressible two-phase flows, *J. Comput. Phys.* 162 (2000) 301–337.
- [72] M. Dianat, M. Skarysz, A. Garmory, A coupled level set and volume of fluid method for automotive exterior water management applications, *Int. J. Multiph. Flow* 91 (2017) 19–38.
- [73] Y. Qi, J. Lu, R. Scardovelli, S. Zaleski, G. Tryggvason, Computing curvature for volume of fluid methods using machine learning, *J. Comput. Phys.* 377 (2019) 155–161.
- [74] H.V. Patel, A. Panda, J.A.M. Kuipers, E.A.J.F. Peters, Computing interface curvature from volume fractions: a machine learning approach, *Comput. & Fluids* 193 (2019) 104263.
- [75] T. Abadie, J. Aubin, D. Legendre, On the combined effects of surface tension force calculation and interface advection on spurious currents within volume of fluid and level set frameworks, *J. Comput. Phys.* 297 (2015) 611–636.
- [76] T.C. Thulasidas, M.A. Abraham, R.L. Cerro, Flow patterns in liquid slugs during bubble-train flow inside capillaries, *Chem. Eng. Sci.* 52 (1997) 2947–2962.
- [77] M. Magnini, B. Pulvirenti, J.R. Thome, Characterization of the velocity fields generated by flow initialization in the CFD simulation of multiphase flows, *Appl. Math. Model.* 40 (2016) 6811–6830.
- [78] P. Liovic, M. Francois, M. Rudman, R. Manasseh, Efficient simulation of surface tension-dominated flows through enhanced interface geometry interrogation, *J. Comput. Phys.* 229 (2010) 7520–7544.
- [79] M. Owkes, O. Desjardins, A mesh-decoupled height function method for computing interface curvature, *J. Comput. Phys.* 281 (2015) 285–300.
- [80] V.P. Carey, *Liquid-Vapor Phase Change Phenomena*, Taylor and Francis, 1992.
- [81] H.S. Udaykumar, R. Mittal, W. Shyy, Computation of solid–liquid phase fronts in the sharp interface limit on fixed grids, *J. Comput. Phys.* 153 (1999) 535–574.
- [82] C. Kunkelmann, *Numerical Modeling and Investigation of Boiling Phenomena* (Ph.D. thesis), TU Darmstadt, Darmstadt, Germany, 2011.
- [83] R.W. Schrage, *A Theoretical Study of Interphase Mass Transfer*, Columbia University Press, New York, 1953.
- [84] I. Tanasawa, Advances in condensation heat transfer, in: J.P. Hartnett, T.F. Irvine (Eds.), *Advances in Heat Transfer*, Academic Press, San Diego, 1991.
- [85] A. Georgoulas, M. Andreadaki, M. Marengo, An enhanced VOF method coupled with heat transfer and phase change to characterise bubble detachment in saturated pool boiling, *Energies* 10 (2017) 272–306.
- [86] M. Magnini, O.K. Matar, Numerical study of the impact of the channel shape on microchannel boiling heat transfer, *Int. J. Heat Mass Transfer* 150 (2020) 119322.
- [87] A.H. Persad, C.A. Ward, Expressions for the evaporation and condensation coefficients in the Hertz-Knudsen relation, *Chem. Rev.* 116 (2016) 7727–7767.
- [88] Z. Liang, T. Biben, P. Keblynsky, Molecular simulation of steady-state evaporation and condensation: validity of the Schrage relationships, *Int. J. Heat Mass Transfer* 114 (2017) 105–114.
- [89] W.H. Lee, A pressure iteration scheme for two-phase flow modeling, in: *Multiphase Transport: Fundamentals, Reactor Safety, Applications*, 1980, pp. 407–432.
- [90] D. Lorenzini, Y. Joshi, CFD study of flow boiling in silicon microgaps with staggered pin fins for the 3D-stacking of ICs, in: *15th IEEE ITherm Conference*, 2016.
- [91] J. Lee, L.E. O’Neill, S. Lee, I. Mudawar, Experimental and computational investigation on two-phase flow and heat transfer of highly subcooled flow boiling in vertical upflow, *Int. J. Heat Mass Transfer* 136 (2019) 1199–1216, <http://dx.doi.org/10.1016/j.ijheatmasstransfer.2019.03.046>.
- [92] F.P. Bretherton, The motion of long bubbles in tubes, *J. Fluid Mech.* 10 (1961) 166–188.
- [93] M. Magnini, O.K. Matar, Morphology of long gas bubbles propagating in square capillaries, *Int. J. Multiph. Flow* 129 (2020) 103353.
- [94] G.F. Teletzke, H.T. Davis, L.E. Scriven, Wetting hydrodynamics, *Rev. Phys. Appl.* 23 (1988) 989–1007.
- [95] N. Borhani, B. Agostini, J.R. Thome, A novel time strip flow visualization technique for investigation of intermittent dewetting and dryout in elongated bubble flow in a microchannel evaporator, *Int. J. Heat Mass Transfer* 53 (2010) 4809–4818.
- [96] A. Oron, S.H. Davis, S.G. Bankoff, Long-scale evolution of thin liquid films, *Rev. Modern Phys.* 69 (1997) 931–980.
- [97] L.W. Schwartz, R.V. Roy, R.R. Elez, S. Petrash, Dewetting patterns in a drying liquid film, *J. Colloids Interface Sci.* 234 (2001) 363–374.
- [98] P. Stephan, C.A. Busse, Analysis of the heat transfer coefficient of grooved heat pipe evaporator walls, *Int. J. Heat Mass Transfer* 35 (1992) 383–391.
- [99] V.S. Ajaev, *Interfacial Fluid Mechanics: A Mathematical Modelling Approach*, Springer, New York, 2012.
- [100] M.O. Abu-Al-Saud, A. Riaz, H.A. Tchelepi, Multiscale level-set method for accurate modeling of immiscible two-phase flow with deposited thin films on solid surfaces, *J. Comput. Phys.* 333 (2017) 297–320.
- [101] A.H. Rajkotwala, *Numerical Simulations of Boiling Flows Using the Local Front Reconstruction Method* (Ph.D. thesis), Technische Universiteit Eindhoven, Eindhoven, The Netherlands, 2020.
- [102] P. Wayner Jr., Y.K. Kao, L.V. LaCroix, The interline heat-transfer coefficient of an evaporating wetting film, *Int. J. Heat Mass Transfer* 19 (1976) 487–492.
- [103] G. Son, V.K. Dhir, N. Ramanujapu, Dynamics and heat transfer associated with a single bubble during nucleate boiling on a horizontal surface, *J. Heat Mass Transfer* 121 (1999) 623–631.
- [104] W. Lee, G. Son, Bubble dynamics and heat transfer during nucleate boiling in a microchannel, *Numer. Heat Transfer A* 53 (2008) 1074–1090.
- [105] Y. Sato, B. Niceno, A depletable micro-layer model for nucleate pool boiling, *J. Comput. Phys.* 300 (2015) 20–52.
- [106] A. Guion, S. Afkhami, S. Zaleski, J. Buongiorno, Simulations of microlayer formation in nucleate boiling, *Int. J. Heat Mass Transfer* 127 (2018) 1271–1284.
- [107] Y. Chen, S. Jin, B. Yu, K. Ling, D. Sun, W. Zhang, K. Jiao, W. Tao, Modeling and study of microlayer effects on flow boiling in a mini-channel, *Int. J. Heat Mass Transfer* 208 (2023) <http://dx.doi.org/10.1016/j.ijheatmasstransfer.2023.124039>.
- [108] L. Rayleigh, XX. On the theory of surface forces. —II. Compressible fluids, *London Edinb. Dublin Philos. Mag. J. Sci.* 33 (201) (1892) 209–220, <http://dx.doi.org/10.1080/14786449208621456>.
- [109] J. van der Waals, The thermodynamic theory of capillarity flow under the hypothesis of a continuous variation of density, *J. Stat. Phys.* 20 (1893).
- [110] J. Liu, C.M. Landis, H. Gomez, T.J. Hughes, Liquid-vapor phase transition: Thermomechanical theory, entropy stable numerical formulation, and boiling simulations, *Comput. Methods Appl. Mech. Engrg.* 297 (2015) 476–553, <http://dx.doi.org/10.1016/j.cma.2015.09.007>.
- [111] A. Badillo, Quantitative phase-field modeling for boiling phenomena, *Phys. Rev. E* 86 (4) (2012) <http://dx.doi.org/10.1103/PhysRevE.86.041603>.
- [112] Z. Wang, X. Zheng, C. Chrysosostomidis, G.E. Karniadakis, A phase-field method for boiling heat transfer, *J. Comput. Phys.* 435 (2021) <http://dx.doi.org/10.1016/j.jcp.2021.110239>.
- [113] J.W. Cahn, J.E. Hilliard, Free energy of a nonuniform system interfacial free energy, *J. Chem. Phys.* 28 (258) (1958).
- [114] X. Cai, M. Wörner, O. Deutschmann, Implementation of a phase field method in OpenFOAM® for simulation of spreading droplets and verification by test problems, in: *7th Open Source CFD International Conference*, 2013.
- [115] F. Jamshidi, H. Heilmel, M. Hasert, X. Cai, O. Deutschmann, H. Marschall, M. Wörner, On suitability of phase-field and algebraic volume-of-fluid OpenFOAM® solvers for gas–liquid microfluidic applications, *Comput. Phys. Comm.* 236 (2019) 72–85, <http://dx.doi.org/10.1016/j.cpc.2018.10.015>.
- [116] S. Dong, J. Shen, A time-stepping scheme involving constant coefficient matrices for phase-field simulations of two-phase incompressible flows with large density ratios, *J. Comput. Phys.* 231 (17) (2012) 5788–5804, <http://dx.doi.org/10.1016/j.jcp.2012.04.041>.
- [117] X. Zheng, H. Babae, S. Dong, C. Chrysosostomidis, G.E. Karniadakis, A phase-field method for 3D simulation of two-phase heat transfer, *Int. J. Heat Mass Transfer* 82 (2015) 282–298, <http://dx.doi.org/10.1016/j.ijheatmasstransfer.2014.11.052>.
- [118] A. Mukherjee, S.G. Kandlikar, Z.J. Edell, Numerical study of bubble growth and wall heat transfer during flow boiling in a microchannel, *Int. J. Heat Mass Transfer* 54 (2011) 3702–3718.
- [119] X. Cai, M. Wörner, H. Marschall, O. Deutschmann, Numerical study on the wettability dependent interaction of a rising bubble with a periodic open cellular structure, *Catal. Today* 273 (2016) 151–160, <http://dx.doi.org/10.1016/j.cattod.2016.03.053>.
- [120] F. Jamshidi, *CFD Simulation of an Air Bubble in Microfluidics using Volume of Fluid and Phase Field Methods in OpenFOAM* (Ph.D. thesis), 2016, URL: <http://www.istm>.
- [121] K.V. Sharma, R. Straka, F.W. Tavares, Current status of lattice Boltzmann methods applied to aerodynamic, aeroacoustic, and thermal flows, *Prog. Aerosp. Sci.* 115 (2020) <http://dx.doi.org/10.1016/j.paerosci.2020.100616>.
- [122] X. Shan, H. Chen, Lattice Boltzmann model for simulating flows with multiple phases and components, *Phys. Rev. E* 47 (1993).
- [123] X. Shan, H. Chen, Simulation of nonideal gases and liquid-gas phase transitions by the lattice Boltzmann equation, *Phys. Rev. E* 49 (4) (1994).
- [124] T. Sun, W. Li, Three-dimensional numerical simulation of nucleate boiling bubble by lattice Boltzmann method, *Comput. & Fluids* 88 (2013) 400–409, <http://dx.doi.org/10.1016/j.compfluid.2013.10.009>.
- [125] P. Cheng, C. Zhang, S. Gong, Lattice Boltzmann simulations of macro/microscale effects on saturated pool boiling curves for heated horizontal surfaces, *J. Heat Transfer* 139 (11) (2017) <http://dx.doi.org/10.1115/1.4036578>.

- [126] S. Gong, P. Cheng, A lattice Boltzmann method for simulation of liquid-vapor phase-change heat transfer, *Int. J. Heat Mass Transfer* 55 (17–18) (2012) 4923–4927, <http://dx.doi.org/10.1016/j.ijheatmasstransfer.2012.04.037>.
- [127] C. Zhang, P. Cheng, F. Hong, Mesoscale simulation of heater size and sub-cooling effects on pool boiling under controlled wall heat flux conditions, *Int. J. Heat Mass Transfer* 101 (2016) 1331–1342, <http://dx.doi.org/10.1016/j.ijheatmasstransfer.2016.05.036>.
- [128] X. Ma, P. Cheng, X. Quan, Simulations of saturated boiling heat transfer on bio-inspired two-phase heat sinks by a phase-change lattice Boltzmann method, *Int. J. Heat Mass Transfer* 127 (2018) 1013–1024, <http://dx.doi.org/10.1016/j.ijheatmasstransfer.2018.07.082>.
- [129] X. Ma, P. Cheng, 3D simulations of pool boiling above smooth horizontal heated surfaces by a phase-change lattice Boltzmann method, *Int. J. Heat Mass Transfer* 131 (2019) 1095–1108, <http://dx.doi.org/10.1016/j.ijheatmasstransfer.2018.11.103>.
- [130] G. Hazi, A. Markus, On the bubble departure diameter and release frequency based on numerical simulation results, *Int. J. Heat Mass Transfer* 52 (5–6) (2009) 1472–1480, <http://dx.doi.org/10.1016/j.ijheatmasstransfer.2008.09.003>.
- [131] A. Begmohammadi, M. Farhadzadeh, M.H. Rahimian, Simulation of pool boiling and periodic bubble release at high density ratio using lattice Boltzmann method, *Int. Commun. Heat Mass Transfer* 61 (1) (2015) 78–87, <http://dx.doi.org/10.1016/j.icheatmasstransfer.2014.12.018>.
- [132] D. Zhang, K. Papadakis, S. Gu, Three-dimensional multi-relaxation time lattice-Boltzmann model for the drop impact on a dry surface at large density ratio, *Int. J. Multiph. Flow* 64 (2014) 11–18, <http://dx.doi.org/10.1016/j.ijmultiphaseflow.2014.04.005>.
- [133] Y. Wang, C. Shu, H.B. Huang, C.J. Teo, Multiphase lattice Boltzmann flux solver for incompressible multiphase flows with large density ratio, *J. Comput. Phys.* 280 (2015) 404–423, <http://dx.doi.org/10.1016/j.jcp.2014.09.035>.
- [134] Q. Li, K.H. Luo, Q.J. Kang, Y.L. He, Q. Chen, Q. Liu, Lattice Boltzmann methods for multiphase flow and phase-change heat transfer, *Prog. Energy Combust. Sci.* 52 (2016) 62–105, <http://dx.doi.org/10.1016/j.pecs.2015.10.001>.
- [135] L. Chen, Q. Kang, Y. Mu, Y.L. He, W.Q. Tao, A critical review of the pseudopotential multiphase lattice Boltzmann model: Methods and applications, *Int. J. Heat Mass Transfer* 76 (2014) 210–236, <http://dx.doi.org/10.1016/j.ijheatmasstransfer.2014.04.032>.
- [136] M.C. Sukop, D. Or, Lattice Boltzmann method for modeling liquid-vapor interface configurations in porous media, *Water Resour. Res.* 40 (1) (2004) <http://dx.doi.org/10.1029/2003WR002333>.
- [137] Q. Li, Q.J. Kang, M.M. Francois, Y.L. He, K.H. Luo, Lattice Boltzmann modeling of boiling heat transfer: The boiling curve and the effects of wettability, *Int. J. Heat Mass Transfer* 85 (2015) 787–796, <http://dx.doi.org/10.1016/j.ijheatmasstransfer.2015.01.136>.
- [138] Y.H. Qian, D. D’Humières, P. Lallemand, Lattice BGK models for Navier-Stokes equation, *Europhys. Lett.* 17 (6) (1992) 479–484.
- [139] A. Hu, D. Liu, 2D simulation of boiling heat transfer on the wall with an improved hybrid lattice Boltzmann model, *Appl. Therm. Eng.* 159 (2019) <http://dx.doi.org/10.1016/j.applthermaleng.2019.113788>.
- [140] H. Wang, S. Wu, H. Dai, X. Liu, C. Zhang, Lattice Boltzmann investigation of flow boiling in a microchannel, *Proc. Inst. Mech. Eng. C* 237 (11) (2022) 2507–2516, <http://dx.doi.org/10.1177/09544062221089144>.
- [141] A.D. Lavino, E. Smith, M. Magnini, O.K. Matar, Surface topography effects on pool boiling via non-equilibrium molecular dynamics simulations, *Langmuir* 37 (18) (2021) 5731–5744, <http://dx.doi.org/10.1021/acs.langmuir.1c00779>.
- [142] S.R. Yan, N. Shirani, M. Zarringhalam, D. Toghraie, Q. Nguyen, A. Karimipour, Prediction of boiling flow characteristics in rough and smooth microchannels using molecular dynamics simulation: Investigation of the effects of boundary wall temperatures, *J. Mol. Liq.* 306 (2020) <http://dx.doi.org/10.1016/j.molliq.2020.112937>.
- [143] S. Rostami, M. Zarringhalam, A. Alizadeh, D. Toghraie, A. Shahsavvar Gordanlou, Molecular dynamic simulation of argon boiling flow inside smooth and rough microchannels by considering the effects of cubic barriers, *J. Mol. Liq.* 312 (2020) <http://dx.doi.org/10.1016/j.molliq.2020.113130>.
- [144] A. Mosavi, M. Zarringhalam, D. Toghraie, A. Rahmani, A. Karimipour, Boiling of argon flow in a microchannel by considering the spherical geometry for roughness barriers using molecular dynamics simulation, *J. Mol. Liq.* 321 (2021) <http://dx.doi.org/10.1016/j.molliq.2020.114462>.
- [145] W. Liu, M.O. AL-Khafaji, Z. Ali Bu sinnah, M. Gh. Said, N. Ali Salman, K. Al-Majidi, A. Hashim Abdulkadhim, M. Zarringhalam, S. Baghaei, Effects of barriers on the thermal enhancement in boiling flow within a ribbed-microchannel using molecular dynamics simulation approach, *Ain Shams Eng. J.* 14 (10) (2023) <http://dx.doi.org/10.1016/j.asej.2023.102195>.
- [146] X. Wang, Y. Li, J.A. Malen, A.J. McGaughey, Assessing the impact of disjoining pressure on thin-film evaporation with atomistic simulation and kinetic theory, *Appl. Phys. Lett.* 116 (21) (2020) 1–6, <http://dx.doi.org/10.1063/5.0010467>.
- [147] A. Chandra, P. Keblinski, Investigating the validity of schrage relationships for water using molecular dynamics simulations, *J. Chem. Phys.* 153 (12) (2020) <http://dx.doi.org/10.1063/5.0018726>.
- [148] E. Bird, J. Gutierrez Plascencia, Z. Liang, Thermal transport across the interface between liquid n-dodecane and its own vapor: A molecular dynamics study, *J. Chem. Phys.* 152 (18) (2020) <http://dx.doi.org/10.1063/1.5144279>.
- [149] A. Georgoulas, M. Marengo, Numerical simulation of flow boiling in microchannels: bubble growth, detachment and coalescence, in: *14th UK Heat Transfer Conference*, 2015.
- [150] K. Vontas, N. Miche, M. Marengo, A. Georgoulas, Numerical investigation of the solid surface material influence on flow boiling in microchannels, *Appl. Therm. Eng.* 217 (2022) 119006.
- [151] I. El Mellas, N. Samkhaniani, C. Falsetti, A. Stroh, M. Icardi, M. Magnini, Numerical investigation of bubble dynamics and flow boiling heat transfer in cylindrical micro-pin-fin heat exchangers, *Int. J. Heat Mass Transfer* 228 (2024) <http://dx.doi.org/10.1016/j.ijheatmasstransfer.2024.125620>.
- [152] C. Falsetti, M. Magnini, J.R. Thome, Hydrodynamic and thermal analysis of a micro-pin fin evaporator for on-chip two-phase cooling of high density power micro-electronics, *Appl. Therm. Eng.* 130 (2018) 1425–1439.
- [153] C. Falsetti, M. Magnini, J.R. Thome, A new flow pattern-based boiling heat transfer model for micro-pin fin evaporators, *Int. J. Heat Mass Transfer* 122 (2018) 1425–1439.
- [154] M. Yazdani, T. Radcliff, M. Soteriou, A.A. Alahyari, A high-fidelity approach towards simulation of pool boiling, *Phys. Fluids* 28 (1) (2016) <http://dx.doi.org/10.1063/1.4940042>.
- [155] A. Faghri, *Heat Pipe Science and Technology*, Global Digital Press, 1995.
- [156] Y. Sato, B. Niceno, Nucleate pool boiling simulations using the interface tracking method: Boiling regime from discrete bubble to vapor mushroom region, *Int. J. Heat Mass Transfer* 105 (2017) 505–524, <http://dx.doi.org/10.1016/j.ijheatmasstransfer.2016.10.018>.
- [157] Y.J. Chen, K. Ling, H. Ding, Y. Wang, S.Q. Jin, W.Q. Tao, 3-d numerical study of subcooled flow boiling in a horizontal rectangular mini-channel by VOFSET, *Int. J. Heat Mass Transfer* 183 (2022) <http://dx.doi.org/10.1016/j.ijheatmasstransfer.2021.122218>.
- [158] Y. Chen, R. Kulenovic, R. Mertz, Numerical study of the formation of Taylor bubbles in capillary tubes, *Int. J. Therm. Sci.* 48 (2009) 234–242.
- [159] Q. Li, Y. Jiao, M. Avramova, P. Chen, J. Yu, J. Chen, J. Hou, Development, verification and application of a new model for active nucleation site density in boiling systems, *Nucl. Eng. Des.* 328 (2018) 1–9, <http://dx.doi.org/10.1016/j.nucengdes.2017.12.027>.
- [160] F. Magaletti, A. Georgoulas, M. Marengo, Unraveling low nucleation temperatures in pool boiling through fluctuating hydrodynamics simulations, *Int. J. Multiph. Flow* 130 (2020) 103356.
- [161] M. Gallo, F. Magaletti, A. Georgoulas, M. Marengo, J. De Coninck, C.M. Casciola, A nanoscale view of the origin of boiling and its dynamics, *Nature Commun.* 14 (1) (2023) <http://dx.doi.org/10.1038/s41467-023-41959-3>.
- [162] G. Gennari, E.R. Smith, G.J. Pringle, M. Magnini, Coupled atomistic-continuum simulations of nucleate boiling, *Int. J. Therm. Sci.* 200 (2024) <http://dx.doi.org/10.1016/j.ijthermalsci.2024.108954>.
- [163] S. Gong, P. Cheng, Numerical investigation of saturated flow boiling in microchannels by the lattice Boltzmann method, *Numer. Heat Transfer A* 65 (7) (2014) 644–661, <http://dx.doi.org/10.1080/10407782.2013.836025>.
- [164] M.M. Mahmoud, T.G. Karayiannis, Pool boiling review: Part I – fundamentals of boiling and relation to surface design, 2021, <http://dx.doi.org/10.1016/j.tsep.2021.101024>.
- [165] M.M. Mahmoud, T.G. Karayiannis, D.B. Kenning, Surface effects in flow boiling of R134a in microtubes, *Int. J. Heat Mass Transfer* 54 (15–16) (2011) 3334–3346, <http://dx.doi.org/10.1016/j.ijheatmasstransfer.2011.03.052>.
- [166] S.W. Welch, J. Wilson, A volume of fluid based method for fluid flows with phase change, *J. Comput. Phys.* 160 (2) (2000) 662–682, <http://dx.doi.org/10.1006/jcp.2000.6481>.
- [167] S. Hardt, F. Wondra, Evaporation model for interfacial flows based on a continuum-field representation of the source terms, *J. Comput. Phys.* 227 (11) (2008) 5871–5895, <http://dx.doi.org/10.1016/j.jcp.2008.02.020>.
- [168] N. Samkhaniani, M.R. Ansari, The evaluation of the diffuse interface method for phase change simulations using OpenFOAM, *Heat Transfer - Asian Res.* 46 (8) (2017) 1173–1203, <http://dx.doi.org/10.1002/htj.21268>.
- [169] M. Irfan, M. Muradoglu, A front tracking method for direct numerical simulation of evaporation process in a multiphase system, *J. Comput. Phys.* 337 (2017) 132–153, <http://dx.doi.org/10.1016/j.jcp.2017.02.036>.
- [170] L.E. Scriven, On the dynamics of phase growth, *Chem. Eng. Sci.* 10 (1959) 1–13.
- [171] I.C. Chu, H.C. No, C.H. Song, Visualization of boiling structure and critical heat flux phenomenon for a narrow heating surface in a horizontal pool of saturated water, *Int. J. Heat Mass Transfer* 62 (1) (2013) 142–152, <http://dx.doi.org/10.1016/j.ijheatmasstransfer.2013.02.067>.
- [172] S. Jung, H. Kim, An experimental method to simultaneously measure the dynamics and heat transfer associated with a single bubble during nucleate boiling on a horizontal surface, *Int. J. Heat Mass Transfer* 73 (2014) 365–375, <http://dx.doi.org/10.1016/j.ijheatmasstransfer.2014.02.014>.
- [173] S. Jung, H. Kim, Hydrodynamic formation of a microlayer underneath a boiling bubble, *Int. J. Heat Mass Transfer* 120 (2018) 1229–1240, <http://dx.doi.org/10.1016/j.ijheatmasstransfer.2017.12.098>.

- [174] T. Chen, S.V. Garimella, Local heat transfer distribution and effect of instabilities during flow boiling in a silicon microchannel heat sink, *Int. J. Heat Mass Transfer* 54 (15–16) (2011) 3179–3190, <http://dx.doi.org/10.1016/j.ijheatmasstransfer.2011.04.012>.
- [175] T. Yabuki, O. Nakabeppu, Heat transfer mechanisms in isolated bubble boiling of water observed with MEMS sensor, *Int. J. Heat Mass Transfer* 76 (2014) 286–297, <http://dx.doi.org/10.1016/j.ijheatmasstransfer.2014.04.012>.
- [176] M. Zupančič, P. Gregorčič, M. Bucci, C. Wang, G. Matana Aguiar, M. Bucci, The wall heat flux partitioning during the pool boiling of water on thin metallic foils, *Appl. Therm. Eng.* 200 (2022) <http://dx.doi.org/10.1016/j.applthermaleng.2021.117638>.
- [177] L. Bureš, Y. Sato, Comprehensive simulations of boiling with a resolved microlayer: Validation and sensitivity study, *J. Fluid Mech.* 933 (2022) <http://dx.doi.org/10.1017/jfm.2021.1108>.
- [178] F. Mucicchi, C.N. Markides, O.K. Matar, M. Magnini, Computational study of bubble, thin-film dynamics and heat transfer during flow boiling in non-circular microchannels, *Appl. Therm. Eng.* 238 (2024) <http://dx.doi.org/10.1016/j.applthermaleng.2023.122039>.
- [179] M. Bucci, *A Theoretical and Experimental Study of Vapor Bubble Dynamics in Separate Effect Pool Boiling Conditions* (Ph.D. thesis), 2020.
- [180] S. Narayan, A. Srivastava, S. Singh, Rainbow schlieren-based investigation of heat transfer mechanisms during isolated nucleate pool boiling phenomenon: Effect of superheat levels, *Int. J. Heat Mass Transfer* 120 (2018) 127–143, <http://dx.doi.org/10.1016/j.ijheatmasstransfer.2017.12.005>.
- [181] V. Voulgaropoulos, G.M. Aguiar, C.N. Markides, M. Bucci, Simultaneous laser-induced fluorescence, particle image velocimetry and infrared thermography for the investigation of the flow and heat transfer characteristics of nucleating vapour bubbles, *Int. J. Heat Mass Transfer* 187 (2022) <http://dx.doi.org/10.1016/j.ijheatmasstransfer.2022.122525>.
- [182] Z. Dong, J. Xu, F. Jiang, P. Liu, Numerical study of vapor bubble effect on flow and heat transfer in microchannel, *Int. J. Therm. Sci.* 54 (2012) 22–32, <http://dx.doi.org/10.1016/j.ijthermalsci.2011.11.019>.
- [183] J. Xu, W. Zhang, G. Liu, Seed bubble guided heat transfer in a single microchannel, in: *Heat Transfer Engineering*, Vol. 32, 2011, pp. 1031–1036, <http://dx.doi.org/10.1080/01457632.2011.556493>.
- [184] N. Tiwari, M.K. Moharana, Conjugate heat transfer analysis of liquid-vapor two phase flow in a microtube: A numerical investigation, *Int. J. Heat Mass Transfer* 142 (2019) <http://dx.doi.org/10.1016/j.ijheatmasstransfer.2019.07.077>.
- [185] S.C. Huang, O. Kawanami, K. Kawakami, I. Honda, Y. Kawashima, H. Ohta, Experimental study of the relation between heat transfer and flow behavior in a single microtube, *Microgravity Sci. Technol.* 20 (3–4) (2008) 193–197, <http://dx.doi.org/10.1007/s12217-008-9079-3>.
- [186] J. Yoo, C.E. Estrada-Perez, Y.A. Hassan, Experimental study on bubble dynamics and wall heat transfer arising from a single nucleation site at subcooled flow boiling conditions - part 2: Data analysis on sliding bubble characteristics and associated wall heat transfer, *Int. J. Multiph. Flow* 84 (2016) 292–314, <http://dx.doi.org/10.1016/j.ijmultiphaseflow.2016.04.019>.
- [187] P. Bhuvankar, S. Dabiri, Simulation of flow boiling in micro-channels: Effects of inlet flow rate and hot-spots, *Int. J. Heat Fluid Flow* 85 (2020) <http://dx.doi.org/10.1016/j.ijheatfluidflow.2020.108616>.
- [188] R. Revellin, V. Dupont, T. Ursenbacher, J.R. Thome, I. Zun, Characterization of diabatic two-phase flows in microchannels: Flow parameter results for R-134a in a 0.5 mm channel, *Int. J. Multiph. Flow* 32 (7) (2006) 755–774, <http://dx.doi.org/10.1016/j.ijmultiphaseflow.2006.02.016>.
- [189] R. Zhuang, W. Wang, Flow pattern of boiling in micro-channel by numerical simulation, *Int. J. Heat Mass Transfer* 55 (5–6) (2012) 1741–1753, <http://dx.doi.org/10.1016/j.ijheatmasstransfer.2011.11.029>.
- [190] S.M. Kim, I. Mudawar, Review of databases and predictive methods for heat transfer in condensing and boiling mini/micro-channel flows, 2014, pp. 627–652, <http://dx.doi.org/10.1016/j.ijheatmasstransfer.2014.05.036>.
- [191] J. Broughton, Y.K. Joshi, Flow boiling in geometrically modified microchannels, *Phys. Fluids* 33 (10) (2021) <http://dx.doi.org/10.1063/5.0062585>.
- [192] W. Zhang, T. Hibiki, K. Mishima, Correlation for flow boiling heat transfer in mini-channels, *Int. J. Heat Mass Transfer* 47 (26) (2004) 5749–5763, <http://dx.doi.org/10.1016/j.ijheatmasstransfer.2004.07.034>.
- [193] S.S. Bertsch, E.A. Groll, S.V. Garimella, A composite heat transfer correlation for saturated flow boiling in small channels, *Int. J. Heat Mass Transfer* 52 (7–8) (2009) 2110–2118, <http://dx.doi.org/10.1016/j.ijheatmasstransfer.2008.10.022>.
- [194] N. Tiwari, M.K. Moharana, Conjugate effect on flow boiling instability in wavy microchannel, *Int. J. Heat Mass Transfer* 166 (2021) <http://dx.doi.org/10.1016/j.ijheatmasstransfer.2020.120791>.
- [195] U.K. Alujoju, S.K. Dubey, A. Javed, 3D transient heat transfer analysis and flow visualization study in diverging microchannel for instability mitigated two-phase flow: A numerical study, *Int. J. Heat Mass Transfer* 160 (2020) <http://dx.doi.org/10.1016/j.ijheatmasstransfer.2020.120212>.
- [196] I. Yeo, S. Lee, 2D computational investigation into transport phenomena of subcooled and saturated flow boiling in large length to diameter ratio micro-channel heat sinks, *Int. J. Heat Mass Transfer* 183 (2022) <http://dx.doi.org/10.1016/j.ijheatmasstransfer.2021.122128>.
- [197] C. Falsetti, H. Jafarpoorchehab, M. Magnini, N. Borhani, J.R. Thome, Two-phase operational maps, pressure drop, and heat transfer for flow boiling of R236fa in a micro-pin fin evaporator, *Int. J. Heat Mass Transfer* 107 (2017) 805–819.
- [198] M. Schepperle, N. Samkhaniani, M. Magnini, P. Woias, A. Stroh, Understanding inconsistencies in thermohydraulic characteristics between experimental and numerical data for di water flow through a rectangular microchannel, *J. Heat Mass Transfer* 146 (3) (2023) 031801, <http://dx.doi.org/10.1115/1.4064330>.
- [199] F. Mucicchi, I. El Mellas, O.K. Matar, M. Magnini, Conjugate heat transfer effects on flow boiling in microchannels, *Int. J. Heat Mass Transfer* 195 (2022) <http://dx.doi.org/10.1016/j.ijheatmasstransfer.2022.123166>.
- [200] W. Qu, I. Mudawar, Measurement and correlation of critical heat flux in two-phase micro-channel heat sinks, *Int. J. Heat Mass Transfer* 47 (10–11) (2004) 2045–2059, <http://dx.doi.org/10.1016/j.ijheatmasstransfer.2003.12.006>.
- [201] D.O. Ariyo, T. Bello-Ochende, *Critical Heat Fluxes for Subcooled Flow Boiling in Optimised Microchannels*, Technical Report 2, 2020, pp. 140–154.
- [202] Z. Tian, K. Li, Y. Zhang, Z. Huang, S. Xu, W. Gao, Numerical simulation of microchannel flow boiling and critical heat flux under rolling motion, *Int. J. Refrig.* 145 (2023) 118–128, <http://dx.doi.org/10.1016/j.ijrefrig.2022.08.025>.
- [203] S.R. Rao, Y. Peles, Spatiotemporally resolved heat transfer measurements for flow boiling in microchannels, *Int. J. Heat Mass Transfer* 89 (2015) 482–493, <http://dx.doi.org/10.1016/j.ijheatmasstransfer.2015.05.062>.
- [204] T.A. Kingston, J.A. Weibel, S.V. Garimella, An experimental method for controlled generation and characterization of microchannel slug flow boiling, *Int. J. Heat Mass Transfer* 106 (2017) 619–628, <http://dx.doi.org/10.1016/j.ijheatmasstransfer.2016.09.036>.
- [205] S. Korniliou, C. Mackenzie-Dover, S. Harmand, G. Duursma, J.R.E. Christy, J.G. Terry, A.J. Walton, K. Sefiane, Local wall temperature mapping during flow boiling in a transparent microchannel, *Int. J. Therm. Sci.* 135 (2019) 344–361.
- [206] P. Zhang, T. Wang, Y. Jiang, C. Guo, Measurement of transient liquid film and its effect on flow boiling heat transfer in non-circular microchannels, *Int. J. Therm. Sci.* 184 (2023) <http://dx.doi.org/10.1016/j.ijthermalsci.2022.108004>.
- [207] W. Li, Z. Wu, A general criterion for evaporator heat transfer in micro/mini-channels, *Int. J. Heat Mass Transfer* 53 (9–10) (2010) 1967–1976, <http://dx.doi.org/10.1016/j.ijheatmasstransfer.2009.12.059>.
- [208] M.M. Mahmoud, T.G. Karayiannis, Heat transfer correlation for flow boiling in small to micro tubes, *Int. J. Heat Mass Transfer* 66 (2013) 553–574, <http://dx.doi.org/10.1016/j.ijheatmasstransfer.2013.07.042>.
- [209] M. Nabil, A.S. Rattner, InterThermalPhaseChangeFoam—A framework for two-phase flow simulations with thermally driven phase change, *SoftwareX* 5 (2016) 216–226, <http://dx.doi.org/10.1016/j.softx.2016.10.002>.
- [210] N. Samkhaniani, M.R. Ansari, Numerical simulation of bubble condensation using CF-VOF, *Prog. Nucl. Energy* 89 (2016) 120–131, <http://dx.doi.org/10.1016/j.pnucene.2016.02.004>.
- [211] H. Scheufler, J. Roenby, TwoPhaseFlow: A framework for developing two phase flow solvers in OpenFOAM, *OpenFOAM® J.* 3 (2023) 200–224, <http://dx.doi.org/10.51560/ofj.v3.80>.
- [212] Y. Sato, B. Niceno, Nucleate pool boiling simulations using the interface tracking method: Boiling regime from discrete bubble to vapor mushroom region, *Int. J. Heat Mass Transfer* 105 (2017) 505–524.
- [213] Y. Sato, B. Niceno, Pool boiling simulation using an interface tracking method: From nucleate boiling to film boiling regime through critical heat flux, *Int. J. Heat Mass Transfer* 125 (2018) 876–890.
- [214] S. Lal, Y. Sato, B. Niceno, Direct numerical simulation of bubble dynamics in subcooled and near-saturated convective nucleate boiling, *Int. J. Heat Fluid Flow* 51 (2015) 16–28.
- [215] T. Harirchian, S.V. Garimella, Flow regime-based modeling of heat transfer and pressure drop in microchannel flow boiling, *Int. J. Heat Mass Transfer* 55 (2012) 1246–1260.
- [216] A. Cioncolini, J.R. Thome, Algebraic turbulence modeling in adiabatic and evaporating annular two-phase flow, *Int. J. Heat Fluid Flow* 32 (2011) 805–817.
- [217] M. Andreadaki, K. Vontas, A. Georgoulas, N. Miché, M. Marengo, The effect of channel aspect ratio on flow boiling characteristics within rectangular micro-passages, *Int. J. Heat Mass Transfer* 183 (2022) <http://dx.doi.org/10.1016/j.ijheatmasstransfer.2021.122201>.
- [218] Z. Pan, J.A. Weibel, S.V. Garimella, A saturated-interface-volume phase change model for simulating flow boiling, *Int. J. Heat Mass Transfer* 93 (2016) 945–956, <http://dx.doi.org/10.1016/j.ijheatmasstransfer.2015.10.044>.
- [219] Y.K. Prajapati, M. Pathak, M.K. Khan, Numerical investigation of subcooled flow boiling in segmented finned microchannels, *Int. Commun. Heat Mass Transfer* 86 (2017) 215–221, <http://dx.doi.org/10.1016/j.icheatmasstransfer.2017.06.009>.
- [220] J. Chen, S. Ahmad, W. Deng, J. Cai, J. Zhao, Micro/nanoscale surface on enhancing the microchannel flow boiling performance: A lattice Boltzmann simulation, *Appl. Therm. Eng.* 205 (2022) <http://dx.doi.org/10.1016/j.applthermaleng.2022.118036>.
- [221] J. Potgieter, L. Lombaard, J. Hannay, M.A. Moghimi, P. Valluri, J.P. Meyer, Adaptive mesh refinement method for the reduction of computational costs while simulating slug flow, *Int. Commun. Heat Mass Transfer* 129 (2021) <http://dx.doi.org/10.1016/j.icheatmasstransfer.2021.105702>.

- [222] A. Serizawa, Z. Feng, Z. Kawara, Two-phase flow in microchannels, *Exp. Therm Fluid Sci.* 26 (6–7) (2002) 703–714, URL: www.elsevier.com/locate/etfs.
- [223] J.D. Da Silva, *Two-Phase Flow Pressure Drop in a Single 1.1mm I.D. Tube* (Ph.D. thesis), Escola de Engenharia de São Carlos (EESC), University of São Paulo, 2012.
- [224] A.A. Arcanjo, C.B. Tibiriçá, G. Ribatski, Evaluation of flow patterns and elongated bubble characteristics during the flow boiling of halocarbon refrigerants in a micro-scale channel, *Exp. Therm Fluid Sci.* 34 (6) (2010) 766–775, <http://dx.doi.org/10.1016/j.expthermflusci.2010.01.006>.
- [225] A. Mukherjee, S.G. Kandlikar, Numerical simulation of growth of a vapor bubble during flow boiling of water in a microchannel, *Microfluid. Nanofluid.* 1 (2) (2005) 137–145, <http://dx.doi.org/10.1007/s10404-004-0021-8>.
- [226] M.E. Steinke, S.G. Kandlikar, An experimental investigation of flow boiling characteristics of water in parallel microchannels, *J. Heat Transfer* 126 (4) (2004) 518–526, <http://dx.doi.org/10.1115/1.1778187>.
- [227] W. Lee, G. Son, Bubble dynamics and heat transfer during nucleate boiling in a microchannel, *Numer Heat Transfer A* 53 (10) (2008) 1074–1090, <http://dx.doi.org/10.1080/10407780701789898>.
- [228] A. Mukherjee, Contribution of thin-film evaporation during flow boiling inside microchannels, *Int. J. Therm. Sci.* 48 (11) (2009) 2025–2035, <http://dx.doi.org/10.1016/j.ijthermalsci.2009.03.006>.
- [229] M. Magnini, B. Pulvirenti, J.R. Thome, Numerical investigation of hydrodynamics and heat transfer of elongated bubbles during flow boiling in a microchannel, *Int. J. Heat Mass Transfer* 59 (1) (2013) 451–471, <http://dx.doi.org/10.1016/j.ijheatmasstransfer.2012.12.010>.
- [230] M. Magnini, J.R. Thome, A CFD study of the parameters influencing heat transfer in microchannel slug flow boiling, *Int. J. Therm. Sci.* 110 (2016) 119–136, <http://dx.doi.org/10.1016/j.ijthermalsci.2016.06.032>.
- [231] A. Ferrari, M. Magnini, J.R. Thome, Numerical analysis of slug flow boiling in square microchannels, *Int. J. Heat Mass Transfer* 123 (2018) 928–944, <http://dx.doi.org/10.1016/j.ijheatmasstransfer.2018.03.012>.
- [232] M. Magnini, O.K. Matar, Numerical study of the impact of the channel shape on microchannel boiling heat transfer, *Int. J. Heat Mass Transfer* 150 (2020) <http://dx.doi.org/10.1016/j.ijheatmasstransfer.2020.119322>.
- [233] M. Andredaki, A. Georgoulas, N. Miche, M. Marengo, Numerical investigation of liquid film instabilities and evaporation in confined oscillating slug-plug flows, in: *WIT Transactions on Engineering Sciences*, Vol. 123, 2019, pp. 127–138, <http://dx.doi.org/10.2495/MPF190121>.
- [234] K. Fukagata, N. Kasagi, P. Ua-arayaporn, T. Himeno, Numerical simulation of gas-liquid two-phase flow and convective heat transfer in a micro tube, *Int. J. Heat Fluid Flow* 28 (1 SPEC. ISS.) (2007) 72–82, <http://dx.doi.org/10.1016/j.ijheatfluidflow.2006.04.010>.
- [235] Y.Q. Zu, Y.Y. Yan, S. Gedupudi, T.G. Karayiannis, D.B. Kenning, Confined bubble growth during flow boiling in a mini-/micro-channel of rectangular cross-section part II: Approximate 3-D numerical simulation, *Int. J. Therm. Sci.* 50 (3) (2011) 267–273, <http://dx.doi.org/10.1016/j.ijthermalsci.2010.09.004>.
- [236] R. Jafari, T. Okutucu-Özyurt, Phase-field modeling of vapor bubble growth in a microchannel, *J. Comput. Multiph. Flows* 7 (3) (2014) 143–158.
- [237] R. Jafari, T. Okutucu-Özyurt, Numerical simulation of flow boiling from an artificial cavity in a microchannel, *Int. J. Heat Mass Transfer* 97 (2016) 270–278, <http://dx.doi.org/10.1016/j.ijheatmasstransfer.2016.02.028>.
- [238] G. Katiyar, S. Karagadde, S.K. Saha, A. Sharma, Numerical modelling of bubble growth in microchannel using level set method, *Int. J. Heat Mass Transfer* 101 (2016) 719–732, <http://dx.doi.org/10.1016/j.ijheatmasstransfer.2016.05.029>.
- [239] A.H. Rajkotwala, L.L. Boer, E.A. Peters, C.W. van der Geld, J.G. Kuerten, J.A. Kuipers, M.W. Baltussen, A numerical study of flow boiling in a microchannel using the local front reconstruction method, *AIChE J.* 68 (4) (2022) <http://dx.doi.org/10.1002/aic.17598>.
- [240] K. Ling, G. Son, D.L. Sun, W.Q. Tao, Three dimensional numerical simulation on bubble growth and merger in microchannel boiling flow, *Int. J. Therm. Sci.* 98 (2015) 135–147, <http://dx.doi.org/10.1016/j.ijthermalsci.2015.06.019>.
- [241] Q. Liu, B. Palm, Numerical study of bubbles rising and merging during convective boiling in micro-channels, *Appl. Therm. Eng.* 99 (2016) 1141–1151, <http://dx.doi.org/10.1016/j.applthermaleng.2016.01.116>.
- [242] Q. Liu, W. Wang, B. Palm, Numerical study of the interactions and merge of multiple bubbles during convective boiling in micro channels, *Int. Commun. Heat Mass Transfer* 80 (2017) 10–17, <http://dx.doi.org/10.1016/j.icheatmasstransfer.2016.11.009>.
- [243] C. Huh, M.H. Kim, An experimental investigation of flow boiling in an asymmetrically heated rectangular microchannel, *Exp. Therm Fluid Sci.* 30 (8) (2006) 775–784, <http://dx.doi.org/10.1016/j.expthermflusci.2006.03.007>.
- [244] T.H. Yen, M. Shoji, F. Takemura, Y. Suzuki, N. Kasagi, Visualization of convective boiling heat transfer in single microchannels with different shaped cross-sections, *Int. J. Heat Mass Transfer* 49 (21–22) (2006) 3884–3894, <http://dx.doi.org/10.1016/j.ijheatmasstransfer.2005.12.024>.
- [245] M. Magnini, B. Pulvirenti, J.R. Thome, Numerical investigation of the influence of leading and sequential bubbles on slug flow boiling within a microchannel, *Int. J. Therm. Sci.* 71 (2013) 36–52, <http://dx.doi.org/10.1016/j.ijthermalsci.2013.04.018>.
- [246] Q. Liu, W. Wang, B. Palm, C. Wang, X. Jiang, On the dynamics and heat transfer of bubble train in micro-channel flow boiling, *Int. Commun. Heat Mass Transfer* 87 (2017) 198–203, <http://dx.doi.org/10.1016/j.icheatmasstransfer.2017.07.002>.
- [247] D. Rahman, A. Mukherjee, Numerical simulation of multiple bubble interaction during flow boiling in microchannels, in: *Proceedings of the ASME 2022 Heat Transfer Summer Conference*, 2022.
- [248] D. Rahman, A. Mukherjee, Numerical simulation of three bubbles interaction during flow boiling of water in microchannel, in: *Proceedings of the ASME 2022 Heat Transfer Summer Conference*, 2022.
- [249] K. Guo, H. Li, Y. Feng, J. Zhao, T. Wang, Numerical investigation on single bubble and multiple bubbles growth and heat transfer during flow boiling in A microchannel using the VOSET method, *Microgravity Sci. Technol.* 31 (4) (2019) 381–393, <http://dx.doi.org/10.1007/s12217-019-9697-y>.
- [250] W.T. Yan, W.B. Ye, C. Li, Effect of aspect ratio on saturated boiling flow in microchannels with nonuniform heat flux, *Heat Transfer - Asian Res.* 48 (7) (2019) 3312–3327, <http://dx.doi.org/10.1002/htj.21543>.
- [251] L. Zhang, J.-M. Koo, L. Jiang, M. Asheghi, K.E. Goodson, J.G. Santiago, T.W. Kenny, Measurements and modeling of two-phase flow in microchannels with nearly constant heat flux boundary conditions, *J. Microelectromech. Syst.* 11 (1) (2002).
- [252] Q. Liu, W. Wang, B. Palm, A numerical study of the transition from slug to annular flow in micro-channel convective boiling, *Appl. Therm. Eng.* 112 (2017) 73–81, <http://dx.doi.org/10.1016/j.applthermaleng.2016.10.020>.
- [253] Y. Luo, W. Li, K. Zhou, K. Sheng, S. Shao, Z. Zhang, J. Du, W.J. Minkowycz, Three-dimensional numerical simulation of saturated annular flow boiling in a narrow rectangular microchannel, *Int. J. Heat Mass Transfer* 149 (2020) <http://dx.doi.org/10.1016/j.ijheatmasstransfer.2019.119246>.
- [254] E. Da Riva, D. Del Col, S.V. Garimella, A. Cavallini, The importance of turbulence during condensation in a horizontal circular minichannel, *Int. J. Heat Mass Transfer* 55 (13–14) (2012) 3470–3481, <http://dx.doi.org/10.1016/j.ijheatmasstransfer.2012.02.026>.
- [255] M. Magnini, O.K. Matar, Fundamental study of wax deposition in crude oil flows in a pipeline via interface-resolved numerical simulations, *Ind. Eng. Chem. Res.* 58 (47) (2019) 21797–21816, <http://dx.doi.org/10.1021/acs.iecr.9b05250>.
- [256] F.R. Menter, Two-equation eddy-viscosity turbulence models for engineering applications, *AIAA J.* 32 (8) (1994) 1598–1605.
- [257] W. Fan, A.V. Cherdantsev, H. Anglart, Experimental and numerical study of formation and development of disturbance waves in annular gas-liquid flow, *Energy* 207 (2020) <http://dx.doi.org/10.1016/j.energy.2020.118309>.
- [258] Y. Luo, J. Li, K. Zhou, J. Zhang, W. Li, A numerical study of subcooled flow boiling in a manifold microchannel heat sink with varying inlet-to-outlet width ratio, *Int. J. Heat Mass Transfer* 139 (2019) 554–563, <http://dx.doi.org/10.1016/j.ijheatmasstransfer.2019.05.030>.
- [259] K.D. Cole, B. Çetin, The effect of axial conduction on heat transfer in a liquid microchannel flow, *Int. J. Heat Mass Transfer* 54 (11–12) (2011) 2542–2549, <http://dx.doi.org/10.1016/j.ijheatmasstransfer.2011.02.007>.
- [260] G. Maranzana, I. Perry, D. Maillet, Mini- and micro-channels: Influence of axial conduction in the walls, *Int. J. Heat Mass Transfer* 47 (17–18) (2004) 3993–4004, <http://dx.doi.org/10.1016/j.ijheatmasstransfer.2004.04.016>.
- [261] Y. Lin, J. Li, Y. Luo, W. Li, X. Luo, S. Kabelac, Y. Cao, W.J. Minkowycz, Conjugate heat transfer analysis of bubble growth during flow boiling in a rectangular microchannel, *Int. J. Heat Mass Transfer* 181 (2021) <http://dx.doi.org/10.1016/j.ijheatmasstransfer.2021.121828>.
- [262] K. Vontas, M. Andredaki, A. Georgoulas, N. Miché, M. Marengo, The effect of hydraulic diameter on flow boiling within single rectangular microchannels and comparison of heat sink configuration of a single and multiple microchannels, *Energies* 14 (20) (2021) <http://dx.doi.org/10.3390/en14206641>.
- [263] Y. Suh, W. Lee, G. Son, Bubble dynamics, flow, and heat transfer during flow boiling in parallel microchannels, *Numer Heat Transfer A* 54 (4) (2008) 390–405, <http://dx.doi.org/10.1080/10407780802164561>.
- [264] Y. Lin, Y. Luo, W. Li, J. Li, Z. Sun, Y. Cao, W.J. Minkowycz, Numerical study of flow reversal during bubble growth and confinement of flow boiling in microchannels, *Int. J. Heat Mass Transfer* 177 (2021) <http://dx.doi.org/10.1016/j.ijheatmasstransfer.2021.121491>.
- [265] S.G. Kandlikar, Fundamental issues related to flow boiling in minichannels and microchannels, *Exp. Therm Fluid Sci.* 26 (2–4) (2002) 389–407, URL: www.elsevier.com/locate/etfs.
- [266] J.R. Thome, Boiling in microchannels: A review of experiment and theory, *Int. J. Heat Fluid Flow* 25 (2) (2004) 128–139, <http://dx.doi.org/10.1016/j.ijheatfluidflow.2003.11.005>.
- [267] T. Saenen, J.R. Thome, Dynamic numerical microchannel evaporator model to investigate parallel channel instabilities, *J. Electron. Packag. Trans. ASME* 138 (1) (2016) <http://dx.doi.org/10.1115/1.4032490>.
- [268] S. Szczukiewicz, N. Borhani, J.R. Thome, Two-phase heat transfer and high-speed visualization of refrigerant flows in 100 x 100 μm² silicon multi-microchannels, *Int. J. Refrig.* 36 (2) (2013) 402–413.
- [269] M.M. Mahmoud, T.G. Karayiannis, Pool boiling review: Part II – heat transfer enhancement, *Therm. Sci. Eng. Prog.* 25 (2021) <http://dx.doi.org/10.1016/j.tsep.2021.101023>.

- [270] S. Krishnamurthy, Y. Peles, Flow boiling on micropin fins entrenched inside a microchannel-flow patterns and bubble departure diameter and bubble frequency, *J. Heat Transfer* 132 (4) (2010) 1–9, <http://dx.doi.org/10.1115/1.2994718>.
- [271] S.G. Kandlikar, W.K. Kuan, D.A. Willistein, J. Borrelli, Stabilization of flow boiling in microchannels using pressure drop elements and fabricated nucleation sites, *J. Heat Transfer* 128 (4) (2006) 389–396, <http://dx.doi.org/10.1115/1.2165208>.
- [272] W. Lee, G. Son, H.Y. Yoon, Direct numerical simulation of flow boiling in a finned microchannel, *Int. Commun. Heat Mass Transfer* 39 (9) (2012) 1460–1466, <http://dx.doi.org/10.1016/j.icheatmasstransfer.2012.08.005>.
- [273] W. Lee, G. Son, Numerical simulation of bubble growth and heat transfer during flow boiling in a surface-modified microchannel, *Heat Transf. Eng.* 35 (5) (2014) 501–507, <http://dx.doi.org/10.1080/01457632.2013.833050>.
- [274] M. Law, P.S. Lee, K. Balasubramanian, Experimental investigation of flow boiling heat transfer in novel oblique-finned microchannels, *Int. J. Heat Mass Transfer* 76 (2014) 419–431, <http://dx.doi.org/10.1016/j.ijheatmasstransfer.2014.04.045>.
- [275] D. Lorenzini, Y. Joshi, Flow boiling heat transfer in silicon microgaps with multiple hotspots and variable pin fin clustering, *Phys. Fluids* 31 (10) (2019) <http://dx.doi.org/10.1063/1.5122209>.
- [276] B. Li, J. Hou, W. Ling, K. Xu, Q. Gao, M. Zeng, Numerical investigation on flow boiling heat transfer in elliptic microchannel heat exchanger with micro fins, *Chem. Eng. Trans.* 94 (2022) 199–204, <http://dx.doi.org/10.3303/CET2294033>.
- [277] I. El Mellas, F. Mucicchi, M. Icardi, M. Magnini, Dynamics of long bubbles propagating through cylindrical micro-pin fin arrays, *Int. J. Multiph. Flow* 163 (2023) <http://dx.doi.org/10.1016/j.ijmultiphaseflow.2023.104443>.
- [278] S. Zhou, X. Xu, B.G. Sammakia, Modeling of boiling flow in microchannels for nucleation characteristics and performance optimization, *Int. J. Heat Mass Transfer* 64 (2013) 706–718, <http://dx.doi.org/10.1016/j.ijheatmasstransfer.2013.05.031>.
- [279] Y. Guo, C.Y. Zhu, L. Gong, Z.B. Zhang, Numerical simulation of flow boiling heat transfer in microchannel with surface roughness, *Int. J. Heat Mass Transfer* 204 (2023) <http://dx.doi.org/10.1016/j.ijheatmasstransfer.2022.123830>.
- [280] H. Lu, X. Duan, M. Xu, L. Gong, B. Ding, A new method of roughness construction and analysis of construct parameters, *CMES - Comput. Model. Eng. Sci.* 123 (3) (2020) 1193–1204, <http://dx.doi.org/10.32604/cmescs.2020.08989>.
- [281] J. Kim, J.Y. Cho, J.S. Lee, Flow boiling enhancement by bubble mobility on heterogeneous wetting surface in microchannel, *Int. J. Heat Mass Transfer* 153 (2020) <http://dx.doi.org/10.1016/j.ijheatmasstransfer.2020.119631>.
- [282] Y.J. Wi, J.H. Kim, J.S. Lee, J.S. Lee, Optimal patterned wettability for microchannel flow boiling using the lattice Boltzmann method, *Coatings* 8 (8) (2018) <http://dx.doi.org/10.3390/coatings8080288>.
- [283] J. Kim, J.S. Lee, Numerical study on the effects of inertia and wettability on subcooled flow boiling in microchannels, *Appl. Therm. Eng.* 152 (2019) 175–183, <http://dx.doi.org/10.1016/j.applthermaleng.2019.02.064>.
- [284] K. Vontas, M. Andreadaki, A. Georgoulas, N. Miché, M. Marengo, The effect of surface wettability on flow boiling characteristics within microchannels, *Int. J. Heat Mass Transfer* 172 (2021) <http://dx.doi.org/10.1016/j.ijheatmasstransfer.2021.121133>.
- [285] K. Tan, Y. Hu, Y. He, Effect of wettability on flow boiling heat transfer in a microtube, *Case Stud. Therm. Eng.* 26 (2021) <http://dx.doi.org/10.1016/j.csite.2021.101018>.
- [286] Y. Song, X. Mu, J. Wang, S. Shen, G. Ling, Channel flow boiling on hybrid wettability surface with lattice Boltzmann method, *Appl. Therm. Eng.* 233 (2023) 121191.
- [287] A. Mukherjee, S.G. Kandlikar, The effect of inlet constriction on bubble growth during flow boiling in microchannels, *Int. J. Heat Mass Transfer* 52 (21–22) (2009) 5204–5212, <http://dx.doi.org/10.1016/j.ijheatmasstransfer.2009.04.025>.
- [288] T.M. Liou, C.T. Lin, Study on microchannel flows with a sudden contraction-expansion at a wide range of Knudsen number using lattice Boltzmann method, *Microfluid. Nanofluid.* 16 (1–2) (2014) 315–327, <http://dx.doi.org/10.1007/s10404-013-1200-2>.
- [289] U.K. Alugoju, S.K. Dubey, A. Javed, Numerical simulation of flow boiling in micro channel to study bubble dynamics, in: *Proceedings of the ASME 2019 Heat Transfer Summer Conference*, 2019.
- [290] Y. Lin, Y. Luo, W. Li, E. Sokolova, Y. Cao, W.J. Minkowycz, A numerical study of slug bubble growth during flow boiling in a diverging microchannel, *Numer. Heat Transfer A* 80 (7) (2021) 356–367, <http://dx.doi.org/10.1080/10407782.2021.1947093>.
- [291] G.D. Xia, Y.X. Tang, L.X. Zong, D.D. Ma, Y.T. Jia, R.Z. Rong, Experimental investigation of flow boiling characteristics in microchannels with the sinusoidal wavy sidewall, *Int. Commun. Heat Mass Transfer* 101 (2019) 89–102, <http://dx.doi.org/10.1016/j.icheatmasstransfer.2019.01.006>.
- [292] V.J. Bhuvu, J.P. Jani, A. Patel, N. Tiwari, Effect of bubble coalescence on two-phase flow boiling heat transfer in raccoon microchannel - a numerical study, *Int. J. Heat Mass Transfer* 182 (2022) <http://dx.doi.org/10.1016/j.ijheatmasstransfer.2021.121943>.
- [293] O.A. Odumosu, H. Xu, T. Wang, Z. Che, Growth of elongated vapor bubbles during flow boiling heat transfer in wavy microchannels, *Appl. Therm. Eng.* 223 (2023) <http://dx.doi.org/10.1016/j.applthermaleng.2023.119987>.
- [294] J. Qiu, J. Zhou, Q. Zhao, H. Qin, X. Chen, Numerical investigation of flow boiling characteristics in cobweb-shaped microchannel heat sink, *Case Stud. Therm. Eng.* 28 (2021) <http://dx.doi.org/10.1016/j.csite.2021.101677>.
- [295] H. Tan, L. Wu, M. Wang, Z. Yang, P. Du, Heat transfer improvement in microchannel heat sink by topology design and optimization for high heat flux chip cooling, *Int. J. Heat Mass Transfer* 129 (2019) 681–689, <http://dx.doi.org/10.1016/j.ijheatmasstransfer.2018.09.092>.
- [296] A.E. Bergles, S.G. Kandlikar, On the nature of critical heat flux in microchannels, *J. Heat Transfer* 127 (1) (2005) 101–107, <http://dx.doi.org/10.1115/1.1839587>.
- [297] G.M. Harpole, J.E. Eninger, Micro-channel heat exchanger optimization, in: *Proceedings - IEEE Semiconductor Thermal and Temperature Measurement Symposium*, Publ by IEEE, 1991, pp. 59–63, <http://dx.doi.org/10.1109/stherm.1991.152913>.
- [298] K.P. Drummond, D. Back, M.D. Sanin, D.B. Janes, D. Peroulis, J.A. Weibel, S.V. Garimella, A hierarchical manifold microchannel heat sink array for high-heat-flux two-phase cooling of electronics, *Int. J. Heat Mass Transfer* 117 (2018) 319–330, <http://dx.doi.org/10.1016/j.ijheatmasstransfer.2017.10.015>.
- [299] S. Wang, H.H. Chen, C.L. Chen, Enhanced flow boiling in silicon nanowire-coated manifold microchannels, *Appl. Therm. Eng.* 148 (2019) 1043–1057, <http://dx.doi.org/10.1016/j.applthermaleng.2018.11.125>.
- [300] Y. Luo, W. Li, Simulation of subcooled flow boiling in manifold microchannel heat sink, *Numer. Heat Transfer A* 77 (11) (2020) 951–965, <http://dx.doi.org/10.1080/10407782.2020.1746578>.
- [301] Y. Luo, J. Zhang, W. Li, A comparative numerical study on two-phase boiling fluid flow and heat transfer in the microchannel heat sink with different manifold arrangements, *Int. J. Heat Mass Transfer* 156 (2020) <http://dx.doi.org/10.1016/j.ijheatmasstransfer.2020.119864>.
- [302] D. Deng, L. Chen, W. Wan, T. Fu, X. Huang, Flow boiling performance in pin fin-interconnected reentrant microchannels heat sink in different operational conditions, *Appl. Therm. Eng.* 150 (2019) 1260–1272, <http://dx.doi.org/10.1016/j.applthermaleng.2019.01.092>.
- [303] J. Xu, X. Yu, W. Jin, Porous-wall microchannels generate high frequency “eye-blinking” interface oscillation, yielding ultra-stable wall temperatures, *Int. J. Heat Mass Transfer* 101 (2016) 341–353, <http://dx.doi.org/10.1016/j.ijheatmasstransfer.2016.05.039>.
- [304] X. Yu, J. Xu, G. Liu, X. Ji, Phase separation evaporator using pin-fin-porous wall microchannels: Comprehensive upgrading of thermal-hydraulic operating performance, *Int. J. Heat Mass Transfer* 164 (2021) <http://dx.doi.org/10.1016/j.ijheatmasstransfer.2020.120460>.
- [305] Y. Kametani, Y. Fukuda, T. Osawa, Y. Hasegawa, A new framework for design and validation of complex heat transfer surfaces based on adjoint optimization and rapid prototyping technologies, *J. Therm. Sci. Technol.* 15 (2) (2020) 1–15, <http://dx.doi.org/10.1299/jtst.2020jtst0016>.
- [306] S. Ozguc, L. Pan, J.A. Weibel, Topology optimization of microchannel heat sinks using a homogenization approach, *Int. J. Heat Mass Transfer* 169 (2021) <http://dx.doi.org/10.1016/j.ijheatmasstransfer.2020.120896>.
- [307] H. Moon, K. Boyina, N. Miljkovic, W.P. King, Heat transfer enhancement of single-phase internal flows using shape optimization and additively manufactured flow structures, *Int. J. Heat Mass Transfer* 177 (2021) <http://dx.doi.org/10.1016/j.ijheatmasstransfer.2021.121510>.
- [308] J.A. Weibel, S. Ozguc, L. Pan, An approach for topology optimization of heat sinks for two-phase flow boiling, 2023, Available at SSRN 4564012. URL: <https://ssrn.com/abstract=4564012>.